Molecular Dynamics Study of Polymorphism in Calcium Carbonate Systems

Emma Sarah Armstrong

A thesis submitted in partial fulfilment of the requirements for the degree of Doctor of Philosophy

The University of Sheffield
Faculty of Engineering
Department of Materials Science and Engineering

February, 2024

Acknowledgements

First and foremost, my thanks goes to my supervisors Dr Colin Freeman and Professor John Harding, for all there teaching and guidance during the PhD. I would also like to thank them both for going above and beyond the support expected from a supervisor.

I would like to thank Dr Stephen Yeandel and Dr Veselina Marinova for all their support and knowledge throughout the process. Thank you greatly to Vittoria Fantauzzo, I couldn't ask for anyone better to share the PhD experience with. I am very grateful for the three of you, and everyone else in the MESAS group, for making the experience all the more enjoyable and for being there when it wasn't.

My greatest thanks goes to Joel. Thank you for all the support, all the discussions on statistics and programming, and most importantly, all the coffee. I couldn't have done this without you.

Abstract

Calcium carbonate is a material of great significance to construction, pharmaceutical and agricultural industries as well as a vital component for marine life. Of the crystalline forms of calcium carbonate, calcite and aragonite are the most stable. Despite only a small difference in thermodynamic stability, calcite is disproportionally precipitated over aragonite. In biomineralisation however, calcite and aragonite are selectively deposited by organisms to fulfil different purposes. This suggests that control over the selected polymorph during nucleation of calcium carbonate is possible.

The presence of magnesium ions, commonly found in seawater, is known to promote precipitation of aragonite by inhibiting the nucleation of calcite. High temperature favours aragonite and more recently, high carbonate content has been shown to nucleate aragonite over calcite at ambient conditions. The mechanisms behind either are not well understood. To investigate the early stages of nucleation when polymorph selection occurs, molecular dynamics simulations have been utilised.

In this work, both kinetic and thermodynamic factors affecting polymorph selection in calcium carbonate have been studied. Configurations of amorphous calcium carbonate with differing ion ratios or water content have been created. We have implemented a cluster analysis technique based on the Manhattan distance metric to identify calcite- or aragonite-like ion clusters within our trajectories. Few polymorph-like clusters were found in all systems but calcite was always the dominant phase.

Values for the interfacial free energy of calcite and aragonite with water have been calculated using a recently developed method. Previous calculations of these values generally contain only the enthalpic contribution, neglecting entropy. The calculation technique utilising an Einstein crystal reference state allows the calculation of both contributions. We found that the entropy contribution varies substantially across the surfaces. It is therefore imperative for entropy to be included in future calculations of interfacial free energies.

Contents

List of Figures

List of Tables

Declaration

I, the author, confirm that the Thesis is my own work. I am aware of the University's Guidance on the Use of Unfair Means (www.sheffield.ac.uk/ssid/unfair-means). This work has not been previously been presented for an award at this, or any other, university.

Chapter 1

Introduction

The understanding of crystallisation and nucleation is of vital importance to a wide variety of industries. Knowledge of selectively precipitating the required form or inhibiting nucleation of unwanted phases is required. Classical nucleation theory (CNT) has long been accepted as the framework to study nucleating systems and successfully describes numerous experimental observations. Many systems have since been found not to follow the proposed theory. The existence of intermediate phases before the crystal nuclei appears is not accounted for in CNT, despite having been observed across various experiments [1]. New or adapted frameworks have been proposed to replace CNT but there is currently no agreed alternative.

Due to the polymorphism exhibited by calcium carbonate, it is a system of particular interest for the study of nucleation. $CaCO_3$ has three anhydrous crystalline forms; calcite, aragonite and vaterite; as well as the amorphous form. Amorphous calcium carbonate (ACC) is often seen as a precursor to the more stable crystalline phases during nucleation. The mechanism by which ACC transforms into the stable phases is still highly debatable within the field. There is evidence supporting both aggregration of amorphous clusters as well as the dissolution of ACC and reprecipitation as a crystal nuclei [2].

ACC is the least stable form of calcium carbonate, followed by vaterite, aragonite and calcite is the most stable. Despite only a small difference in thermodynamic stability, calcite is precipitated disproportionally more than aragonite under ambient conditions. There are well established methods to favour aragonite nucleation over calcite, such as the inclusion of Mg^{2+} ions or increasing the temperature beyond 70°C. Magnesium ions are more readily incorporated into the calcite structure than the aragonite structure and so favour aragonite by inhibiting calcite nucleation [3]. The influence of temperature on polymorph selection in $CaCO_3$ however is still not well understood.

The early stages of nucleation, during which polymorph selection takes place, is difficult to observe experimentally due to both the time and length scales involved in the process. Molecular simulations can be used to observe the dynamics of a nucleating system on the scale of individual atoms. Global properties of the system or general trends across various systems can then be compared with experimental findings to provide a more complete understanding of the process.

Both calcite and aragonite have well defined geometries at the atomistic level. We can take advantage of this to identify clusters of atoms within computer

simulations that resemble these reference structures. In this work, a technique based on the Manhattan distance metric has been implemented to compare the structures of ions within simulated systems to reference structures of calcite and aragonite. The similarity of the clusters to the references geometries are quantified in terms of atom distances and angles.

The aim of this project is thus to investigate the kinetic and thermodynamic parameters that may influence the polymorph selection of calcite and aragonite in calcium carbonate systems. Molecular dynamics (MD) simulations have been used to observe the systems at an atomistic level using well established and tested forcefields for calcium carbonate and water. Since ACC is often seen as a precursor to calcite and aragonite, MD simulations have been run on various set-ups of ACC simulation cells.

Recent experimental findings indicate that high ratios of carbonate to calcium yields substantially more aragonite crystals than calcite at ambient temperatures. Therefore MD simulations of ACC with various ratios of calcium to carbonate ions have been investigated to try and replicate the experimental observations as well as explain why increased carbonate content would favour aragonite nucleation over calcite.

Water is also known to be an important parameter in the nucleation of calcium carbonate crystals from its amorphous state. However, the exact role it plays has yet to be established. Observing water and ACC at the atomistic levels can elucidate how the water molecules behaviour influences the nucleation process. Configurations at various stages of hydration have been run and the movement of the water monitored. For all the ACC systems, the Manhattan distance analysis method has been implemented to identify any ion clusters showing resemblance to calcite or aragonite that could proceed to nucleate into the respective crystal. The number of polymorph-like clusters, distribution of polymorph similarities and lifetime of the found clusters have been investigated.

The described ACC configurations focused more so on the kinetic factors affecting polymorph selection in $CaCO_3$, however there is also the thermodynamic factors to be considered. The change in free energy between systems must be calculated to be physically meaningful. To do so, a reference state of known free energy is used and the system transformed to this state via a thermodynamic pathway. For interfacial free energies between a solid and liquid, finding a suitable pathway is particularly difficult, further complicating the matter. Nevertheless, a novel method to calculate interfacial free energies using Einstein crystals as the reference state has recently been developed [4]. We have applied this method to the calcium carbonate system to look at the free energies of the solid phases in water.

The interfacial free energies of various calcite and aragonite surfaces in water have been calculated to determine their relative stabilities. From these values, morphologies of calcite and aragonite crystals can be predicted and compared to known structures. Most previous calculations of calcium carbonate and water free energies have only considered the enthalpic contribution. However with the Einstein crystal free energy method, both the enthalpic and entropic contributions are included. The relative contributions of enthalpy and entropy to the free energy along with their variation with increased temperature have also been calculated.

Overall we present both kinetic and thermodynamic approaches to explore polymorph selection in calcium carbonate using results from molecular dynamics simulations.

Chapter 2

Crystallisation

Crystallisation is an important process by which atoms in a disordered state transition to a highly ordered structure. In nature, crystallisation is responsible for rock formation [5] and biomineralisation; creating shells, exoskeletons and bones [6]. Ice crystals in the atmosphere dictate the amount of solar radiation passing through to the Earth [7] and the process of calcium carbonate crystallisation in the oceans helps capture carbon dioxide and maintain the pH of seawater [8,9,10]. Industrially, nearly all chemical production will rely on crystallisation at one stage. Generally, it can be used to separate or purify systems as well as the production or recovery of products [11] In particular, the synthesis of drugs and the production of food additives rely heavily on crystallisaton [11]. In some industries, such as the oil industry, crystallisation is an unwanted process which hinders production, therefore understanding how crystallisation works is essential to be able to inhibit the process [12].

The crystallisation process is a first order phase transition. Two stages are required for crystallisation to occur. The first is nucleation, where a crystalline phase first appears in the disordered system, followed by crystal growth, in which the particles increase in size until the crystalline phase is formed.

A crystal contains highly ordered atoms or molecules, a unit of which is repeated in all directions to form a lattice. Single crystals can also be identified by their distinct geometry and crystal faces orientated in particular directions [13]. The same material can have different crystal forms with different properties. Polymorph selection is therefore incredibly important to ensure the desired crystal is produced for its intended use; be it pharmaceutical or agricultural [14].

It is thought that the final crystalline form of a material is determined by the initial stages of crystallisation, during nucleation [15]. Understanding the mechanism behind nucleation is essential to the selection of the crystalline phase in production.

2.1 Nucleation

Nucleation occurs when a new condensed phase forms within the system. If crystalline particles of the material are present in the system and induce the nucleation of further particles, the process is known as secondary nucleation. If the nucleation is not induced and is instead spontaneous, it is primary nucle-

ation. Primary nucleation can be split into two further types; homogeneous and heterogeneous nucleation. Homogeneous occurs in the absence of impurities or surfaces unlike heterogeneous nucleation, which occurs with the nucleus at a surface and is the more common process [13].

Generally the thermodynamic driving force for the first order phase transition is the supersaturation. A supersaturated solution occurs when the concentration of solute is greater than the concentration at equilibrium - it is a metastable state [16].

The mechanism by which nucleation occurs has been a topic of interest for decades and many theories have been presented to explain the process. The most successful has been classical nucleation theory (CNT). However, more recent studies have challenged this framework and suggest that a more complex mechanism than that described by CNT is required to fully understand nucleation [1].

2.1.1 Classical Nucleation Theory

Classical nucleation theory states that nucleation is not a spontaneous process and a free energy barrier ΔG^* must be overcome for the new phase to appear. The energy penalty arises due to the phase boundary and surface tension associated with the the formation of the solid phase [17].

In a homogeneous system, the nucleation of a spherical nuclei of radius r results in a change in the free energy of

$$\Delta G = \frac{-4\pi r^3}{3\nu} kT \ln S + 4\pi r^2 \sigma \tag{2.1}$$

where ν is the volume of a single molecule in the system and S the supersaturation ratio. Supersaturation ratio is given by

$$S = \frac{C}{C^*} \tag{2.2}$$

the ratio of solute concentration C and the solute concentration at equilibrium C^*. The first term in Equation 2.1 is the contribution from the bulk to the free energy, or the volume energy. The second term is the contribution from the interface where σ is the specific surface energy between the two phases. At larger values of r, the volume term dominates and ΔG will decrease, however at smaller r, ΔG increases due to the more significant interfacial term, as demonstrated in Figure 2.1.

From Equation 2.1, we can determine the maximum value of ΔG and thus the free energy barrier ΔG^*. The radius at which ΔG^* occurs is known as the critical nuclei radius, r^*, and gives the minimum size nuclei for which nucleation can take place. By differentiating the equation with respect to r, the critical radius is $r^* = 2\sigma\nu/kT \ln S$ and the barrier is determined by

$$\Delta G^* = \frac{16\pi\sigma^3\nu^2}{3(kT)^2(\ln S)^2} \tag{2.3}$$

which must be overcome by thermal fluctuations in the system [18].

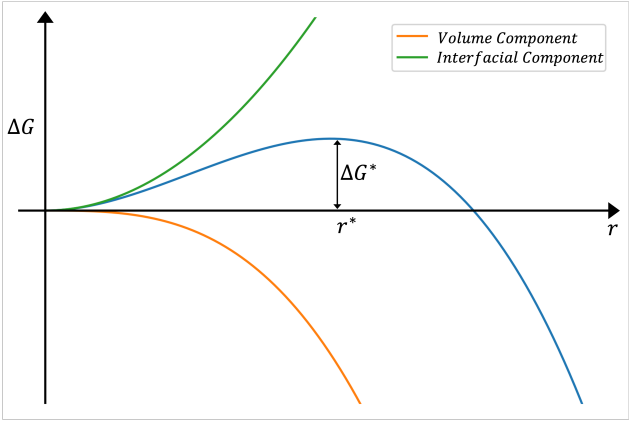

Figure 2.1: *Schematic diagram of the change in free energy of a system associated with nucleation. The total free energy (blue) comprises a bulk, volume term and an interfacial term associated with the surface between the two phases. At larger values of r, the radius of the nucleus, the volume component dominates whereas at smaller r, the interfacial term dominates. A maximum is present corresponding to the energy barrier for nucleation, ΔG^*, which happens at the critical radius r^*.*

Arguably the greatest success of CNT is the calculation of the rate of nucleation J which is given by the following,

$$J = A \exp\left(-\frac{E_A}{kT}\right) \exp\left(-\frac{\Delta G^*}{kT}\right) \tag{2.4}$$

in which E_A is the activation energy for atomistic processes and A is a material-dependent constant [19] but it can be very inaccurate if experimental values of σ are used. The first exponent is related to the kinetic barrier; it accounts for the number of possible nucleation sites, the attachment rate and the fact that clusters may shrink in size before growing into a crystalline phase [13]. Contributions to the kinetic term are difficult to establish and are often neglected leaving only the thermodynamic exponent.

CNT is based on vapour to liquid condensation of water droplets but it can also be used to approximate liquid to solid systems and crystallisation out of solution [20]. Many systems exhibit behaviours that can be successfully described using CNT, however the theory relies on a number of approximations that fail to account for more complex behaviour. The calculated nucleation rates are thus off by orders of magnitude [21]. The most dubious assumption of the theory is the capillary approximation, which assumes that the resulting nuclei have the same macroscopic properties as the bulk phase. This assumes that the interfacial energy of the nuclei is the same as the bulk interfacial free energy, which may hold for larger cluster sizes but will break down at clusters comprising a few molecules [16]. The key assumption of CNT is that the nucleus grows by single units. For some systems, the addition and fragmentation of clusters comprised of multiple atoms is a significant kinetic pathway which cannot be approximated by single atom adsorption or emission [20]. Additionally, we assume these are rare events so that transition state theory can be used.

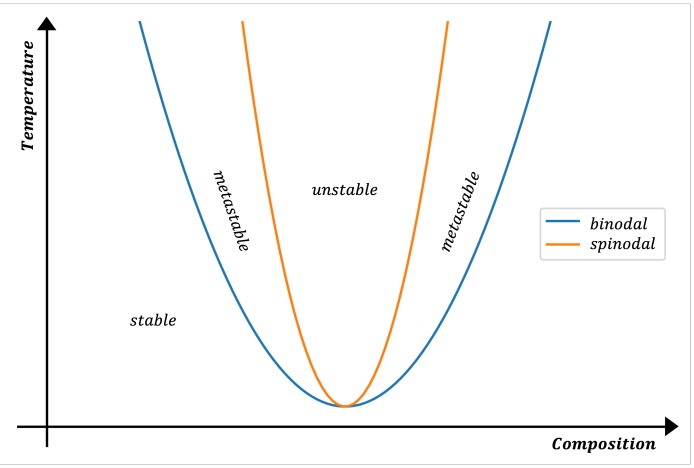

Figure 2.2: *Illustrative plot of the phase diagram for a two-phase system. Outside the binodal curve (blue), the system is stable. Crossing the curve into the metastable region represents a phase transition. A nuclei forming in the system corresponds to movement through the metastable region reaching the boundary of the spinodal (orange) region.*

2.1.2 Phase Separation

A phase transition can also occur via phase separation. For a generic two phase system, a phase diagram for temperature and composition is shown in Figure 2.2. Two curves are displayed; the binodal and spinodal. The binodal curve corresponds to the conditions at which the coexistence of both phases occurs. Outside the binodal curve lies the stable region where the solution is undersaturated. Crossing the binodal curve into the metastable region can be achieved by altering the composition at a constant temperature or vice versa. At this point phase separation can occur. Nucleation as described by CNT occurs as the supersaturation increases in the metastable region until the solution reaches the boundary between the metastable and unstable regions defined by the spinodal curve. At this boundary, phase separation must occur and decomposition happens spontaneously. However, this can only take place if the spinodal is reached without a nucleus forming beforehand [22].

2.1.3 Non-Classical Nucleation

Despite the success of CNT and its ongoing use, an increasing number of systems cannot be explained by the current framework. The formation of an intermediate phase is often seen before the final nuclei appears. An extension of the classical theory includes an energy barrier to overcome to form a precursor of increased density, which may be stable or unstable with reference to the liquid phase. However this precursor does not exhibit a crystalline structure and so a second energy barrier needs to be overcome to order the atoms and form the nuclei, resulting in a two-step nucleation [23]. There is significant experimental evidence for a two-step nucleation mechanism [15] similar to the scheme illustrated in Figure 2.3, but the exact details of the mechanism and extension of

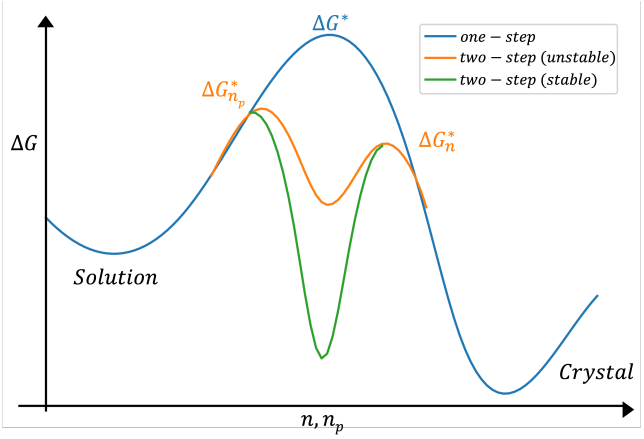

Figure 2.3: *Comparison of the classical one-step nucleation and the proposed two-step nucleation. The free energy is presented as a function of cluster size, n. For the classical case, a single free energy barrier needs to be overcome for the crystal to form from solution. With a two-step mechanism, a second barrier is introduced associated with a precursor cluster of size n_p appearing. The intermediate precursor can be unstable (orange) or stable (green) with respect to the solution.*

CNT are still up for debate.

Various types of intermediates have been observed experimentally including, pre-nucleation clusters [22,24], amorphous phases [25,26] and liquid-like precursors [27,28], amongst many others. Pre-nucleation clusters have been defined as thermodynamically stable clusters of ions or atoms that participate in the nucleation process. A significant amount of work has been done to understand their nature and the role they play in nucleation as well as attempts at nucleation theories to account for their existence [22]. Amorphous phases appearing before the crystalline phase have been observed in multiple systems [26], but a substantial amount of research has looked at calcium carbonate. Amorphous calcium carbonate is often seen before the system nucleates into one of the more stable crystalline phases [29,30,31]. In biomineralisation, the amorphous phase is nearly always seen as a intermediate stage before crystallisation.

Although substantial evidence for the existence of intermediate phases and more complicated pathways than that suggested by CNT are available, there is no agreed upon mechanism to describe the observed nucleation [32]. There is evidence that supports the formation of intermediate phases and then aggregation to the final phase [30,33]. Other experiments suggest the intermediate phases dissolve before being reprecipiated as the crystal nuclei [34]. In systems with multiple polymorphs, such as $CaCO_3$, these have nucleated under the same conditions implying multiple pathways occurring at the same time. [35,36,37] Examples of these pathways for a generic system are illustrated in Figure 2.4.

Currently there is no agreed upon theory to explain the multiple different pathways observed and thus no replacement for CNT. Despite advances in imaging technology, the time and length scales of nucleation are still difficult to observe. However the implementation of atomistic simulations allows di-

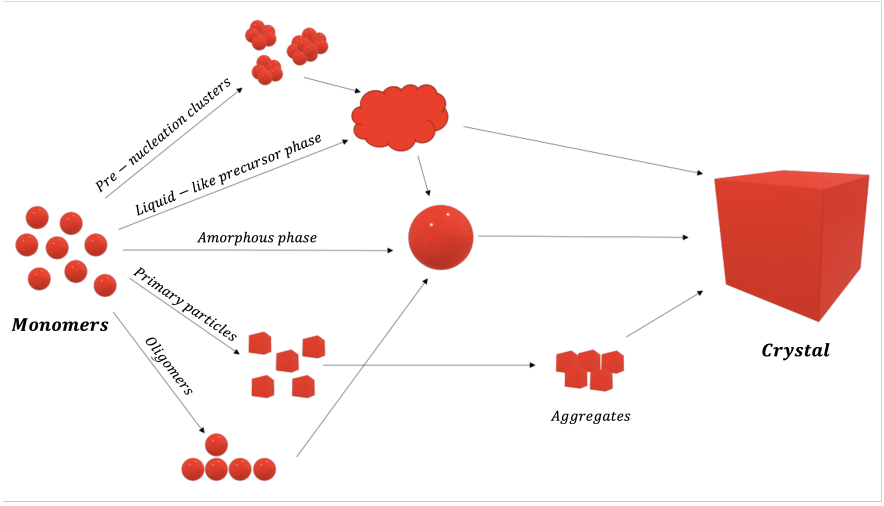

Figure 2.4: *Illustration to demonstrate possible intermediate phases and associated nucleation pathways. Pre-nucleation clusters, liquid-like precursors, amorphous phases, primary particles and oligomers are considered. The intermediates can then transform immediately into the crystal phase or proceed through a further step before the final phase is reached.*

rect access to the dynamics of the system, providing significant insight into the mechanisms during nucleation not available experimentally [23,31].

2.2 Commonly Studied Systems

Three of the most common nucleation systems investigated include: ice, sodium chloride and calcium carbonate. Ice nucleation from water is an example of a crystal made from molecules, whereas NaCl is a crystal where the solute is highly soluble. Conversely, the $CaCO_3$ solute is highly insoluble. The varying properties of these systems showcase the range of research available on crystallisation.

2.2.1 Ice

Given the abundance and importance of water, it is unsurprising that the nucleation of water droplets into ice has been extensively studied. The formation of ice crystals in the atmosphere in particular is vital to cloud and climate sciences [7]. Even with the vast amount of research conducted on ice, there are still numerous questions around the process requiring further investigation.

Of particular interest is the microscopic study of ice nucleation from water, which can be studied using atomic simulations. Numerous forcefields for use in molecular dynamics have been developed to encapsulate the behaviour of water. However specific models are required to simulate the nucleation of ice to ensure properties such as density and the coexistence curve are correct [38]. The location of phase boundaries are particularly sensitive to changes in the

potential model parameters, therefore the melting temperature of the specific water model is important to note.

Given the timescale of crystallisation, molecular dynamics simulations alone are not enough to capture the behaviour of the process. Metadynamics is usually employed, allowing longer simulations and improved sampling for rare events. Calculations have been performed to look at the homogeneous nucleation of ice and determining the preferred polymorph formed under the simulation conditions [39]. More recent studies have extended to include the temperature dependence of nucleation rates whilst also concluding the local tetrahedral coordination of molecule clusters from which water nucleation appears [40].

2.2.2 NaCl

Sodium chloride is a simple system making it ideal for performing atomic simulations. The forcefields available accurately predict material properties and the experiments looking at NaCl nucleation generally work at small volumes; resembling more closely the simulation systems. The size and simplicity of the ions allows larger and longer computations.

The kinetics of NaCl nucleation and crystallisation has been investigated using seeded simulations; a NaCl crystal is already present in the system [41]. These simulations were performed at comparable supersaturations to experiment yet the resulting nucleation rates were still orders of magnitude out from experimentally calculated values.

Other studies using forward flux sampling, a similar sampling approach to metadynamics, to calculate nucleation rates of NaCl results in significantly lower nucleation rates [42]. However these calculations do not depend on CNT. Molecular dynamics simulations have also been employed to look at the pathways taken [43]. A wide distribution of pathways were found with two-step nucleation pathways being more dominant than the classical one-step, in line with experimental observations.

2.2.3 $CaCO_3$

Crystallisation of calcium carbonate is one of the most studied systems due to its scientific importance. Despite its extensive study both experimentally and computationally, it is still not well understood [44]. The size, morphology and polymorph of resulting crystals can be easily determined by the synthesis conditions . However there is still considerable research required for understanding the mechanism behind $CaCO_3$ crystallisation, leading to greater control over its precipitation. As calcium carbonate is the focus of this work, it is discussed more thoroughly in Chapter 3.

Chapter 3

Calcium Carbonate

$CaCO_3$ is one of the most ubiquitous minerals and has practical uses across numerous fields. It is therefore the focus of substantial amounts of research. The mineral is commonly found in limestone, eggshells, pearls and extensively in organism shells and exoskeletons[6,45]. Calcium carbonate has important roles in the construction[46,47,48], pharmaceutical[49,50] and agricultural industries[51,52]. The properties and applications of $CaCO_3$ depend on the particle size, morphology and selected polymorph. These can be tuned during the synthesis process by varying setup and environmental parameters to produce the desired properties.

3.1 Polymorphs

Polymorphism displayed in calcium carbonate is one of the reasons the system is still of great interest. The amorphous phase is often seen as a precursor to the crystalline phases, as is discussed in more detail in Section 3.2. It is also possible to crystallise all three anhydrous crystal phases of $CaCO_3$ simultaneously under ambient conditions[53]. The control over polymorph deposition exhibited by living organisms is still not well understood and drives further study for polymorph control[54,55].

3.1.1 Phases

Calcium carbonate has six polymorphs: amorphous calcium carbonate, two hydrated phases and three anhydrous phases. This work will only focus on the anhydrous phases and so the two hydrated phases will not be discussed further. In order of stability, the anhydrous crystalline phases are calcite, aragonite and vaterite, however the difference between thermodynamic stability of calcite and aragonite is small[56].

Calcite exhibits a trigonal crystal structure, aragonite an orthorhomic and vaterite a hexagonal structure. The detailed structure of vaterite is not well understood[57], however the structures of both calcite and aragonite are well-defined at the atomic level. Calcite exhibits an antiprism structure and an oxygen coordination of 6 around the Ca, whereas aragonite has a prism structure and a coordination of 9 around the Ca, as detailed in Figure 3.1.

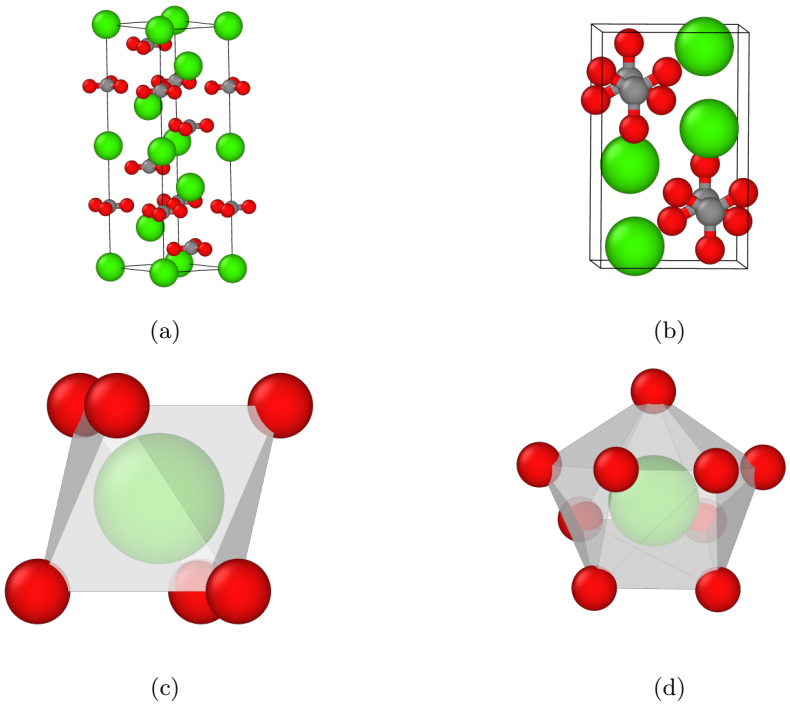

Figure 3.1: *Unit cells of calcite* (a) *and aragonite* (b) *to demonstrate the crystal structure. The different oxygen coordinations are shown in* (c) *and* (d) *for calcite and aragontite respectively. The central calcium ion (green) is surrounded by 6 oxygen atoms (red) for calcite, resulting in an antiprism structure. For aragonite the 9 oxygen atoms results in a prism structure surrounding the ion.*

The crystal morphology of calcite is dominated by the $\{10\bar{1}4\}$ surface, resulting in a rhombohedral structure often found in experiment. For aragonite and vaterite, the morphologies are more complicated and thus a variety of structures are grown in experiment including needle-like structures, fibrous, and spherical shapes[58,59?,60]. Calcite is of importance in soil remediation and stablisation. It is a component of limestone along with aragonite and is utilised in concrete production[61]. Aragonite is essential for most sea life and maintaining the natural pH of seawater[9]. In biomedicine, vaterite is in high demand with possible roles in drug delivery and bone implants amongst others[62]. Control over $CaCO_3$ polymorphism is thus essential to many industries and methods to produced the desired crystalline structure are required.

Mollusc shells are composed primarily of aragonite, although calcite and vaterite is often used by organisms to repair them[63]. Molluscs, amongst other marine organisms, have exhibited the ability to control polymorph production of $CaCO_3$ with the possibly of switching between the calcite and aragonite phases[54,55]. The capability of selection is thought to arise from the surrounding environment and solution[64]. Observation of this natural phenomena provides insight into the possible control methods available experimentally and commercially.

3.1.2 Polymorph Selection

Calcite readily nucleates at ambient conditions, research is therefore focused on promoting the nucleation of aragonite under similar conditions. Numerous ways have been found to enhance the nucleation of aragonite, however, the underlying mechanism and understanding have not been established in many cases.

Mg^{2+} Ions

As evidenced by aragonite precipitation in seawater, the inclusion of Mg^{2+} ions in solution induces aragonite nucleation. This increase in aragonite nucleation results from the inhibition of calcite nucleation in the presence of Mg^{2+} ions. It is suggested that the smaller ions are more readily accepted into the calcite structure than the larger Ca^{2+} ions, ultimately increasing the interfacial energy. Although the inclusion of Mg^{2+} ions increases the solubility of calcite, the resulting increase in energy is more significant. Due to the higher oxygen coordination of aragonite, magnesium inclusion has a much greater energy penalty than calcium; approximately four times larger[3]. Additionally, ninefold coordination of Mg^{2+} by oxygen in crystals is unknown[65]. Thus the thermodynamic stability of calcite is reduced such that aragonite becomes the more favourable structure[3].

Both experiment and ab initio calculations conclude that high ion ratios, $Mg^{2+}/Ca^{2+} > 2$, are required in solution for calcite inhibition. At this ratio, both aragonite and calcite are precipitated but when going to even higher ratios, $Mg^{2+}/Ca^{2+} > 4$, the precipitation is almost entirely dominated by aragonite[66]. The Mg^{2+}/Ca^{2+} ratio is modern seawater is thought to be approximately 5.2[67]. Considering only the effect magnesium ions have on $CaCO_3$ nucleation, seawater provides a suitable environment for aragonite nucleation, consistent with the high levels of aragonite observed in the oceans.

At lower Mg^{2+}/Ca^{2+} ratios, although aragonite will not be promoted, Mg^{2+} may still be incorporated in the calcite lattice. The presence of magnesium ions alters the final morphology of the calcite crystal; rounding of the rhombohedral structure associated with pure calcite has been observed as the ion ratio was increased. ACC was also found to precipitate first with the amount of Mg^{2+} incorporated depending on the ion ratio in the solution. The magnesium was shown to stabilise the resulting ACC before the final transformation to calcite occurred [66].

Other inorganic ions, such as Sr^{2+} and Li^{+}, are able to control calcium carbonate polymorph selection [68,69] as well as a large variety of organic macromolecules [70]. Of particular interest are polyamines, as they are thought to promote aragonite nucleation at low concentrations, in direct contrast to Mg^{2+} ions which enhance aragonite nucleation by inhibiting that of calcite [53].

Temperature

The precipitation of calcite and aragonite is known to have a temperature dependence. At low temperatures and room temperature, calcite is the most stable polymorph and, in the absence of additives, will be the only polymorph present. As the temperature increases, aragonite is also formed, resulting in the coexistence of calcite and aragonite phases. When temperatures reach approximately $70°C$ and beyond, pure aragonite is produced [71]. It can then be shown that the proportion of calcite and aragonite precipitated is a function of both temperature and the Mg^{2+}/Ca^{2+} ratio [72]. With sufficiently high ion ratios, pure aragonite can be crystallised at room temperature and below.

Although it has been well established that higher temperatures promote aragonite nucleation, the mechanism is not understood. Calcite is always the more stable polymorph even with increased temperature as reflected in the bulk free energies [73].

CO_3^{2-}/Ca^{2+} Ion Ratio

The activity ratio of CO_3^{2-} to Ca^{2+} is also known to influence calcium carbonate nucleation. Due to the structure of calcite, both obtuse and acute step edge form during crystal growth, each with different growth rates. It has been shown that varying CO_3^{2-}/Ca^{2+} leads to further difference in growth rates; at excess calcium, obtuse steps grow more rapidly whereas excess carbonate causes the acute step growth rates to dominate [74]. The nucleation rate as well as the growth rate is also dependent on the activity ratio in the system. Deviating from equal quantities of both types of ion results in slower rates, however the rates are reduced more with excess Ca^{2+} than with excess CO_3^{2-} [75]. In the same study, the size of the $CaCO_3$ particle was also found to differ asymmetrically with the size of CO_3^{2-}/Ca^{2+}. At higher calcium content, larger particle sizes were observed than for higher carbonate content, however neither were larger than the particles formed at equal ratios. It was not stated whether the resulting crystalline form was analysed or varied with the activity ratio.

The influence of varying carbonate concentration has been observed experimentally with the inclusion of Mg^{2+} ions to stabilise resulting ACC. Carbonate concentration was varied such that the final values of CO_3^{2-}/Ca^{2+} activities ranged from roughly 0.05 up to 4 [76]. At low CO_3^{2-}/Ca^{2+} values and low magne-

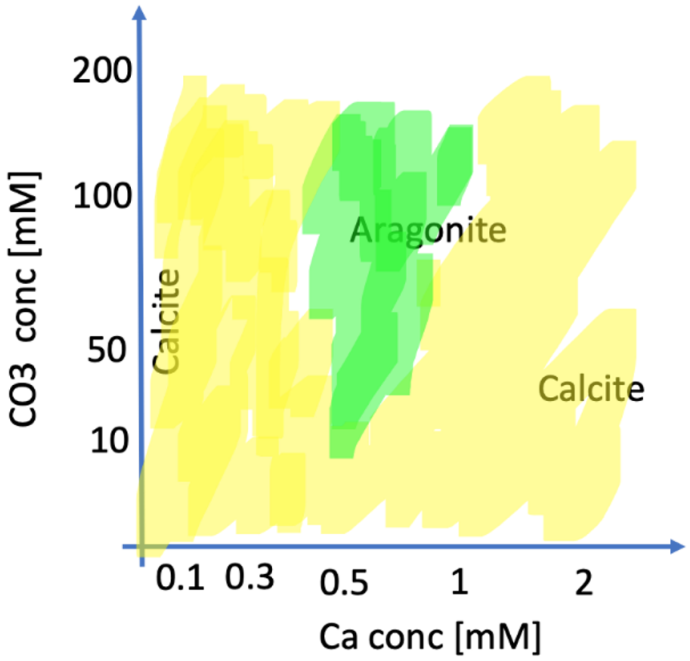

Figure 3.2: *Schematic phase diagram to demonstrate the dominant polymorph produced under varying solution conditions from the work of Kim (currently unpublished). Of particular interest is the region of low* Ca^{2+} *concentration and high* CO_3^{2-} *in which aragonite is precipitated over calcite under ambient conditions.*

sium content, only calcite was produced. As the amount of Mg^{2+} was increased, both calcite and aragonite were precipitated. With excess CO_3^{2-}, monohydrocalcite (one of the hydrated forms of calcium carbonate) was produced in place of calcite which eventually transformed into the more stable aragonite. Although the Mg^{2+}/Ca^{2+} ratio had considerably more impact on polymorph selection, the CO_3^{2-}/Ca^{2+} ratio also influences the selection to a degree which cannot be ignored.

Experiments performed by Kim and Meldrum (currently unpublished) have looked at the effect of varying the respective concentrations of Ca^{2+} and CO_3^{2-} in solution, at ambient conditions and without the inclusion of Mg^{2+} ions. The ratio of CO_3^{2-}/Ca^{2+} concentrations investigated was significantly higher than in previous experiments.

Why high carbonate concentrations at selected calcium concentrations leads to the dominance of aragonite crystals is unknown and highly speculative. The reasoning will likely be kinetic as opposed to thermodynamic and related to the ability for the ions to reorder themselves.

3.2 Amorphous Calcium Carbonate

Amorphous calcium carbonate (ACC) is the least stable form of calcium carbonate. It is observed prominently in biomineralisation with uses ranging from exoskeleton stiffeners to temporary storage of calcium within tissues [77,78]. Both hydrated and dehydrated forms exist naturally.

Following Ostwald's step rule, which states that the least stable polymorph will crystallise first, ACC is often precipitated before the final crystal form appears [79]. The precursor exists for a very small amount of time before transforming into one of the more stable forms. It has been suggested this occurs through a dissolution and reprecipitation mechanism [34]. However there is a significant difference in conditions between the biomineralisation of calcite via ACC and the inorganic, experimentally produced crystals.

Despite dehydrated ACC's extreme instability, many organisms are able to produce stable ACC [80]. These stable forms are found to be hydrated, generally with a 1:1 ratio of calcium carbonate and water [2,81], whereas the transient precursors are anhydrous [2]. A high amount of magnesium or phosphorous ions are often present in stable ACC [2,82]; nearly all biogenic ACC contains Mg^{2+} ions. Due to their smaller size, Mg^{2+} readily replaces Ca^{2+} ions within the structure. Mg^{2+} ions have a greater dehydration enthalpy than Ca^{2+}, making dehydration of ACC more difficult and thus increasing stability [83].

In addition to the dissolution and reprecipitation mechanism suggested, $CaCO_3$ crystals have been observed forming through cluster aggregation. Metastable particles of ACC assemble through the aggregation of ion clusters before further organising and nucleating [84]. Experiments also show the existence of both ACC and crystalline phases, suggesting that a solid-state transformation takes place [82]. The full process by which calcium carbonate crystallises through amorphous phases has not been agreed upon and is still subject to substantial investigation.

It is difficult to observe the dynamics of nucleation experimentally, therefore atomistic simulations provide an important insight into determining the process occurring. Molecular dynamics studies of ACC nucleation have supported theories of cluster aggregation leading to nuclei formation and growth as well as variation in local ACC structure [85]. The local structure analysis provided by computational studies is particularly important in the study of $CaCO_3$ polymorphism and analysing the suggestion of pre-nucleation ACC clusters resembling the final crystalline phase.

Closer inspection of the structure of stable ACC indicates some short-range order around the Ca^{2+} ion despite being an "amorphous" phase, however no long-range order is present [86]. It has therefore been suggested that amorphous calcium carbonate is not a single phase but a family of amorphous phases with varying local structure [2].

The selected deposition of stable or unstable ACC in biomineralisation implies control over the structure, however, the mechanism by which this occurs is still unknown. A vast amount of research has gone into, and continues looking at achieving the same control over ACC nucleation as exhibited in nature. Effective synthesis of stable ACC under ambient conditions would lead to commercial production for use in drug delivery and improving material fabrication [87].

Many additional methods are known to influence calcium carbonate nucleation: high pressure favours aragonite polymorphs [56], solution stirring [76], pH [88] and confinement [89] all affect polymorph formation. The underlying mechanism and understanding of why such factors alter polymorph selection are poorly known. The early stages of nucleation, when polymorph selections is assumed to take place, is difficult to observe experimentally due to the time and length scales involved. Utilising computer simulations allows monitoring of individual atom dynamics and local atom environments, which cannot be obtained in the lab. Calculation of macroscopic system properties permits comparison with experimental results to obtain a broader understanding of the mechanisms occurring during nucleation.

Chapter 4

Methodology

4.1 Molecular Dynamics

Molecular dynamics (MD) uses Newton's classical laws of motion to model the motion of individual atoms. The particles are usually approximated as hard spheres and the interactions between them are encapsulated in forcefields of varying complexity. By initially assigning positions and velocities to atoms, then numerically solving Newton's equations, trajectories of the particles in the system are obtained which detail their behaviour over the course of the simulation. Relatively large ($\sim 10^9$ atoms) systems can be observed at the atomistic level as they evolve with time. With MD simulations, it is possible to reach small time and length scales ($< 10^{-6}$ s), that are difficult or even impossible to achieve experimentally. Bulk properties of systems can be predicted using MD calculations, enabling a direct comparison with experimental results. This comparison allows confirmation of the accuracy of computationally produced results or the possibility to guide experimental setup for further investigations.

The detailed electron structure found in quantum mechanical methods is not required, allowing greater size and duration of calculations as well as a reduced computational expense. The time evolution in MD simulations means it is possible to calculate dynamical properties of the system, such as diffusion, which is not possible in Metropolis Monte Carlo methods.

4.1.1 Forcefields

Simulations of sufficiently long time scales or length scales are far too computationally expensive for ab initio methods. If the electronic properties of the system are not required and no changes are expected in the electronic structure, the potential energy of the system can be described using forcefields. Forcefields encapsulate the physics of the interactions occurring between atoms in a set of parameters and functional forms [90].

The potential energy of a system is made up of bonded potentials and potentials describing non-bonded interactions between atoms. Harmonic and Morse potentials are two common types of two-body potentials describing unbreakable and breakable bonds of pairs of atoms respectively. A harmonic function form can also be used to describe angle bending and improper torsion potentials maintain the geometry of four-body systems.

For pair potentials describing atoms not bound together, we assume that the interaction between them depends only on the interatomic distances [91]. The simplest and most common form of pair-potential used is the Lennard-Jones potential

$$V^{LJ}(r) = 4\epsilon \left[\left(\frac{\sigma}{r}\right)^{12} - \left(\frac{\sigma}{r}\right)^{6} \right] \tag{4.1}$$

with ϵ the characteristic energy (or potential well depth) and σ the ideal separation of the atoms present. The functional form encapsulates both the repulsive Pauli exchange interaction at short range distances and the attractive van der Waals interaction at longer ranges. It is computationally inexpensive yet captures the required physics for a realistic description of interactions between atoms and ions; it is therefore the basis of many more complicated pair potential models.

Beyond certain distances, the interactions between atoms will become negligible and cease to contribute significantly to the energy of the system. To avoid unnecessary computation, cutoff distances, R_c, beyond which the interaction between atoms can be ignored are included in forcefields. Discontinuities in interaction energy could cause strange and unwanted behaviour in the system, therefore smoothing functions such as,

$$E(r) = V^{LJ}(r) - V^{LJ}(R_c) - (r - R_c)\frac{dV^{LJ}}{dr}\bigg|_{r=R_c} \tag{4.2}$$

are usually applied to combat this [92].

To create a forcefield to describe a particular system, the functional form and parameters need to be fit to available data. Parameters can be fitted to available experimental data for the system or alternatively can be fit to data obtained from more accurate quantum calculations. It is important to ensure the data used for fitting is relevant and encapsulates the physics required for the forcefield to be used. For commonly studied systems, many forcefield are available from the literature that have been extensively used, studied and improved. The forcefield required depends greatly on the simulation setup.

4.1.2 MD Algorithms

Molecular dynamics simulations depend entirely on classical mechanics, or Newton's laws of motion. By solving Newton's second law,

$$F = ma \tag{4.3}$$

the acceleration, a, and thus the trajectories, of the individual atoms are computed. The mass, m, of the atoms are known constants and the force, F, is calculated from the utilised forcefield. The force acting on the atoms and the acceleration must be recalculated and updated throughout the simulation. As it cannot be calculated analytically, numerical methods are required to solve Newton's equations. Integration algorithms need to be computationally fast but have a low memory demand; they also need to be accurate and stable so energy is conserved and no drift occurs. Many integration algorithms have been implemented in molecular dynamics simulations. the most common of which is the Verlet family of algorithms.

4.1.2.1 Verlet Algorithm

The original Verlet integration algorithm solves Newton's laws of motions with good numerical stability and eliminates the issues with Euler's method at little extra computational cost [90]. The position of a particle is then given by

$$r(t + \Delta t) = 2r(t) - r(t - \Delta t) + \frac{F(t)}{m}\Delta t^2 \tag{4.4}$$

where r is the position, t time and Δt is the chosen simulation timestep. Although an improvement on the most simple integration method, the Verlet algorithm has problems: the previous position of the particle is always required to calculate the current position, which is unknown at the start of the simulation, and the velocity is not produced in the algorithm and must be calculated separately.

4.1.2.2 Velocity Verlet Algorithm

To calculate position and velocity at the same time, the Velocity Verlet algorithm can be implemented [90]. Position and velocity are propagated forwards in time. The velocity, v, is calculated at the intermediate timestep

$$v\left(+\frac{\Delta t}{2}\right) = v(t) + \frac{F(t)}{m}\frac{\Delta t}{2} \tag{4.5}$$

which can be used to calculate the position at the new timestep

$$r(t + \Delta t) = r(t) + v\left(t + \frac{\Delta t}{2}\right) \tag{4.6}$$

and is not dependent on the particle's previous position. The force must be recalculated for the new timestep and can be used to determine the new velocity

$$v(t + \Delta t) = v\left(t + \frac{\Delta t}{2}\right) + \frac{F(t + \Delta t)}{m}\frac{\Delta t}{2} \tag{4.7}$$

with the previously calculated intermediate timestep velocity. Calculating the force is the largest component of the calculation, which is only performed once at each timestep in the method described. The Velocity Verlet algorithm has been used in the LAMMPS [93] calculations performed in this work.

4.1.2.3 Leapfrog Verlet Algorithm

Although the Velocity Verlet Algorithm is time reversible and numerically stable, it is also a two step calculation leading to higher computational costs and time [94]. Forces are calculated first before the velocity at the intermediate time is calculated

$$v\left(t + \frac{\Delta t}{2}\right) = v\left(t - \frac{\Delta t}{2}\right) + \frac{F(t + \Delta t)}{m}\Delta t \tag{4.8}$$

using the velocity at half a timestep behind. The position is calculated as following

$$r(t + \Delta t) = r(t) + v\left(t + \frac{\Delta t}{2}\right)\Delta t \tag{4.9}$$

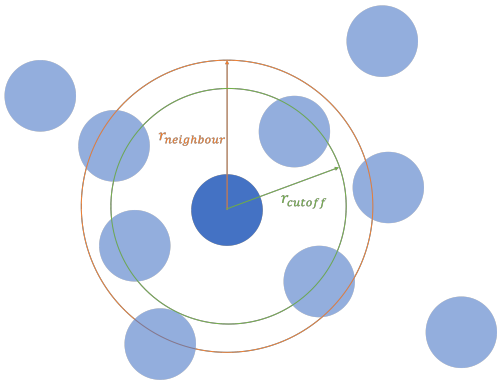

Figure 4.1: *Determining the neighbours to be stored for a given atom. All particles within the volume of the sphere centred at the chosen atom can be considered neighbours. The cutoff for neighbouring atoms, $r_{neighbour}$, should be larger than the cutoff for the potential interaction, r_{cutoff}, to ensure no interactions are missed.*

based on the current postion and the half-step velocity. The Leapfrog Verlet algorithm is simpler and faster than the Velocity Verlet, with only a single step required, but has issues around thermostatting. DLPOLY [95] calculations performed in this work have been implemented with the Leapfrog Verlet algorithm.

4.1.2.4 Timestep

When setting up MD calculations, the timestep chosen is incredibly important. If the timestep is too small, the simulations will make little progress and result in large computational time and expense. Alternatively, if the timestep is too large, key occurrences are likely to be missed, atoms may crash into one another or other unphysical phenomena may occur. To strike a balance between the two, the timestep is usually selected to be smaller than the fastest atom motion present in the system. Generally this is on the order of fs, however for lighter atoms such as hydrogen, a smaller timestep is needed to capture the high frequency vibrations.

4.1.3 Neighbour Lists and Cell Lists

The distance between the selected atom and all other atoms in the system are needed to determine which atoms will interact regardless of potential cutoff. This would require calculating the distances between all atoms in the system at each point of the trajectory, quickly increasing computational expense and memory. With the correct timestep, the neighbouring particles (those within the potential cutoff) of the selected atom will not vary significantly, if at all, over 10-20 timesteps. Therefore, to reduce the number of distance calculations, neighbour lists can be implemented in MD simulations, storing atoms within a given cutoff; this cutoff is generally larger than the potential cutoff to ensure that no particle interactions are omitted [96]. These cutoffs are demonstrated in Figure 4.1. The neighbour list will need to be recalculated and updated frequently throughout the simulation.

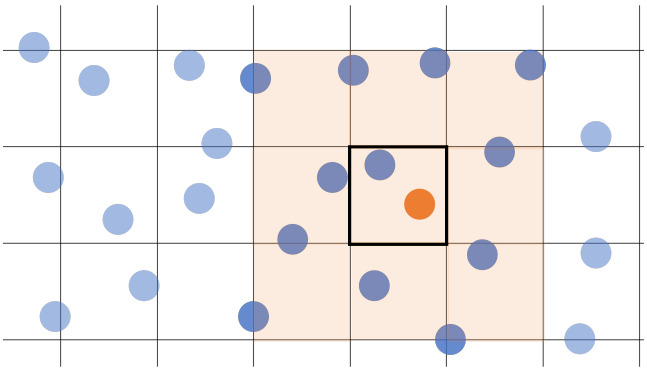

Figure 4.2: *The simulation box is split into numerous cells, with a cell length larger than the potential cutoff, and each atom is assigned a cell based on its coordinates. For the selected atom (orange), interactions with the particles in the same cell and neighbouring cells are calculated. In a 3D simulation, each cell will have 26 neighbouring cells.*

For systems much larger than the potential cutoff, cell lists may be a more efficient method of reducing computational expense [96]. The system is divided into a series of cells, see Figure 4.2, each with a length greater than the potential cutoff. Interaction calculations are then only required between atoms within the same cell and in neighbouring cells. Again, the cell list identifying the atoms within each cell will need to be updated after an appropriate number of timesteps.

4.1.4 Thermodynamic Ensembles

For a system of atoms in statistical equilibrium, the interactions with its environment and the macroscopic constraints imposed upon it will determine the type of ensemble present [97]. If the system is isolated, so no energy or particles are exchanged with the surrounding environment, then the system is in the Microcanonical ensemble, or NVE ensemble. The number of atoms, N, the volume of the system, V and the total energy of the system, E, all remain constant. It is arguably the most fundamental but least realistic of the ensembles considered due to the exclusion of energy fluctuation and interaction with the surroundings.

If the system remains closed but heat exchanges with the environment is uninhibited, the system is now in the Canonical or NVT ensemble. The number of atoms and volume of the system again remain constant, but the exchange of energy means the temperature, T, of the system is now dictated by the temperature of the environment. For a constant volume, the boundaries of the system remain rigid. By implementing flexible boundaries, the volume of the system can change and allows the pressure P to equalise with the environment. This is known as the Isothermal-isobaric system or NPT ensemble. The temperature and pressure of the environment are determined in MD simulations by the thermostat or barostat respectively. As constant pressure is more easily achieved experimentally than constant volume, the NPT ensemble provides slightly more realistic molecular dynamics simulations than the NVT ensemble.

Finally, if matter is also allowed to exchange with the environment and rigid boundaries are again enforced, the system is open and known as the Grand Canonical or μVT ensemble. The chemical potential, μ, will control the number of atoms in the system.

4.1.4.1 Thermostats and Barostats

For both NVT and NPT ensembles, a constant temperature is required. A thermostat is introduced to regulate the temperature in the simulations. Since the temperature of a system is directly related to the kinetic energy,

$$\langle E_k \rangle = \frac{3}{2} N k_B T, \tag{4.10}$$

the simplest method to control temperature is to rescale the velocities to values from the Maxwell-Boltzmann distribution at each timestep. Alternatively, the system can be coupled to a heat bath at the desired temperature which regulates the energy of the system, known as the Berendsen thermostat [98]. It is mostly used for the initial equilibration of the system before a more accurate thermostat, like the Nosé-Hoover thermostat, is used in the production run.

The Nosé-Hoover thermostat [99] includes the thermal bath as an extra degree of freedom s. The potential energy term for the bath is given by,

$$(3N + 1) k_B T \ln(s) \tag{4.11}$$

And the kinetic energy,

$$\frac{Q}{2} \left(\frac{ds}{dt} \right)^2 \tag{4.12}$$

including a fictious parameter Q which can be considered to be the mass of the extra degree of freedom. The equations of motion now produce trajectories with canonical behaviour and reliable thermodynamics properties.

For constant pressure ensembles, a similar process is implemented using a barostat [100] which dictates the pressure of the system by adjusting the volume of the simulation box.

4.1.4.2 Phase Space and Ergodicity

Each particle in a molecular dynamics simulation will have 6 degrees of freedom; 3 coordinates to determine its position and 3 components for its momentum (or velocity). Thus for a system containing N particles, we have a $6N$ dimensional phase space. To correctly compute average properties of the system, this phase space must be sampled correctly. If the system samples only a small region of the phase space, the resulting averages will depend on the initial coordinates and momenta of the atoms. All significant points in phase space must be sampled for the calculation to be independent of its starting set-up and thus ergodic. Ergodicity suggests every atom will visit all possible points in the system and thus the average behaviour of the system can be deduced from the trajectory of a single atom [101].

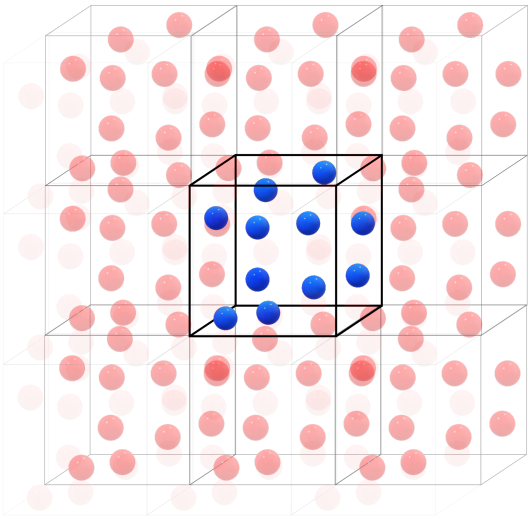

Figure 4.3: *The simulation box (blue) is surrounded by images of itself (red). The periodic array continues infinitely to imitate a much larger system. If a particle is to travel outside the simulation box, it will reappear in the system from the opposite edge.*

4.1.5 Boundary Conditions

The number of atoms required to model a system realistically far exceeds anything that is computationally viable. Instead only a region of the system of interest is modelled. Reducing the size of the system imposes artificial boundaries on the model atoms. A much higher number of atoms will reside at the edges of the simulation boxes, introducing unwanted surface effects into our model. To eliminate unphysical effects such as these, the choice of boundary is important.

There are multiple types of boundary conditions to suit different system scenarios. For a gaseous system with a volume much smaller than the simulation box, no boundary conditions are required. Atoms can be fixed at the boundaries to create rigid boundary conditions which is useful for modelling porous systems. Stochastic boundary conditions also require atoms fixed at the box edges, however they provide an additional thermal conduction pathway, modelling systems where atoms beyond the simulation region will be interacting with atoms in the system [102].

To include the influence of a much higher number of atoms than that being simulated, periodic boundary conditions can be used [103]. By removing the boundaries of the box and linking opposite surfaces together, an infinite array of boxes in each direction is created as demonstrated in Figure 4.3. An atom leaving the system at one edge will re-enter the system through the opposite edge. This allows atoms to interact with periodic images of atoms and thus increasing the number of interactions within the system to a more realistic case. With periodic boundary conditions, it is possible that an atom can interact with its own periodic image or multiple images of the same particle. As this can lead to unphysical effects, it is not wanted in simulations. To overcome this, the

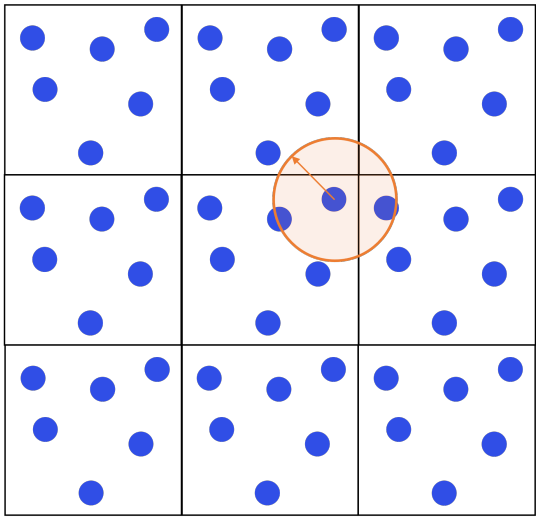

Figure 4.4: *Minimum image convention for periodic systems. The cutoff for potential interactions (orange) should be less than half the simulation box size. This ensures that the atom will not interact with its own image or interact with the same atom more than once across the periodic images.*

minimum image convention is applied [104]. Figure 4.4 shows that by ensuring that the cutoff for atom interactions is less than half the box size, this problem can be avoided.

4.1.6 Ewald Summation

Long-range forces will usually extend far enough that increasing the box size to accommodate them becomes impractical. In particular, the electrostatic interactions for charged particles , which decay with $\frac{1}{r}$, is problematic in atomic simulations but important for modelling charged species and calculating some system properties (e.g. dielectric constant). Directly summing over all the charge-charge interactions in the system is slow to converge and also conditionally convergent; it is dependent on the order in which the terms are considered.

The most widely used method to compute long-range interactions for periodic systems is the Ewald summation [96]. In this method, the summation is split using

$$\frac{1}{r} = \frac{f(r)}{r} + \frac{1 - f(r)}{r} \tag{4.13}$$

to creating two series that converge much more rapidly. A Gaussian charge distribution

$$p_i(r) = \frac{q_i \alpha^3}{\pi^{3/2}} \exp(-\alpha^2 r^2) \tag{4.14}$$

is most commonly used as the function $f(r)$. The summation now consists of the initial point charges and the neutralising Gaussian distribution, both calculated in real space, and a second cancelling charge distribution performed in reciprocal space such as those in Figure 4.5. Correction terms for the Gaus-

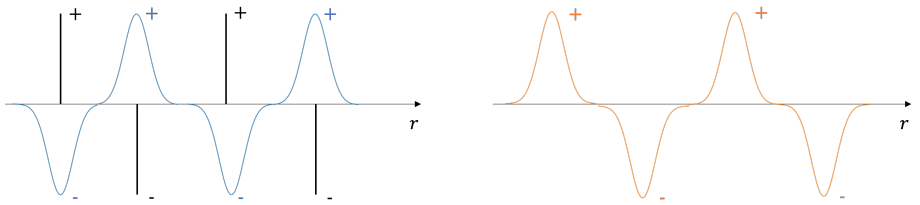

Figure 4.5: *The summations that occur in real space are presented on the left; the original point charges (black) and the associated Gaussian distributions to neutralise the charge (blue). On the right is the cancelling Gaussian charge distribution (orange), the sum of which is performed in reciprocal space.*

sian self-interactions and the surrounding medium must also be included in the calculation.

The rate of convergence for both distributions depends significantly on the width of the Gaussian distribution α: the real space summations converges more quickly with large α but the reverse is true for the reciprocal space summation. Although it is extensively used, the Ewald method is computationally expensive, scaling N^2, or if α is allowed to vary, $N^{3/2}$. It is possible to reduce the scaling using the fast Fourier transform (FFT) algorithm to calculate the reciprocal space summation which scales $N \ln N$. However, discrete rather than continuous data is required for the FFT method. This can be achieved by replacing the continuous point charge coordinates with a grid-based charge distribution. The particle-mesh method is the most popular approach to introduce the discrete charge density and has been improved further to produce the particle-particle particle-mesh (PPPM) technique[105].

4.1.7 Radial Distribution Function

The radial distribution function (RDF) is a measure of structure or order within the simulated system. Distances between all atoms are calculated and the probability of finding a pair of atoms at a distance r is compared to that of a completely uniform distribution. For inequivalent atoms, a and b, the RDF $g(r)$ is given by,

$$g(r) = \frac{V}{4\pi N_f N_a N_b r^2 \delta r} \sum_{frames} \sum_{i} \sum_{j \neq i} \delta(r - r_{ij}) \tag{4.15}$$

where N_f is the number of frames in the simulation trajectory, $N_{a,b}$ is the number of atoms of type a or b, δr is the radius of the sampling shell, described in Figure 4.6, and V the volume of the simulation box. The distribution of atom positions is given by $\delta(r - r_{ij})$.

When considering a liquid system, $g(r) = 1$ indicates a system containing a random distribution of atoms with the same density as the system of interest. Values greater than 1 indicate a higher than expected probability of finding atoms at that distance, r, relative to a uniform distribution. Conversely, $g(r) < 1$ suggests fewer atoms found at the value of r. Order of a system can be measured looking at the number and intensity of peaks produced from the RDF, like the example in Figure 4.7. However at large separation values, the RDF

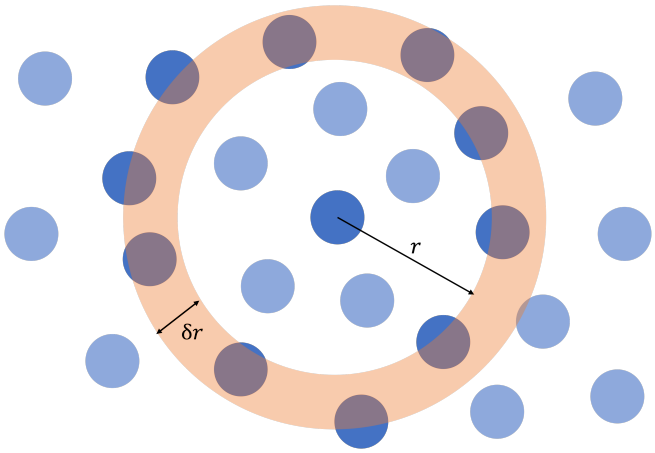

Figure 4.6: *For each atom in the system, the number of particle centres that lie within a distance of r and $r + \delta r$, (orange region), is calculated. Although the graphic depicts a 2D scene, the calculation is generally performed on a 3D system, therefore the orange region represents a spherical shell. The volume of the shell is given by the difference in volume of two spheres with radius $r + \delta r$ and r.*

falls off making long range order more difficult to identify. Additionally, RDFs can be measured experimentally, using X-ray diffraction for example, thereby providing a direct comparison between experiments and simulations of the same system.

4.1.8 Mean Squared Displacement

As the simulations are dynamic, we may want a measure of the movement of particles in a liquid or gas with time. The mean squared displacement (MSD) measures the deviation of a particle from a selected reference position over time[106]. MSD is given by

$$MSD(r) = \left\langle \frac{1}{N} \sum_{i=1}^{N} \left| r - r(t_0) \right|^2 \right\rangle_{t_k} \tag{4.16}$$

for a system with N equivalent particles. For a typical liquid, the MSD will become linear with time and by computing the gradient, the diffusion coefficient, D, can be calculated. At shorter times, the MSD will be more erratic due to particle collisions and will resemble the path of a random walker. A windowed calculation of the MSD is averaged over various values of the lag-time, where the lag-time is less than the length of the trajectory.

4.2 Thermodynamic Integration

Direct measurement of the free energy of a molecular dynamics simulation is not always possible as it does not sample the phase space adequately. Thermal quantities such as this depend on the volume in phase space that the system

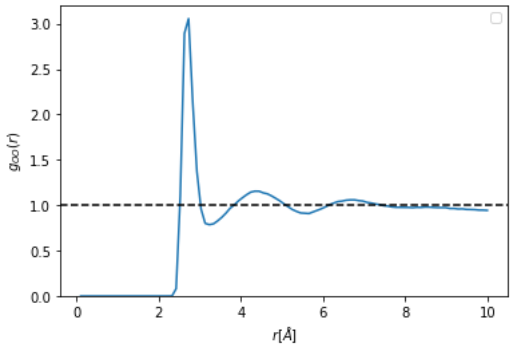

Figure 4.7: *An example of an RDF plot showing the distribution of O-O distances in bulk water at 300K. The initial peak shows the most probable distance between atoms before tending to* $g(r) = 1$*, as is characteristic of liquid systems.*

can access. However it is possible to calculate a free energy difference between states [106].

Free energy cannot be measured experimentally either and so properties related to its derivative with respect to volume or temperature are often determined, such as the pressure or energy of the system. The same procedure can be applied to simulations. The change in free energy between the system of interest and a system of known free energy (e.g. ideal gas phase) can be calculated.

Therefore, free energy difference between state A and state B is determined by

$$\Delta F_A^B = \int_{\lambda=0}^{\lambda=1} \langle \frac{\partial H(\lambda)}{\partial \lambda} \rangle_\lambda d\lambda \tag{4.17}$$

Where λ is a control parameter used to smoothly switch between the systems such that the Hamiltonian is

$$H(\lambda) = (1 - \lambda)H_A + \lambda H_B \tag{4.18}$$

With $\lambda = 0$ equating to state A and $\lambda = 1$ for state B. Numerous simulations are performed with discrete values of λ between 0 and 1 and the average integrand for each value computed. The free energy difference of state A and B can then be computed with numerical integration.

Chapter 5

Ion Ratio and Polymorphism in Amorphous Calcium Carbonate

Amorphous calcium carbonate (ACC) is the least stable polymorph of $CaCO_3$ and is often seen as a precursor to the more stable crystalline phases, calcite, aragonite and vaterite, during nucleation [?]. Both calcite and aragonite are found extensively in nature [107] but aragonite is substantially more difficult to precipitate from solution at ambient conditions than either calcite or vaterite [108].

Aragonite deposited in nature is unlikely to be selected due to the effects of temperature or Mg ions since those conditions are not commonly found. However, it would be possible to regulate the local environment. The ratio $[Ca^{2+}/CO_3^{2-}]$ has been observed impacting the particle size precipitated [109] and the polymorph selected, when implemented in conjunction with other known selection conditions [110].

Experiments performed by Kim and Meldrum have looked at the effect of varying the respective concentrations of Ca^{2+} and CO_3^{2-} in solution. Calcium carbonate crystals were precipitated by mixing equal volumes but unequal concentrations of $CaCl_2$ and Na_2CO_3 and the resulting crystals identified with optical microscopy and SEM imaging. When the concentration of Ca^{2+} was greater than 1mM, predominantly calcite was precipitated alongside small amounts of vaterite. However with Ca^{2+} concentration < 0.5mM, aragonite became the most abundant polymorph and the dominance of the polymorph increased with greater concentration of CO_3^{2-}. At very low concentrations of Ca^{2+} mixed with very high concentrations of CO_3^{2-}, calcite again became the selected polymorph, although a smaller number of crystals were precipitated than seen at high concentrations. The dominant polymorph precipitated and respective concentrations of Ca^{2+} and CO_3^{2-} are detailed in Figure 5.1.

The length scales of the early stages of nucleation are not easily obtained experimentally. Computer simulations can more easily observe at the atomistic

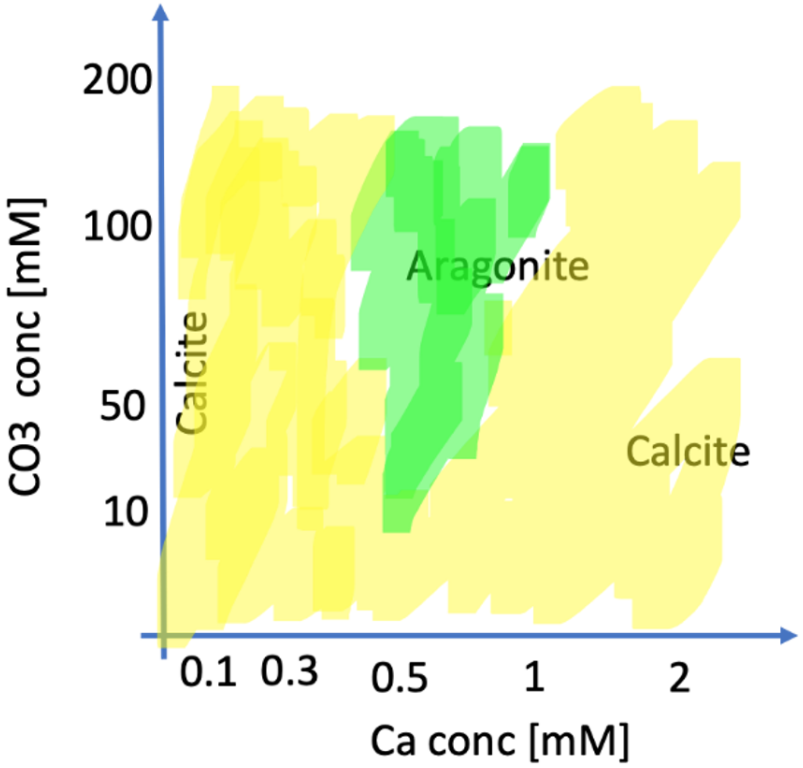

Figure 5.1: *Schematic phase diagram to demonstrate the dominant polymorph produced under varying solution conditions from the work of Kim (currently unpublished). Of particular interest is the region of low* Ca^{2+} *concentration and high* CO_3^{2-} *in which aragonite is precipitated over calcite under ambient conditions.*

level and closely study the movement of ions. Molecular dynamics simulations have therefore been used to model the early stages of the nucleation from ACC. The ratio of calcium to carbonate was varied across the systems studied and the likeness of ion cluster geometries to calcite and aragonite was quantified to identify any "protonuclei" of either polymorph. An influence of the ion ratio on the protonuclei found may suggest preferential conditions for specific polymorph nucleation, such as those seen in experiment, and also the explanation behind the selection.

5.1 Polymorph Identification

Polymorph identification in nucleating systems relies on the assumption that the structure of the forming "nuclei" resembles the structure of the final crystalline phase. Methods are required to identify nuclei-like clusters within our molecular dynamics simulations as well as the ability to identify the polymorph it most closely resembles. With the calcite and aragonite phases of the calcium carbonate systems, there is a clear geometric distinction between the two structures. This enables polymorph identification based on the local geometric structure of atom clusters.

Order parameters are frequently used to quantify the similarity of a cluster's geometry to known bulk phases. The geometric properties employed will likely depend on the system being studied and the chosen method to determine order parameters. There are a variety of methods that have been implemented previously, the advantages of which are system dependent.

5.1.1 Distribution Function Methods

One of the simplest methods to identify polymorphs is utilising the radial distribution function (RDF), the details of which are presented in Section 4.1.7. The resultant peak positions and ion coordinations can be compared between bulk crystal structures and clusters within the system. MD simulations of amorphous calcium carbonate grown from high concentration solutions have used the RDF as a means of comparison with calcite, aragonite and vaterite [111]. ACC clusters exhibited some structural similarity to vaterite and to a combination of both vaterite and aragonite but only at small distances.

A similar study utilised the RDF with a distribution function for the angle, $p(\theta)$, formed by the three nearest-neighbours [112]. By considering only the three nearest-neighbour cations, $p_{cation}(\theta)$, the distribution function was distinguishable for all three crystalline phases. The pure ACC structure was found to most closely resemble vaterite, supporting the findings of the previous study.

Although these methods provide comparison between phases, the similarities are not fully quantified and the visual comparison is often open to interpretation. A definitive and quantifiable method would provide more reliable results.

5.1.2 Machine Learning Methods

With the recent advances and interest in machine learning techniques, identification and classification algorithms have also been applied to aid structural identification in molecular simulations.

One such method has been developed using neural networks and techniques adopted from computer vision as a general approach to identify local structures[113]. Previous efforts to implement machine learning in such a way have been computationally expensive and required a large amount of preprocessing of data. The PointNet architecture (a neural network used for classification) directly processes point clouds, sets of points in 3D space, without the need for preprocessing. For the application to crystal structure identification, point clouds represent the positions of atoms within a given cutoff distance of a central atom and determine the structure relative to that atom. The technique is developed such that the results of the PointNet classification are invariant to global translations and rotations, and the exchange of atoms. The network is trained to identify structures on a large (10^4-10^5) number of pure crystal phases generated from computer simulations. The authors tested the crystal structure identification capabilities of the network on a variety of crystal systems: Lennard-Jonesium, water and mesophase systems, claiming identification accuracies upwards of 92.5%. The technique described in the paper could provide a method to evaluate crystalline structure where simple order parameters are not available.

The previous method using distribution functions has been expanded upon with ML techniques to provide a quantitative likeness[114]. Dimensionality reduction (DR) has been used to evaluate geometrical similarity. DR has previously been used in determining geometric structures such as face recognition. For comparing phase similarities, the geometry of different phases are represented by the pair distribution functions and angular distribution functions, creating multidimensional data. In contrast to the previous method developed by the authors, all possible pair and angle distributions are considered. When applied to $CaCO_3$, there are 24 functions in total, each discretised with 50 data points, resulting in 1200-dimensional data. Then using a DR algorithm, the data is transformed to low dimensional data without a significant loss of information. The similarity between structures can then be compared via the distance between the data points between those phases. Consistent with previous simulations of ACC, the technique found ACC clusters to most closely resemble vaterite and differences in structure were highlighted in the presence of Mg^{2+} and Sr^{2+} ions.

Both ML methods discussed provide a definitive value for the difference in structure between phases. For the study of calcium carbonate, the neural network technique is needlessly complicated when simpler order parameters are available. The DR technique improves on the authors previous methods, however the results are extremely sensitive to the chosen DR algorithm implemented. Although the methods presented provided the same qualitative results, the same may not occur when applied to different systems.

5.1.3 Steinhardt Order Parameters

For metadynamics studies of ordering, Steinhardt bond orientation parameters are often employed. They are a set of parameters based on spherical harmonics which are rotationally and translationally invariant[115]. In the work considered[116], the metadynamics scheme locates nanoparticles of calcium carbonate with crystalline order by identifying minima in the free energy landscape. The Steinhardt order parameters are then used to identify whether the found

phase resembles calcite, aragonite or vaterite. Local order parameters are defined per ion such that

$$q_l^{\alpha\beta} = \left[\frac{4\pi}{2l+1} \sum_{m=-l}^{l} \left| \frac{1}{N_{\alpha\beta}} \sum_{i=1}^{N_{\alpha\beta}} Y_{lm}\left(\theta_i, \phi_i\right) \right|^2 \right]^{\frac{1}{2}} \tag{5.1}$$

where θ_i and ϕ_i describe the angular position of the ith neighbour. The atoms C, Ca and O, are denoted by α and β. The number of neighbours $N_{\alpha\beta}$, of atom type β within a given, predetermined cutoff radius, is a constant for each atom type α.

Five order parameters were used and linear combinations of these calculated for each ion; this value is then compared with reference values for bulk phases. If all the local order parameters lie within 3 standard deviations of the corresponding bulk values, the cluster surrounding the ion can be considered polymorph-like.

For calcium carbonate, the order parameter is fairly straightforward to compute using the above method. At smaller nanoparticle sizes, the order parameter statistics are poor and it is unlikely the technique can be effectively applied to other systems.

A range of polymorph identification techniques are available with varying complexity and appropriate systems. In this work, a novel method has been implemented to identify clusters resembling calcite and aragonite within molecular dynamics trajectories. The method utilises comparisons between distance and angle probability distributions for ion clusters and reference distributions for crystalline phases. Although similar to approaches discussed here, a simpler routine is implemented to provide a value quantifying likeness to the considered polymorphs. A thorough explanation of the novel method is presented below in Section 5.2.

5.2 Manhattan Distance

The Manhattan geometry, or taxicab geometry, defines the distance between two points as the sum of the absolute difference between their Cartesian coordinates such that;

$$d_{man}(\mathbf{p}, \mathbf{q}) = \sum_{i=1}^{n} |p_i - q_i| \tag{5.2}$$

where $\mathbf{p}$ and $\mathbf{q}$ are Cartesian coordinates of dimension n.

As the structures of calcite and aragonite are different at the atomistic level, the C-C distances, d, and the C-Ca-C angles, θ, of a cluster of atoms around a central Ca ion are sufficient to distinguish between the two polymorphs. Exploiting the geometric differences, Finney et al (unpublished) developed a technique to distinguish calcite- and aragonite-like clusters with the Manhattan distance.

For each Ca ion in the system surrounded by 6 carbonates, the average distances and angles of the atom cluster are quantified as discrete probability distributions $\mathbf{P}_\alpha$ and $\mathbf{P}_\beta$ respectively. The same procedure is applied to bulk calcite and aragonite structures to acquire probability distributions, $\mathbf{P}_\alpha^{\mathbf{ref}}$ and

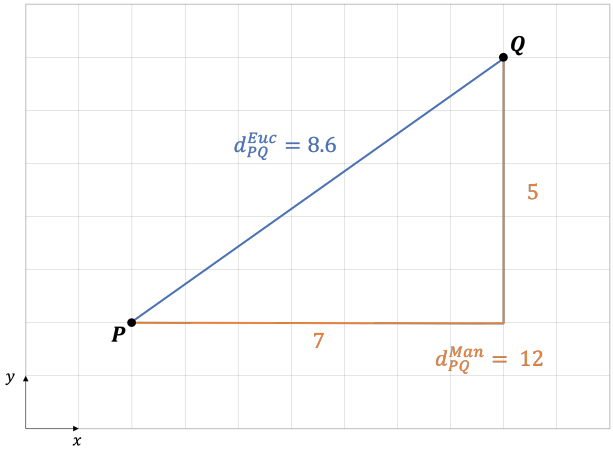

Figure 5.2: *A schematic diagram depicting both the Euclidean and Manhattan distance between two points P and Q. The Euclidean distances takes the shortest possible route between the two points and the resulting length is given by $\sqrt{(q_x - p_x)^2 + (q_y - p_y)^2}$. For the Manhattan distance, the route can only go horizontally or vertically, resulting in a larger distance of $(q_x - p_x) + (q_y - p_y)$.*

$\mathbf{P}_{\beta}^{\mathbf{ref}}$, to be used as reference structures for the crystalline phases. By calculating the Manhattan distance, from Equation 5.2, between the local structure of a cluster and the reference structure, the likeness of the chosen cluster to the polymorph phase can be quantified. For each ion cluster, two different values are returned,

$$s_\alpha = \|\mathbf{P}_\alpha(d) - \mathbf{P}_\alpha^{\mathbf{ref}}(d)\| \tag{5.3}$$

$$s_\beta = \|\mathbf{P}_\beta(\theta) - \mathbf{P}_\beta^{\mathbf{ref}}(\theta)\| \tag{5.4}$$

for the distance and angle, both of which are dimensionless. The closer both s_α and s_β are to zero, the greater the resemblance to the reference structure. For a truly amorphous structure, the values should be roughly equal and far from zero.

5.2.1 Combination to Single Value

As there is some variation within the crystalline structure, mean values of s_α and s_β for bulk calcite and aragonite can be obtained. Assuming a normal distribution around the mean, if the Manhattan distance values calculated for a cluster lie within 3 standard deviations (s.d.) of the mean polymorph values, it can be considered polymorph-like. For ease of analysis, the two values quantifying likeness have been combined into a single value $s_{\alpha,\beta}$ using a choice of three different metrics: the taxicab metric (same as the Manhattan metric but will be referred to as the taxicab metric to avoid confusion),

$$s_{\alpha,\beta} = s_\alpha + s_\beta \tag{5.5}$$

the Euclidean metric,

$$s_{\alpha,\beta} = \sqrt{s_\alpha^2 + s_\beta^2} \tag{5.6}$$

and the Chebyshev metric.

$$s_{\alpha,\beta} = \max(s_\alpha, s_\beta) \tag{5.7}$$

A single value is now used to quantify the resemblance of a cluster to the selected polymorph however the cut-off value at which to classify a cluster as distinctly polymorph-like is more ambiguous. Utilising the previous value of 3 s.d. from the mean value would result in potential polymorph-like clusters being excluded with the taxicab and Euclidean metric. Increasing the value raises issues over what counts as polymorph like; for example the case where only the distance or angle distribution exhibits strong similarity.

Although the method described is specific to the calcium carbonate system, the general procedure could be applied to other systems with well defined and geometrically distinguishable phases.

5.3 Simulation Setup

Ratios of calcium to carbonate, Ca^{2+}/CO_3^{2-}, with values ranging from 4/1 to 1/4, have been investigated. The systems contain no counterions or water so it can be determined whether the ion ratio is influencing polymorph selection as opposed to the effects of counterions or water behaviour. All systems contain at least 10000 Ca^{2+} or CO_3^{2-} ions with the number in the system increased for the other ion to generate unequal ion ratios as shown in Table 5.1.

To model the amorphous state of the systems, Packmol [?] was used to create the simulation boxes. By randomly placing the atoms within the box we can emulate the disordered nature of the systems being studied. The simulation box sizes were varied to try and maintain a consistent density of the system. All systems were investigated with a cubic box and periodic boundary conditions.

Due to the varying ratios of ions and the exclusion of counter ions, our simulation boxes are all charged. The molecular dynamics program chosen to run the calculations, DLPOLY4 [95], includes a correction for charged systems. The Fuchs correction assumes that the divergence caused when a periodic array of charged unit cells is present can be removed by the addition of a uniform background charge of the opposite sign [117].

Molecular dynamics simulations have been run in DLPOLY4. For all simulations the Raiteri forcefield has been used to describe $CaCO_3$ [118]. To ensure the simulation boxes are randomised and to avoid any unrealistic placings of atoms, the systems are heated from 300 K to 3000 K in intervals of 300 K using the NVT ensemble. Each calculation is run for 200 ps using a timestep of 0.5 fs (excluding the 1/1 system which used a timestep of 1 fs) and the Nosé-Hoover thermostat with a relaxation time of 0.5 ps. The system is then held at constant temperature at 3000 K for 2 ns before being quenched back down to 300 K again in 300 K intervals of 100 ps each run.

Once the NVT calculations have been performed, the system is then held at a constant pressure of 1 atmospheres. The NPT simulations were run in 500 ps intervals for 2 ns to 4 ns until the system was suitably relaxed. Production runs to acquire trajectory data for analysis were performed for 2 ns; a sample of ratio systems were run for a further 2 ns. A timestep of 0.5 fs (1 fs for 1/1)

Ca/CO_3 Ratio	No. of Ca^{2+}	No. of CO_3^{2-}	Cell Volume [$Å^3$]	Atom Density [$Å^{-3}$]
4/1	40000	10000	820838	0.0975
3.5/1	35000	10000	796316	0.0942
3/1	30000	10000	769354	0.0910
2.8/1	28000	10000	756792	0.0899
2.6/1	26000	10000	744702	0.0886
2.4/1	24000	10000	730496	0.0876
2.2/1	22000	10000	714720	0.0867
2/1	20000	10000	695980	0.0862
1.8/1	18000	10000	675298	0.0859
1.6/1	16000	10000	659900	0.0849
1.4/1	14000	10000	645967	0.0836
1.2/1	12000	10000	628591	0.0827
1/1	10000	10000	620235	0.0806
1/1.2	10000	12000	858265	0.0676
1/1.4	10000	14000	1014550	0.0651
1/1.6	10000	16000	1088370	0.0680
1/1.8	10000	18000	1138200	0.0720
1/2	10000	20000	1192760	0.0755
1/2.2	10000	22000	1263500	0.0776
1/2.4	10000	24000	1335870	0.0793
1/2.6	10000	26000	1408710	0.0809
1/2.8	10000	28000	1481620	0.0823
1/3	10000	30000	1558040	0.0834
1/3.5	10000	35000	1742630	0.0861
1/4	10000	40000	1938650	0.0877

Table 5.1: *Number of Ca^{2+} and CO_3^{2-} ions in each system as well as the associated simulation box volume.*

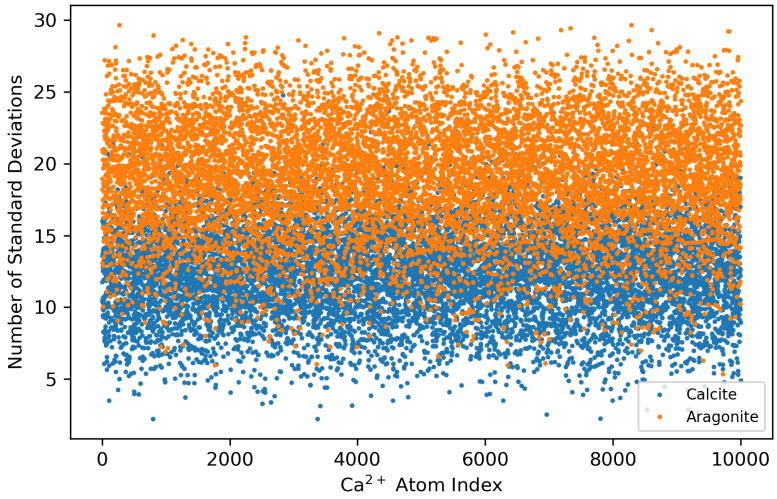

Figure 5.3: *Distribution of similarity to calcite and aragonite quantified with the Manhattan distance analysis for Ca^{2+} ions in the $1Ca/1CO_3$ system.*

was used and the Nosé-Hoover thermostat and barostat with relaxtion times of 0.5 fs and 1 fs respectively. The calculations were run across MMM's Young as well as ARCHER and ARCHER2.

5.4 Results

5.4.1 Polymorph Identification with Manhattan Distance Method

The similarity of the structure around the ion to both calcite and aragonite is quantified using the Manhattan distance analysis. For each Ca^{2+} ion in the system, values of s_α and s_β have been calculated. Mean values of s_α and s_β for calcite and aragonite have previously been calculated: $s_\alpha^{cal} = 0.19$, $s_\beta^{cal} = 0.15$, $s_\alpha^{ara} = 0.17$, $s_\beta^{ara} = 0.13$, with standard deviation values of: $\sigma_\alpha^{cal} = 0.062$, $\sigma_\beta^{cal} = 0.056$, $\sigma_\alpha^{ara} = 0.055$, $\sigma_\beta^{ara} = 0.045$, since the crystal structure can vary slightly. If both s_α and s_β for an ion lie within 3 standard deviations of the mean values for a polymorph, the cluster around the calcium ion is classified as resembling the respective polymorph. An example of the quantified similarity in terms of standard deviation for the equal ratio system is displayed in Figure 5.3. Each data point represents a single ion at a single timestep and shows the number of standard deviations away from the calcite and aragonite reference structure. The calcite values are much lower than the aragonite values although nearly all ion clusters are beyond anything that could be considered polymorph like.

Two similarity measurements, for the distances and angles, are required to quantify polymorphs. Three different methods have been implemented to combine the values into a single quantity describing the similarity of the ion cluster

geometry. The lower the value, the greater the resemblance to the respective polymorph. The taxicab metric, Euclidean metric, and Chebyshev metric (see Section 5.2.1)were all used as combination methods. The point at which to classify a cluster as polymorph-like was now more ambiguous. However 4 standard deviations away from the mean value of $s_{\alpha,\beta}^{cal,ara}$, the reference values, was determined as the cut-off. This encompasses the majority of ions that would show likeness and omit the cases where only the distance or angle distribution exhibit similarity.

Due to the mathematics of the metrics, the taxicab method always produces the largest values and the Chebyshev method the lowest. However the general pattern produced and the comparison between calcite and aragonite results remains the same for each method. The Chebyshev metric is the most reliable as it will only include ion clusters where both the distance and angle order parameters lie within the normal distribution range. The other two methods may include clusters where the distance probability distribution shows a very strong resemblance but the angle distribution resemblance is much weaker and vice versa.

5.4.2 Similarity Distribution

The number of standard deviations away from the mean values for all systems is far greater than any structure that would be considered calcite- or aragonite-like. The data for both polymorphs across all respective methods run roughly anti-parallel to one another, detailed in Figure 5.4. This suggests that an ion cluster can only show resemblance to one of the polymorphs and that the inhibition of formation for one polymorph promotes the nucleation of the other and vice versa. The preference for aragonite observed at high CO_3^{2-} concentrations in experiment may in fact be due to the inhibition of calcite nucleation, similar to the promotion of aragonite precipitation in the presence of Mg^{2+} ions being a consequence of hindering calcite precipitation.

Looking below 4 standard deviations away, in Figure 5.4(b), focuses on the clusters that show strong resemblance to the polymorphs. There are very few clusters identified within this region. At high CO_3^{2-} ratios, no calcite- or aragonite-like clusters were found. At high Ca^{2+} ratios, no clusters showing similarity to aragonite were seen but there were still some calcite-like clusters present in the system. In the cases where there are low values for aragonite, very few clusters are actually present and the low values are skewed by one or two anomalous ion clusters with a strong resemblance to aragonite.

5.4.3 Average Number of Crystals

Continuing to focus on calcite- and aragonite-like clusters, the average fraction of Ca^{2+} ions that would be classified as crystal-like across the simulation run

$$\text{Average Polymorph Fraction} = \frac{\text{Number of polymorphs present across all frames}}{\text{Number of frames} \times \text{Number of } Ca^{2+}\text{ions}} \quad (5.8)$$

has been calculated using the three combination methods.

At each timestep in the trajectory, a Ca^{2+} ion and its surroundings are classified as calcite-like, aragonite-like or neither. Atom density, the total number

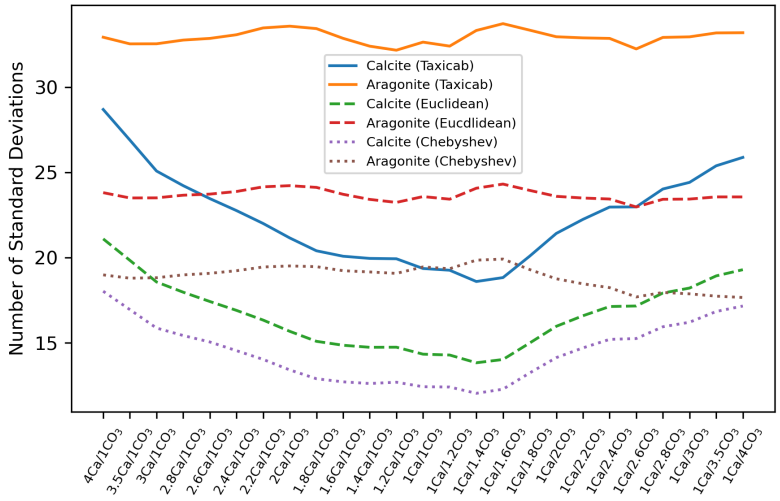

(a) *All standard deviation values*

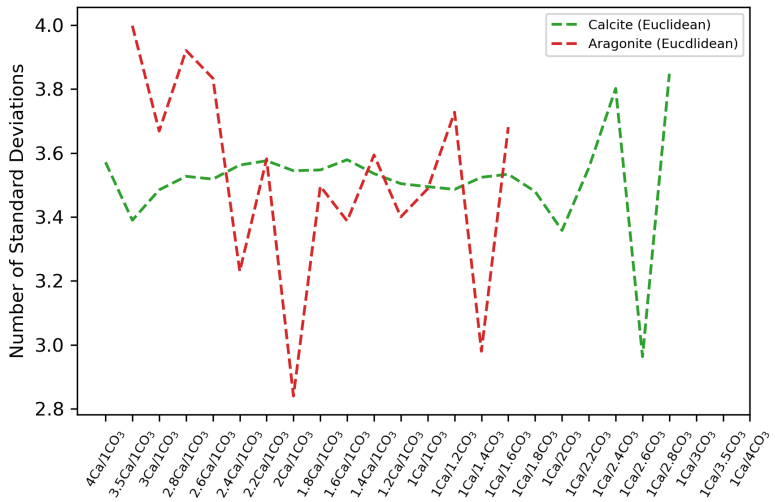

(b) *Under 4 standard deviations*

Figure 5.4: *The median value of the Manhattan distance similarities for calcite and aragonite. The three different combination methods are shown; Taxicab (solid line), Euclidean (dashed line) and Chebyshev (dotted line).* (b) *shows the median value under 4 standard deviation, the region in which the clusters are considered polymorph-like. Only the Euclidean combination is shown but the other methods show similar patterns. No calcite-like clusters are found at high carbonate content beyond ratios of* $1Ca/2.8CO_3$ *and no aragonite-like cluster are found beyond* $1Ca/1.6CO_3$ *ratios or at the* $4Ca/1CO_3$ *ratio.*

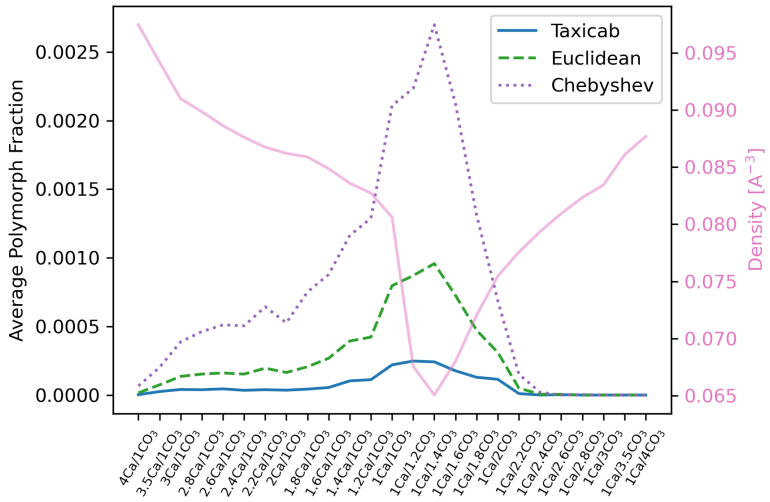

(a) *Calcite*

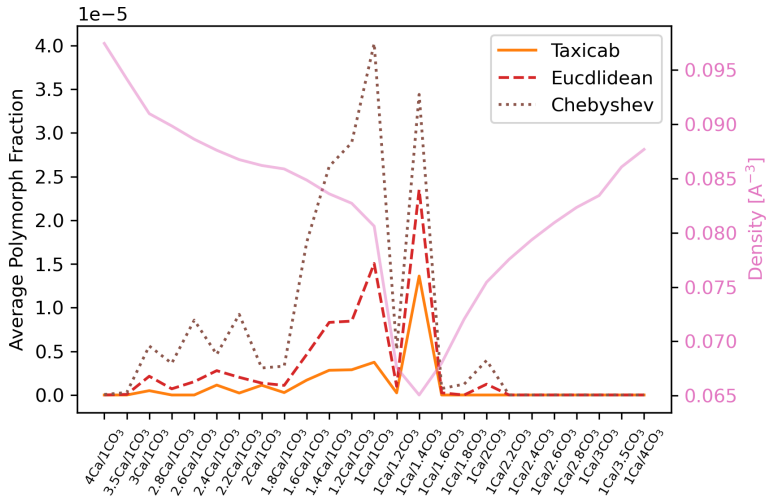

(b) *Aragonite*

Figure 5.5: *Average number of* (a) *calcite and* (b) *aragonite polymorphs across the simulation run alongside the density of the system in terms of number of atoms. The variation in density arises from altering the ion ratios systematically.*

of atoms independent of size over the simulation box size, was then compared with the average polymorph fraction.

The fraction of ion clusters classified as either polymorph is small for all methods; 1×10^{-3} to 1×10^{-4} for calcite and 1×10^{-5} to 1×10^{-6} for aragonite. In all instances shown in Figure 5.5, the fraction of aragonite-like clusters is smaller than calcite-like clusters. For both polymorph types, the highest fraction of clusters identified occurs slightly off the 1/1 ratio at 1/1.4, the system with the lowest atom density. As the amount of Ca^{2+} in the system rises, the fraction of identified polymorph decreases and the atom density increases. The same occurs with increasing CO_3^{2-}, however the decline in fraction of polymorphs found is significantly more rapid than moving to high Ca^{2+} systems. At large amounts of either ion, almost no polymorph-like clusters are seen.

Since the highest fraction of polymorph-like clusters was identified at the lowest atom density, it is possible that the extra volume available to the ions in these systems allowed the atoms to more easily rearrange and order themselves into the crystalline structures. With increasing atom density, less space is available to rearrange therefore inhibiting the formation of crystalline-like clusters. The preference for aragonite in high carbonate systems observed in experiment could be due to the inhibition of nucleation. Although both calcite and aragonite formation are hindered, it is possible that aragonite will eventually be able to form over calcite due to its lower interfacial energies. The current work focuses only on the kinetic effects present in the early stages of nucleation but the thermodynamic effects also need to be considered.

5.4.4 Cluster Lifetimes

The total lifetime of a polymorph cluster within the simulation is defined as the total number of timeframes at which a cluster is identified as polymorph-like at any point in the run, converted into picoseconds. Maximum lifetime of a cluster is the maximum number of consecutive timeframes that the cluster exists for and is quantified as showing similarity to a polymorph within the simulation. The relative stability of a single polymorph cluster is then quantified by comparing its two associated lifetimes, resulting in the lifetime fraction.

$$\text{Lifetime Fraction} = \frac{\text{Maximum consecutive timeframes cluster exists}}{\text{Total timeframes cluster is present}} \tag{5.9}$$

Both total and maximum lifetimes are approximately two orders of magnitude larger for calcite than aragonite across all cases where clusters were detected as shown in Figure 5.6 but the lifetimes are all very small (< 0.2 ps) given the length of the simulation trajectory (2 ns). For calcite, there is only a small amount of variation in the fraction lifetime and on average the maximum time a cluster exists for at once is roughly half of the clusters total lifetime. On the other hand, there is much greater variation in the aragonite fraction lifetimes, this is again due to very few clusters present providing poor statistics. There are a few instances where the maximum lifetime is equal to the total lifetime, suggesting the when an aragonite cluster forms it will more likely stay around than the calcite clusters. However the time for which is the aragonite clusters exist are all shorter than for calcite, so it is not possible to say they are more stable.

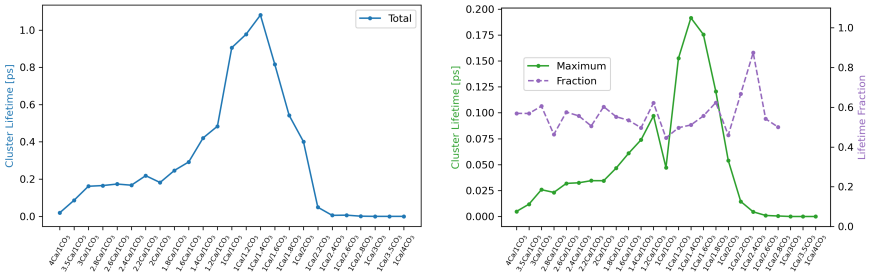

(a) *Calcite*

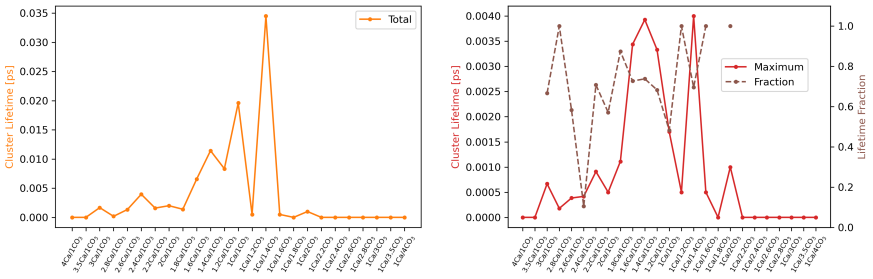

(b) *Aragonite*

Figure 5.6: *The average total cluster lifetimes (left) alongside the average maximum and fraction lifetimes (right) for calcite* (a) *and aragonite* (b) *across all systems.*

5.4.5 ACC Structure and Coordination

RDF

Varying the ratio of Ca^{2+} to CO_3^{2-}, as expected, alters the global structure of the ACC system. A systematic shift in the structure occurs as the amount of Ca^{2+} is decreased and the amount of CO_3^{2-} increased, illustrated by the radial distribution function (RDF) of calcium to calcium, carbon and oxygen, shown respectively in Figures 5.7(a), 5.7(b) and 5.7(c). Increasing the amount of CO_3^{2-}, reduces the long-range structure in the system as the space available for the ions to rearrange and order is limited.

The double peak present in the RDF for the Ca-C distance at the 1/1 ratio (Figure 5.7(b), red line) indicates that both monodentate and bidentate binding are present in the system and occurring with equal probability. Monodentate binding refers to binding with a single O atom on a CO_3^{2-} ion whereas for bidenetate, two of the three O atoms are bonded as exhibited in the examples in Figure 5.8. Monodentate binding has a longer Ca-O distance than the distance for bidentate binding.

As the quantity of Ca^{2+} in the system rises, bidentate binding becomes more prominent than monodentate. Whereas for decreasing Ca^{2+} (and increasing CO_3^{2-}), there is a shift from predominantly bidentate binding to almost exclusively monodentate binding.

Oxygen Coordination

To confirm the suggestions of the RDF data, the number of mono- or bidentate binding exhibited around the individual Ca^{2+} ions within the system was calculated. Within a range of 4Å, the number of O atoms surrounding a Ca^{2+} ion were counted. It was then determined whether the O atoms present belonged to the same CO_3^{2-} ion. If the O within the range was the only one from a particular CO_3^{2-} ion, it was classified as monodentate. If two O atoms came from the same CO_3^{2-} ion, they were classified as bidentate. On the rare but still possible situation in which all oxygens from a CO_3^{2-} ion were positioned within the given range of the Ca^{2+} ion, they are classified as tridentate. The average classification of ion binding in each system, see Figure 5.10, confirms the global findings of the RDF data at a local level. Monodentate binding is most prevalent in high CO_3^{2-} systems and bidentate binding is almost non-existent at these ratios. With increasing amounts of Ca^{2+} ions, bidentate binding becomes more significant and less monodentate binding occurs. At the highest Ca^{2+} ratios, some tridentate (according to our definitions) binding exists in the system. Calcite exhibits exclusively monodentate binding whereas aragonite contains a mixture of mono- and bidentate binding, as can be seen in their structures in Figure 5.9. From our analysis of binding types, calcite would be favoured at high CO_3^{2-} content as no bidentate binding is present. However we also need to consider the O coordination.

As the amount of CO_3^{2-} in the system increases across the systems, the O coordination rises due to the increased availability of O atoms in the CO_3^{2-}. Aragonite has a higher coordination number, 9, than calcite, 6. Since the coordination number tends to that of aragonite with increasing CO_3^{2-}, the preference for aragonite in high CO_3^{2-} systems in experiment may simply be due to the abundance of O available and the local structure around a Ca^{2+} ion having the

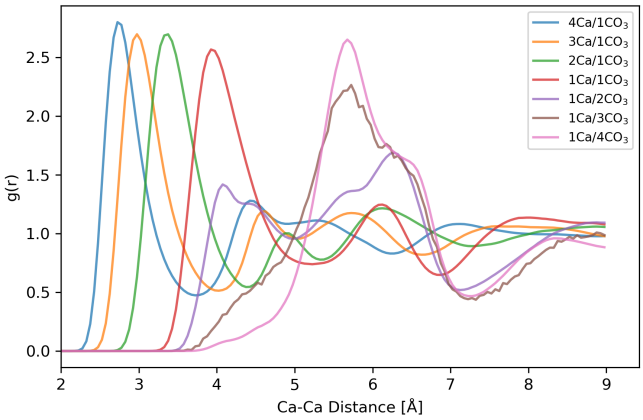

(a)

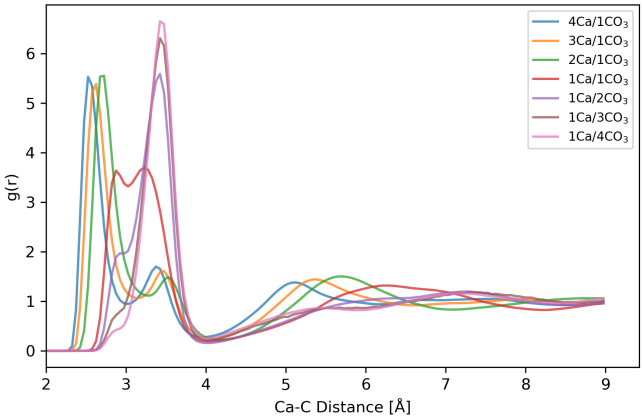

(b)

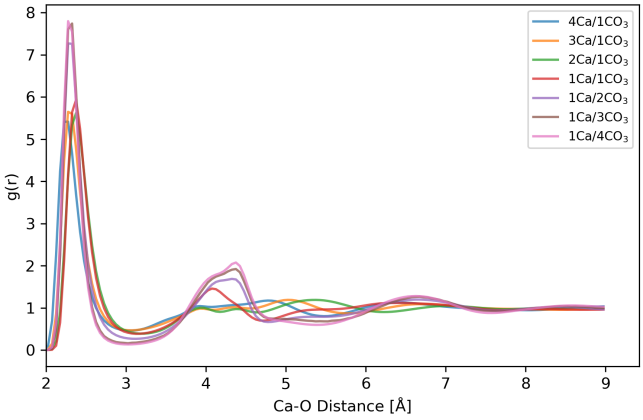

(c)

Figure 5.7: *Radial distribution functions for Ca-Ca, Ca-C and Ca-O variation with differing ion ratios.*

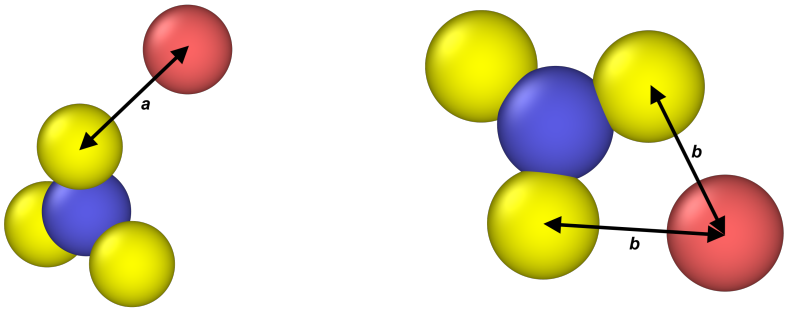

(a) *Monodentate* (b) *Bidentate*

Figure 5.8: *Schematic diagrams to show* (a) *monodentate binding with Ca-O distance* ***a*** *and* (b) *bidentate binding with Ca-O distances* ***b***.

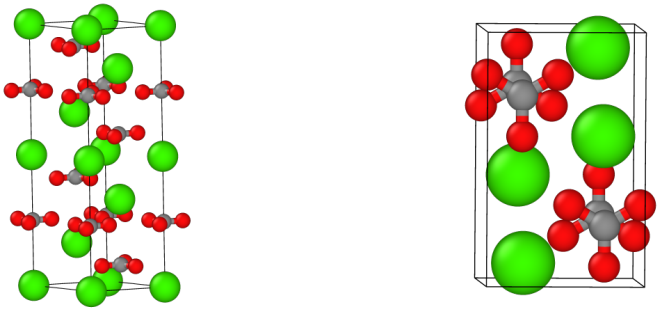

(a) (b)

Figure 5.9: *Atomic structures of* (a) *calcite and* (b) *aragonite. The atoms Ca, C and O are coloured green, grey and red respectively.*

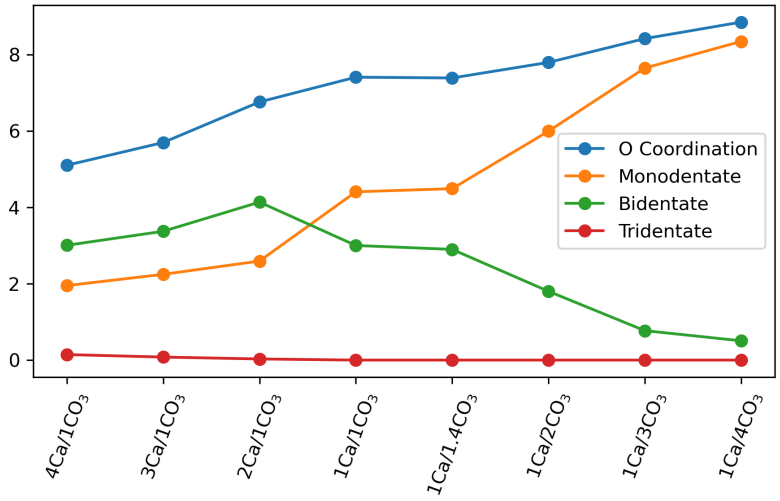

Figure 5.10: *Variation of oxygen coordination and binding type across different ratio systems.*

correct number of O atoms required for the aragonite crystal geometry. There are very few Ca^{2+} ion structures with a coordination greater than 9 [119] so it is possible that with increasing CO_3^{2-}, the coordination number will stay at that of aragonite, even at the high ratios used in the experimental work. Calcite-like formation may also be suppressed less quickly with increased Ca^{2+} than with those with more CO_3^{2-}, as shown in Figure 5.5, in the systems as the coordination remains at around 6; that of the calcite structure.

5.5 Conclusions

Molecular dynamics calculations have been performed on anhydrous amorphous calcium carbonate systems with varying ratios of Ca^{2+} and CO_3^{2-} ions. A novel method of polymorph identification based on the Manhattan distance metric has been implemented to determine the geometric similarity of ion clusters to calcite or aragonite, and establish if the ion ratio has influenced polymorph selection.

Nucleation occurs over a much longer period of time than the length of the simulations studied here. Therefore the number of polymorph-like clusters identified across all systems is very small but we can still determine some possible conclusions. The highest fraction of both calcite-like and aragonite-like clusters occurs just off the 1/1 ratio in the 1/1.4 system, which is also the ion ratio at which the atom density is lowest. Both global and local structure suggest bidentate binding is more prominent in high Ca^{2+} systems whereas monodentate binding is more prevalent in high CO_3^{2-} systems along with an increase in O coordination. By increasing the quantity of either Ca^{2+} or CO_3^{2-}, nucleation is eventually reduced and reduced more rapidly with increased CO_3^{2-}. The distribution of similarity to the reference structures across all ions suggests it is likely that the promotion of nucleation of one type of polymorph will inhibit it

in the other polymorph.

Experimentally, it has been shown that a preference for aragonite over calcite is present in systems with high amounts of CO_3^{2-}, substantially higher than possible to model using the current method. From our investigations at much lower levels of CO_3^{2-} ion, we can infer that the preference with abundant CO_3^{2-} could be due to the increased amount of O available, closer to the coordination number of aragonite, and the inhibition of calcite nucleation allowing the promotion of aragonite formation. It is also possible that the space accessible in the system for the atoms to rearrange will also encourage a greater number of ion clusters to nucleate into crystalline structures.

Since very few clusters were identified and classified as showing similarity to polymorph crystals, continuing the analysis to larger and longer systems could confirm the conclusions drawn here, as well as negate any possible size effects. Additionally, more realistic simulations would include water as well as possibly including counter ions in the solution.

Chapter 6

Amorphous Calcium Carbonate and Water

Water is known to affect the nucleation of crystalline phases from ACC, however the process is still not well understood [82,85]. Nearly all stable forms of ACC found in nature contain water [80]. Furthermore, ACC often precedes the anhydrous crystalline forms during the nucleation process for calcite and aragonite [2].

With molecular dynamics simulations, we can more easily observe the influence of water on the process of nucleation from ACC. It is still debated as to how this process occurs; through dissolution of the ACC and reprecipitation as the ordered form [34] or aggregation of ACC clusters into a large pre-nucleation cluster then organising into the crystal form [84]. We are therefore looking at the very early stages of calcite and aragonite nucleation from the amorphous state. ACC is shown to exhibit some short-range order despite being amorphous. We can assume that if an ACC cluster shows some short-range order resembling the calcite or aragonite structure, it is likely to nucleate into the respective form.

By varying the water content, we can investigate if and how the presence of water affects the selection of calcite and aragonite during the nucleation process. There is a question as to whether the amount of water in the system alone is enough to determine polymorph selection or if further aspects of the water molecules' behaviour is more influential.

6.1 Simulation Setup

Previous modelling work has looked at small systems of ACC and water containing 2800 formula units of $H_2O_x(CaCO_3)_{1-x}$ with $x = 0,0.1,0.2,0.5$ simulated in DLPOLY [95]. The Manhattan distance analysis (see Section 5.2) was used to identify any calcite- or aragonite-like ion clusters. Initial results from this investigation suggest that calcite is more readily formed than aragonite in these configurations. However there is a possible influence from the size of the simulation cell affecting the results. To support the previous calculations, MD simulations have been performed on larger systems containing 10000 formula units.

ACC and water configurations were created using Packmol [?] to randomly

pack molecules into the simulation cell, imitating the disorder present in the amorphous material. The amount of water in the system was varied from none to half in increments of 10% causing the resulting boxes to vary in size but maintain the same density. The percentages refer to the number of molecules in the system i.e. for 50% the system contained 5000 $CaCO_3$ molecules and 5000 H_2O molecules. For each water content, 5 different starting configurations were created and run in DLPOLY4. The simulations followed the same procedure as the ion ratio configurations except with a timestep of 1fs; the systems were heated from 300 K to 3000 K in 200 ps increments before quenching back down to 300 K in 100 ps runs, all performed in the NVT ensemble. Production run simulations were then calculated with the NPT ensemble creating 2ns of trajectory data for analysis, after sufficient convergence. Raiteri's carbonate forcefield [118] was again implemented as well as the SPC/Fw model for water [120]. The MD calculations were run across local machines, ShARC and Bessemer, as well as ARCHER2 and its predecessor ARCHER.

6.2 Results

Using the resultant trajectory data, the Manhattan distance analysis was performed to locate any calcite- or aragonite-like clusters of ions and quantifying the resemblance of all Ca^{2+} ion surroundings to the reference distributions.

6.2.1 Vacuum Gap

During the heating process, vacuum gaps appeared in the system as demonstrated in Figure 6.1. The size of the gap is related to the amount of water in the configuration; with the size of the gap increasing with water content and no vacuum appearing in the anhydrous system. In addition to the appearance of the vacuum gaps, there is also a separation of the calcium carbonate ions and the water molecules. The water molecules surround the vacuum gap leaving large regions of pure calcium carbonate and not a homogeneous system as expected. These vacuum gaps have appeared due to the heating process causing the water to evaporate and the size of the simulation boxes being too large. The extra volume available in the system allows both easier movement of the water molecules and space for the vacuum gap to reside.

Despite the unexpected appearance of the vacuum gaps, polymorph identification has still been performed on the systems. The average number of polymorphs for all configurations is shown in Figure 6.2 across each different starting configuration, (a)-(e), and their combined average, (f). An ion cluster was considered calcite- or aragonite-like if its Manhattan distance values for both C-C distance and C-Ca-C angle were within 3 standard deviations of the respective bulk reference values. In all cases, calcite is the most dominant polymorph, although the number of polymorph-like clusters is incredibly low, with at most 0.06% of the ions in the system being classified as calcite-like. For aragonite, the percentages are at least a magnitude smaller and in some instances, no aragonite-like clusters were identified. There is very little to conclude in how the water content affects polymorph selection in these systems with a vacuum interface present.

For all Ca^{2+} ions with 6 surrounding CO_3^{2-} ions, Manhattan distances values

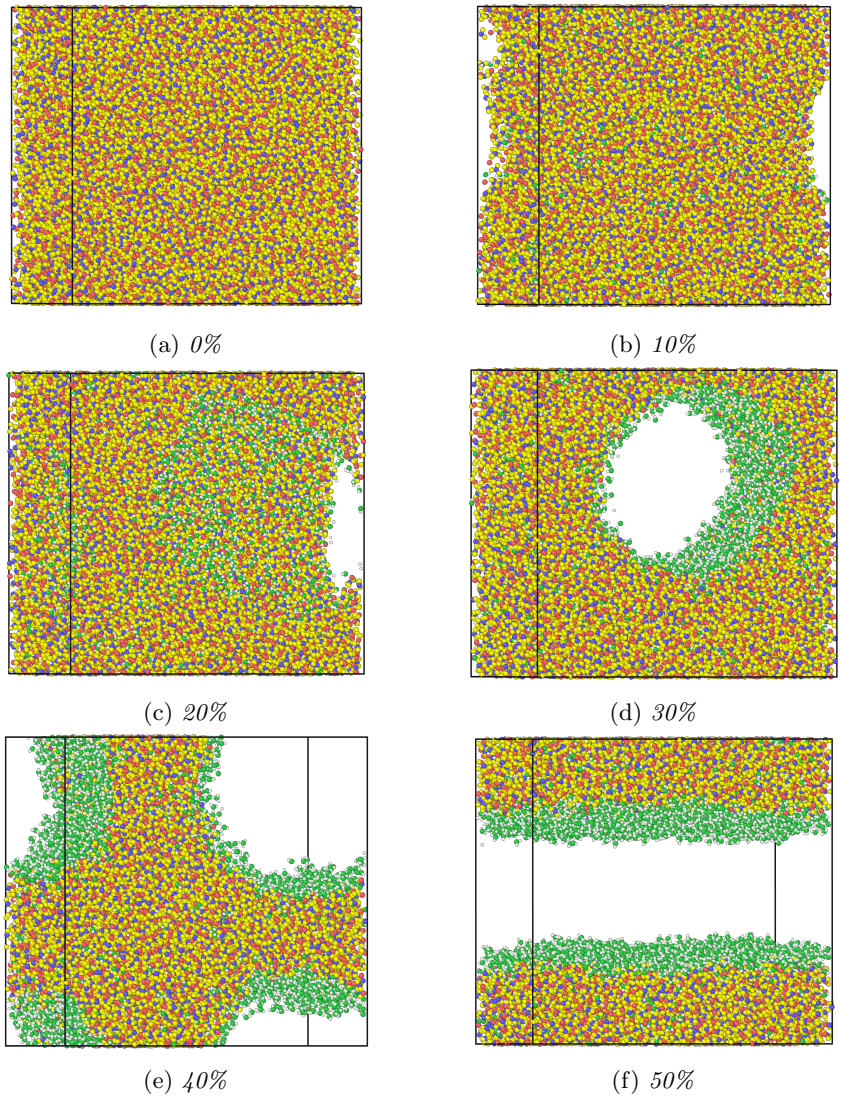

(a) *0%* (b) *10%*

(c) *20%* (d) *30%*

(e) *40%* (f) *50%*

Figure 6.1: *Vacuum gaps and separation of molecules in the different ACC and water systems. The Ca, C and O are coloured in red, blue and yellow respectively. The water molecules are shown in green.*

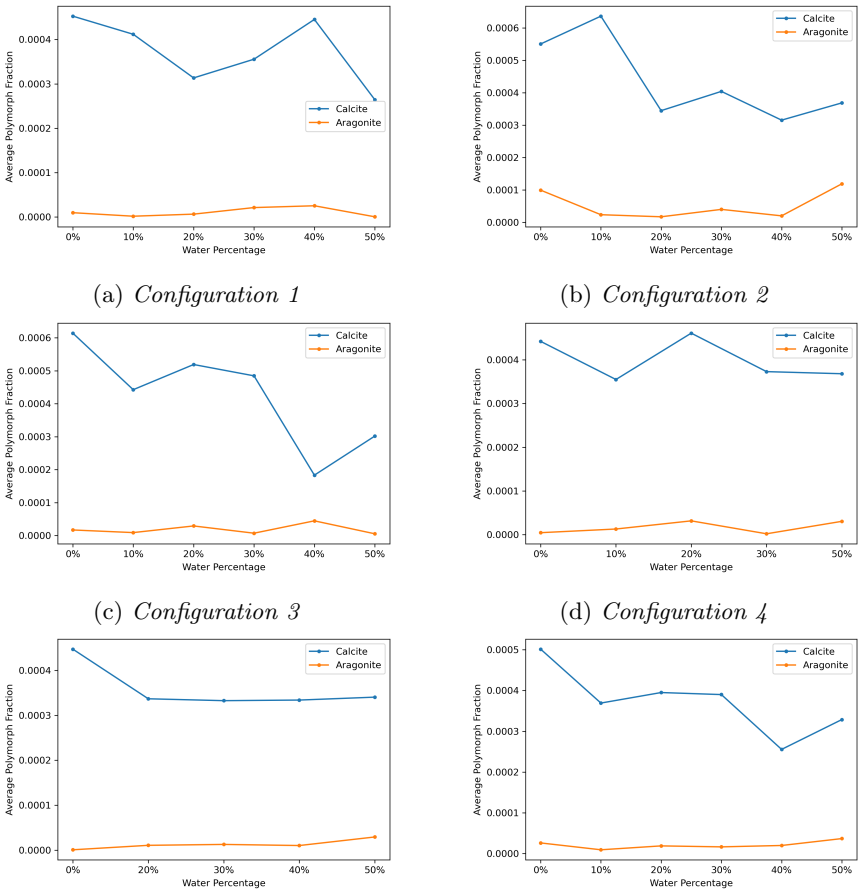

(a) *Configuration 1*

(b) *Configuration 2*

(c) *Configuration 3*

(d) *Configuration 4*

(e) *Configuration 5*

(f) *Combined Average*

Figure 6.2: *The average number of calcite- and aragonite-like polymorphs identified across all systems. Data points for 40% and 10% are missing in configurations 4 and 5 respectively due to simulation stability.* (f) *shows the average across all the different starting configurations*

have been calculated for the distance and angle. As with the ion ratio work in Chapter 5, these values have been converted to the number of standard deviations away from the mean values for bulk calcite and aragonite, as such,

$$sd_{\alpha,\beta} = \frac{|s^{ref}_{\alpha,\beta} - s_{\alpha,\beta}|}{\sigma^{ref}_{\alpha,\beta}} \tag{6.1}$$

where $s^{ref}_{\alpha,\beta}$ and $\sigma^{ref}_{\alpha,\beta}$ are the mean and standard deviation values for the selected reference polymorph, calcite or aragonite. The individual values for sd_α and sd_β are combined into a single value using the taxicab, Euclidean and Chebyshev metrics. The median standard deviation values are displayed in Figure 6.3. Unlike the ion ratio results, there is not a clear anti-parallel relationship between the calcite and aragonite distributions, although there is some present in the Chebyshev combination in configurations 2 and 5. There is however little variation in the low water content values (up to 20%) and considerably more variation as the water content increases.

6.2.2 Comparison

New configurations with smaller simulation box volumes were created using Packmol and the heating process was not applied. Alternatively, the NVT calculations were performed at 300 K for 1 ns and no vacuum gaps appeared during the simulation. The 50% system is presented in Figure 6.4 and shows the water molecules distributed throughout the simulation cell; the same applies for the other water content systems.

For the systems without a vacuum gap and separation of molecules, the Manhattan distance analysis has again been applied. The average number of polymorphs identified in the system is compared for the systems with and without a vacuum gap in Figure 6.5. In both cases, calcite is always the more dominant polymorph. Although of roughly the same magnitude, the number of polymorph-like clusters is slightly higher in the presence of the vacuum gap for both calcite and aragonite. However, the vacuum gap systems show a general decrease in calcite-like clusters with increasing water content, whereas the reverse is true for the systems without the vacuum and separation. There is less of a trend present for aragonite but there is only a very small number of aragonite-like clusters found and so the statistics would not be as reliable.

The contrast between the systems with and without the vacuum gap becomes more apparent when investigating the distribution of polymorph similarity. In Figure 6.6(a), the combined values in terms of standard deviation are shown across the systems. Each combination shows an almost linear relationship as the median standard deviation distance value increases slightly with water content. The magnitude is the same, but there is no deviation from the linear relationship at high (more than 30%) water contents as seen with the vacuum gaps in Figure 6.3. At high water contents, the vacuum gaps are larger and the separation of molecules is more distinct, which will have more influence on the results than the systems with fewer waters present. With no vacuum gap, this is not seen and thus it is clear that the presence of the vacuum and the molecule separation are in some way influencing polymorph selection.

Figure 6.6(b) also shows the distribution of values below 4 standard deviations therefore only showing the clusters we would considered polymorph-like.

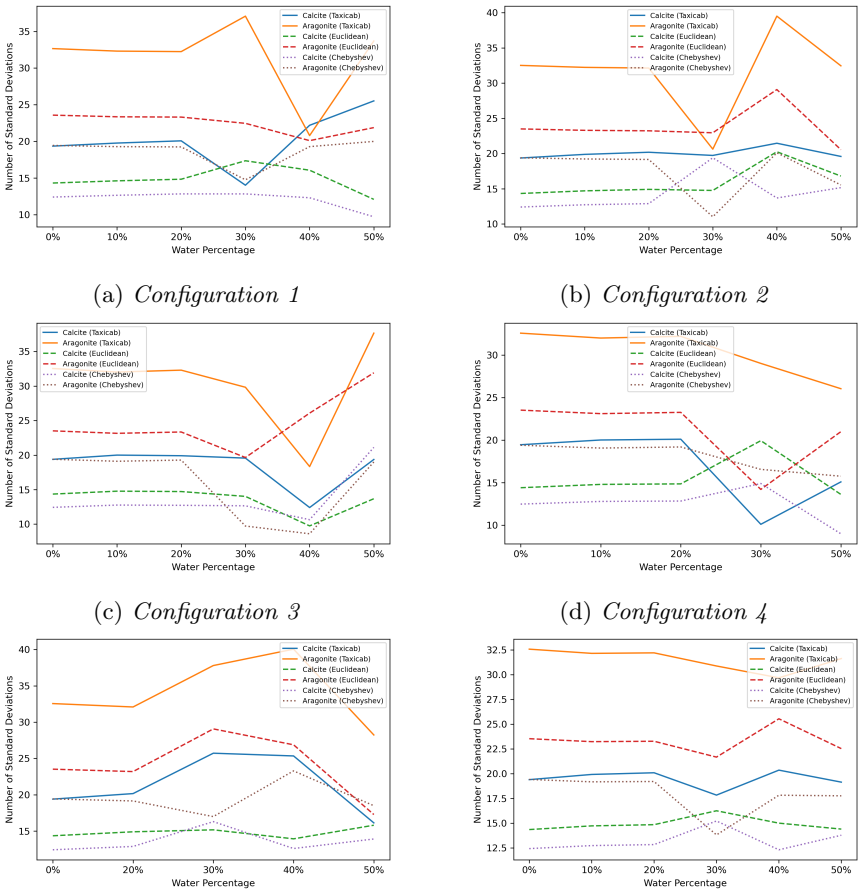

(a) *Configuration 1*

(b) *Configuration 2*

(c) *Configuration 3*

(d) *Configuration 4*

(e) *Configuration 5*

(f) *Combined Average*

Figure 6.3: *Median number of standard deviations away from the mean values for calcite and aragonite. Distance and angle similarities are combined with the taxicab, Euclidean and Chebyshev metrics.* (f) *shows the mean value across all starting configurations.*

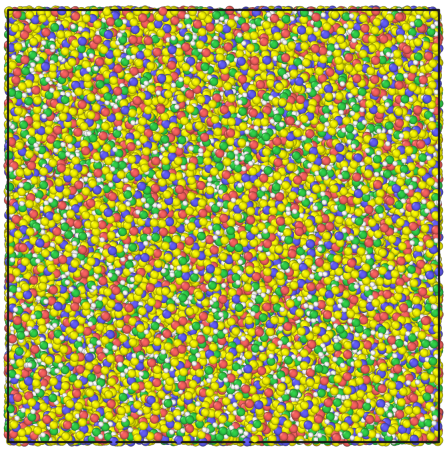

Figure 6.4: *Mixed amorphous calcium carbonate and water molecules for the 50% system. No vacuum gap or separation appears.*

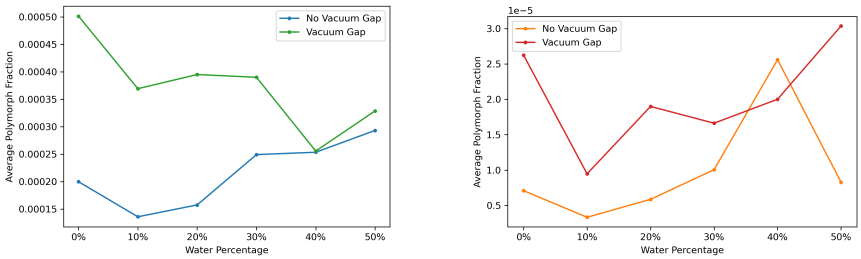

(a) *Calcite* (b) *Aragonite*

Figure 6.5: *Comparison of the average number of polymorphs for the respective systems with and without the vacuum gap.*

There is less that can be interpreted from the data, again due to the poor statistics. Nonetheless, despite fewer polymorphs being identified without the vacuum gap, there was always at least one aragonite-like cluster, which was not the case for the vacuum gap and separation systems.

We have determined that there is a difference between the polymorph selection in the two different system types. However there are multiple factors that could be causing the difference:

- The presence of the vacuum gap acting as an interface that influences polymorph selection in calcium carbonate,
- Differing local ion environments; dense regions of water or calcium carbonate verses the homogeneous mix of the two,
- Movement of water molecules during the separation process.

The following simulations and analysis aimed to determine which of these factors resulted in our differing results.

6.2.2.1 Interface

To establish if the presence of the vacuum interface alone was causing a difference, a vacuum gap of the same size seen in Figure 6.1(f) was inserted into the mixed 50% water system, as shown in Figure 6.7. This way the vacuum gap is present without the separation of the molecules.

The distribution of polymorph similarity for all systems with equal amounts of calcium carbonate and water are compared in Figure 6.8. There is a large variation in the median value for the systems with a vacuum gap, particularly when identifying aragonite-like clusters. As highlighted in Figure 6.8, there is very little difference in the number of both types of polymorph identified between the mixed systems with and without the vacuum gap. If the presence of the vacuum interface alone was influencing polymorph selection we would expect there to be some discrepancy between the results. For the average number of polymorphs a slight difference is seen in the calcite values, however given that the number of clusters used to calculate the result is so small, the distribution values which look at all ions provide much more reliable statistics.

Therefore it is likely another aspect of the initial systems affecting polymorph selection and not exclusively from the vacuum gap.

6.2.2.2 Local Ion Environment

The ion environment around the identified polymorph-like clusters could also influence the chosen structure. With the molecules separated, the local ion environment will vary depending on where the cluster is located. The cluster could be located in a dense region of calcium carbonate with very little water present or near the water region.

For each cluster, the number of nearby atoms/molecules to the central calcium ion are calculated based on RDF results for hydrated ACC, as indicated in Figure 6.9. The cutoff for Ca-Ca distances was 7 Å, 8 Å for Ca-C and 5 Å for Ca-O distances, where O is the oxygen atom of the water molecule. At each timestep, the number of nearby calcium ions, carbonate ions and water molecules was recorded for all Ca^{2+} in the system.

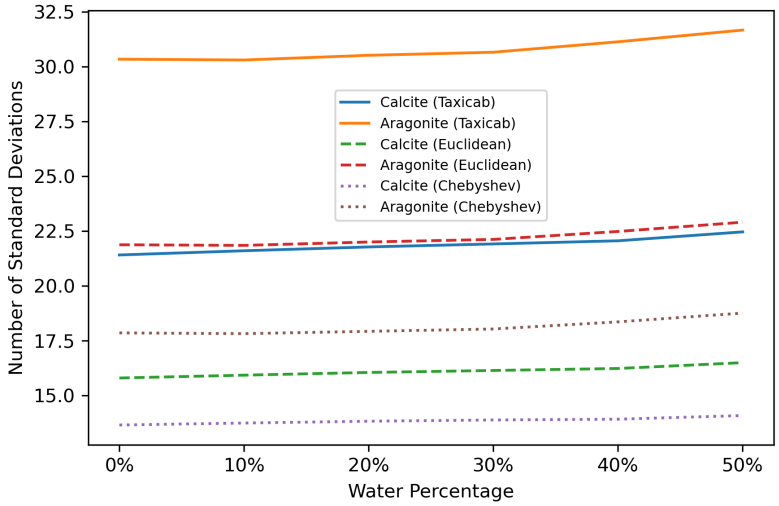

(a)

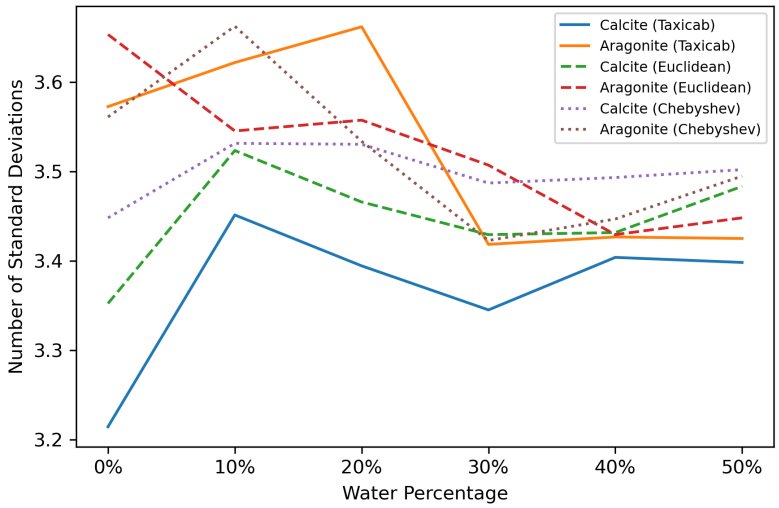

(b)

Figure 6.6: *Median quantified similarity across all mixed systems with no vacuum gaps present.* (b) *shows the median value for the most polymorph-like clusters with standard deviations values below 4.*

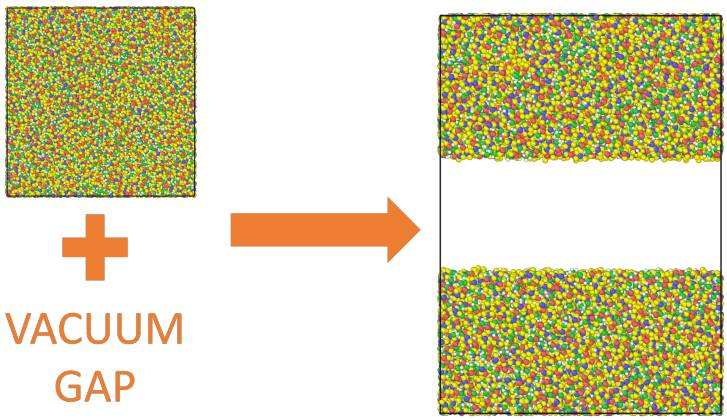

Figure 6.7: *Procedure to create a mixed system with a vacuum gap. Vacuum gap inserted into the 50% water mixed configuration.*

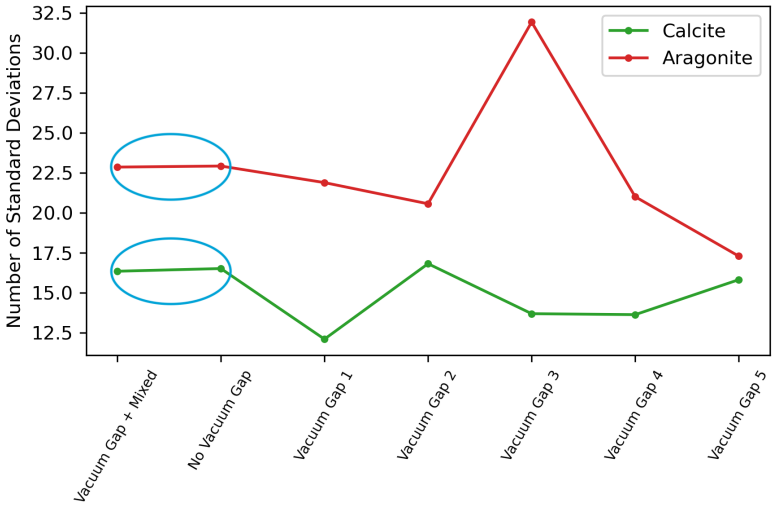

Figure 6.8: *Comparison of 50% configuration across all different system types for calcite and aragonite. Highlighted is the similarity between the mixed vacuum gap system and the mixed system without the vacuum gap.*

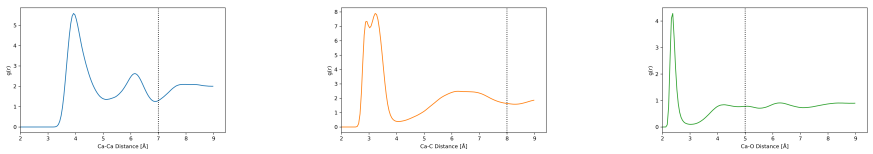

Figure 6.9: *Radial distribution functions for Ca-Ca distances, Ca-C distances and Ca-O distances for the equal ACC and water system. Dotted lines indicated respective cutoff values.*

The correlation between the number of each surrounding atom type and the Manhattan distance similarity of the cluster was computed using Spearman's rank correlation coefficient. A Spearman's rank value of 1 or -1 indicates perfect correlation whereas values close to 0 indicate no correlation between the variables. It can then be distinguished from this if a cluster's similarity to each polymorph is dependent on the ions within its local environment. Example results for the systems with a vacuum gap are presented in Figure 6.10 across each water content value. Although it seems that for aragonite formation and calcite formation in higher water content systems there is some dependence on local ion environment, the correlation values are extremely small. Therefore we can deduce that polymorph similarity is not based on the surrounding ion types and is not deterred or encourage by dense calcium carbonate or water regions.

6.2.3 Water Movement

From our previous simulations, the presence of the vacuum gap and the local ion environment is not influencing polymorph selection in the ACC and water systems. It appears that the movement of the water and calcium carbonate molecules during the separation process is affecting our results. A key part of the nucleation from ACC is the expulsion of water from the nascent crystal [121]. Therefore our suggestion of the water movement influencing polymorph selection is not unreasonable.

To investigate the relationship between polymorph selection and water movement, a configuration consisting of separated calcium carbonate and water molecules ,as shown in Figure 6.11, was created. As the simulation progresses, the molecules are allowed to mix. By splitting the cell into regions across the z-direction, we can see how polymorph selection varies as molecules move. Regions 4 and 5, where the dividing point between calcium carbonate and water lies, will contain the most mixing initially. As periodic boundary conditions are implemented, there will also be mixing across the boundary between regions 0 and 9.

The simulations was initially performed using DLPOLY, however due to increased efficiency, LAMMPS [93] was used to produce the trajectory data for analysis. MD calculations were performed with an NVT ensemble, to aid mixing, and a timestep of 0.5 fs. The system contained 13000 formula units of $CaCO_3$ and 26000 units of H_2O. As the system is dynamic and we expected significant changes in the positions as the molecules mix, analysis has been performed at 1 ns intervals. However, from the central images in Figure 6.12, we see little change in the distribution with time.

In each region, the average number of polymorph-like clusters has been calculated with respect to the total number of ions within that volume. At the lower index regions, there was almost no calcium or carbonate ions present and therefore it was not possible to identify clusters within these regions. As time progresses, Figure 6.12 shows the number $CaCO_3$ units increasing and thus some clusters were identified in regions 0 and 4. However after 4 ns, there was still no clusters, and possibly no calcium carbonate, present in regions 1, 2 and 3.

A greater number of clusters were identified at the higher index regions, unsurprisingly due to the increased amount of calcium carbonate available. For aragonite, the most polymorph-like clusters were identified in region 8 (apart from the large number detected in region 0 after 1 ns which quickly disappears

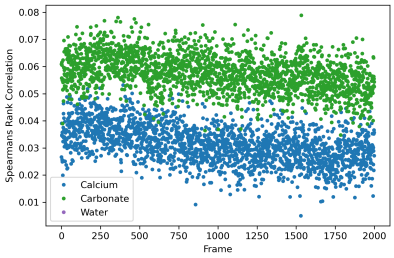

(a) *Calcite 0%*

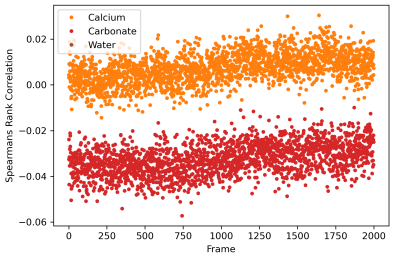

(b) *Aragonite 0%*

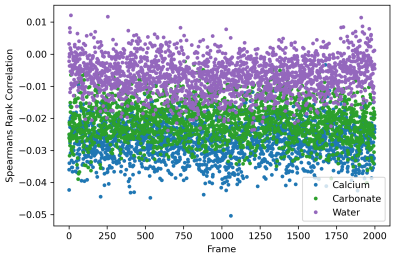

(c) *Calcite 10%*

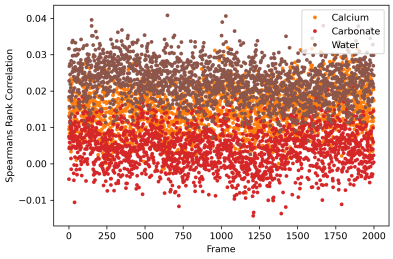

(d) *Aragonite 10%*

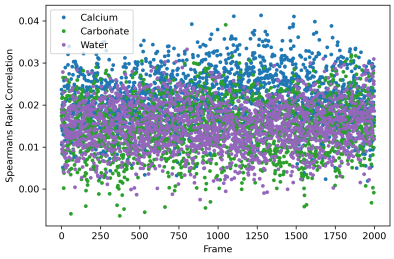

(e) *Calcite 20%*

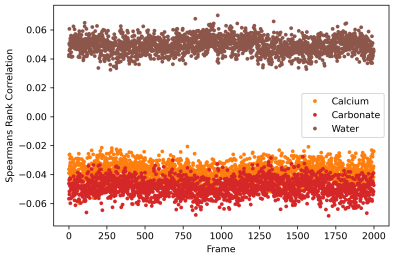

(f) *Aragonite 20%*

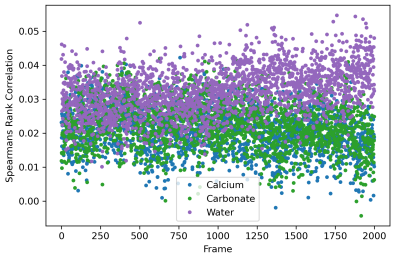

(g) *Calcite 30%*

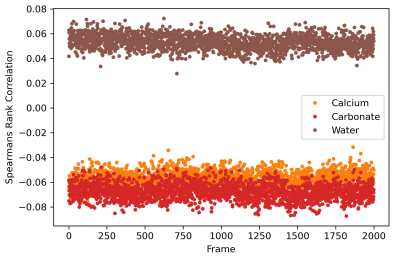

(h) *Aragonite 30%*

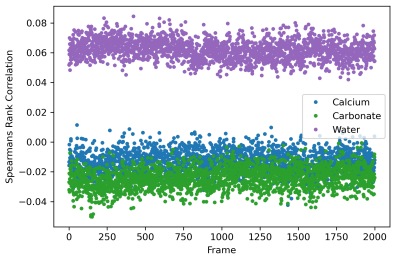

(i) *Calcite 40%*

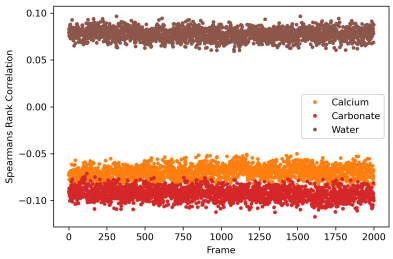

(j) *Aragonite 40%*

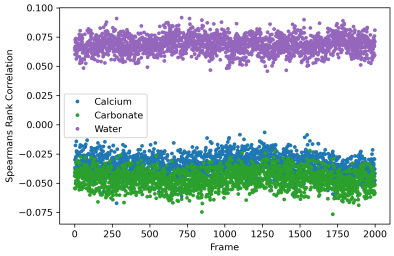

(k) *Calcite 50%*

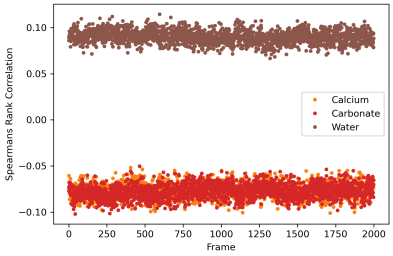

(l) *Aragonite 50%*

Figure 6.10: *Spearman's rank correlation coefficient values between the number of atoms types around the central ion and the similarity to either calcite or aragonite. One starting configuration's values are shown as an example but all configurations show the same results.*

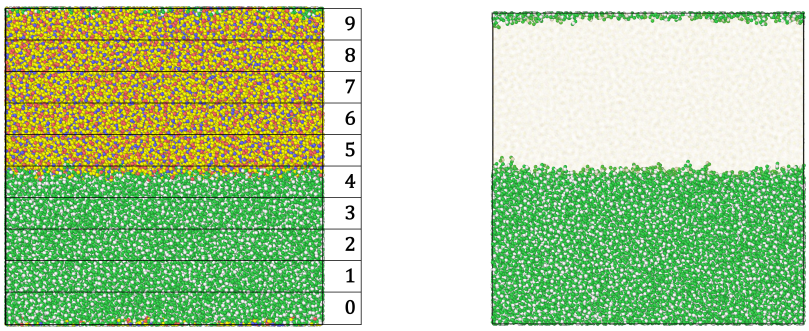

Figure 6.11: *Separated calcium carbonate and water system allowed to mix. The simulation box was split as indicated (left).*

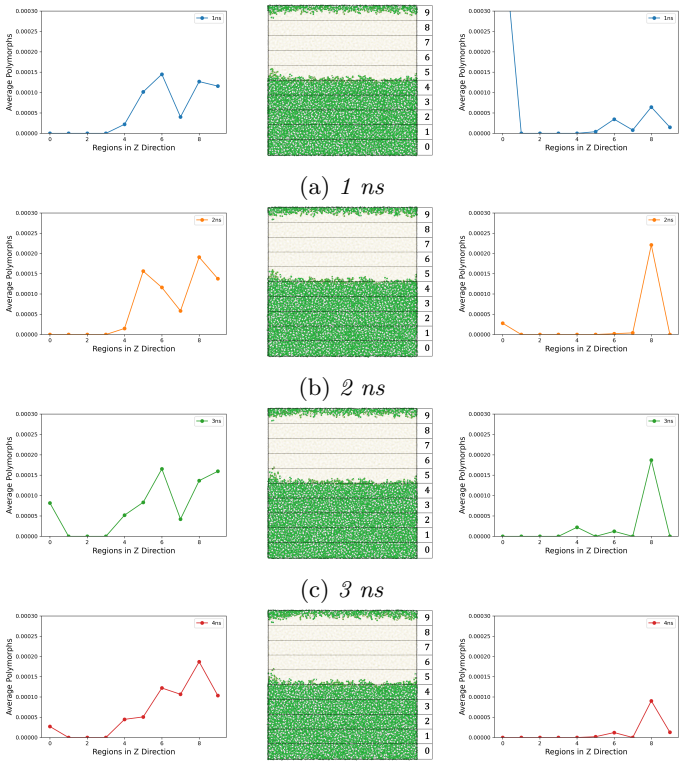

(a) *1 ns*

(b) *2 ns*

(c) *3 ns*

(d) *4 ns*

Figure 6.12: *Number of clusters identified across the different z regions after 1 ns intervals. Calcite- (left) and aragonite-like (right) identified clusters alongside visualisation of the simulation state at the end of the trajectory (centre). The average is calculated relative to the number of* Ca^{2+} *ions in each region.*

and can be considered anomalous) but the value begins to decrease over tine. The greatest number of calcite clusters was identified in regions 6 and 8, those adjacent to the regions of most visible mixing.

More calcite clusters are found over a wider portion of the system, however in region 8, more aragonite than calcite is found up to 3 ns. This is in stark contrast with our previous simulations where calcite was always the most dominant polymorph regardless. Figure 6.13 shows more clearly how the amount of calcite and aragonite varies with time. At 4 ns, the number of clusters across the different regions begins to shift to a smoother curve in the calcium carbonate containing areas. If the simulation was run for longer it is possible this smoothing would continue and a more distinct distribution of the clusters across the system would be found.

In addition to the number of clusters found in each region, we also wish to consider the mobility of the molecules within these regions and determine any possible relationship between them. The mean squared displacement (MSD) has been implemented as a measure of the water molecules' movement within each region of the simulation. Figure 6.14 shows how the MSD of the water molecules within a region varies as the lag-time is increased. A molecule is assigned to a

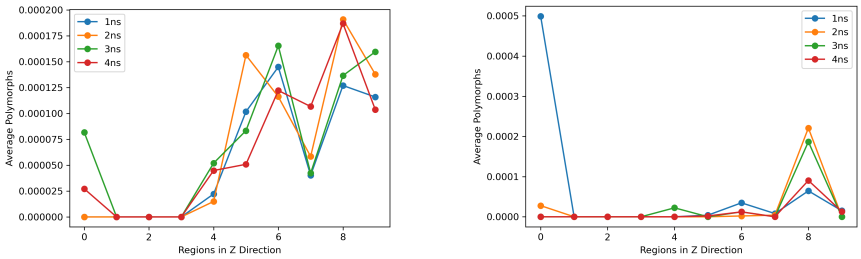

(a) *Calcite* (b) *Aragonite*

Figure 6.13: *Comparison of number identified polymorphs across the MD simulation trajectory at 1 ns intervals.*

region based on its position at $r(t_0 + t)$.

At 1 ns and 2 ns, there is a sharp increase in the MSD for the water molecules in region 9, the area in which waters are likely entering across the periodic boundary. Additionally, a continual decrease is present for the molecules in region 5, which shifts to region 6 at 3 ns. Again, as these are the regions at the interface of the waters and calcium carbonate, it is not unreasonable to see a decrease in the displacement as the water molecules move between regions or begin mixing. No water molecules, thus no MSD values, are present for regions 6 initially and regions 7 and 8 across all trajectories.

During the first ns, there is increased mobility for nearly all other regions containing water; the closer to the interface, the higher the MSD reaches. At later intervals, there is less of an increase and the maximum displacement reached is much lower. However the movement in the regions at the interface (regions 5,6 and 9) is still large, particularly the waters that enter region 6 which have MSD values at least one magnitude higher. Therefore we are seeing less movement in the bulk-like water regions and significantly more at the interface.

An average value for the mean squared displacement has also been calculated so that we have a single value for each region at each timestep. Since we are taking a mean of an already averaged value, the standard deviation associated with the data for each region has also been included as error bars in Figure 6.15.

As already shown in the previous MSD calculations, the highest mobility occurs in the regions closest to the water and calcium carbonate interface: 5, 6 and 9. These are also the regions with the largest spread of values, due to the significant change with lag-time. However the minimum values of these regions are still higher than the maximum in any other region. There is a shift in where the most mobile water molecules are; region 9 after 1 ns, region 5 after 2 ns and region 6 after 3 ns and 4 ns. The shift from 1 ns to 2 ns is due to a reduction in the mobility of the waters in region 9, but the subsequent shift from 2 ns to 3 ns occurs with water molecules entering region 6 and thus mixing with the calcium carbonate.

When comparing the MSD values for each region with the number of polymorphs found there, we can see a relatively large amount of polymorphs are found in regions 5, 6 and 9, where the water mobility is highest. For both calcite and aragonite, the most polymorphs are identified in region 8. Although there is no water present in region 8, there is a significant amount of mobile

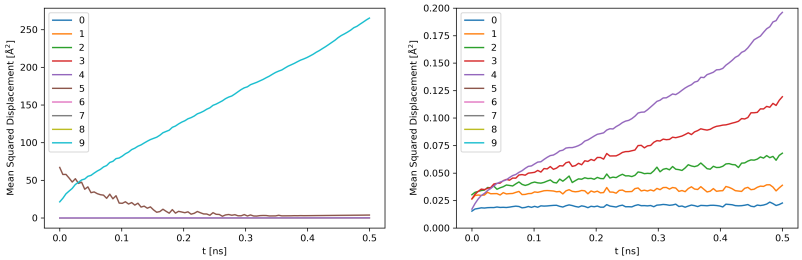

(a) *1 ns*

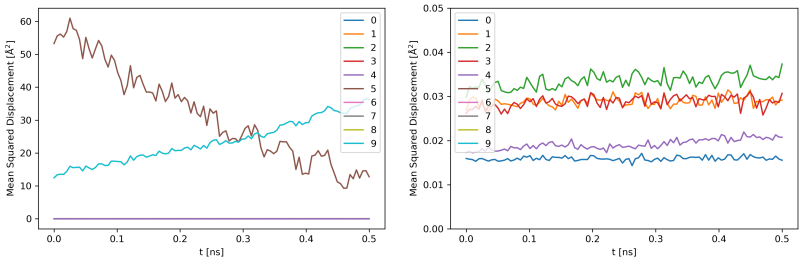

(b) *2 ns*

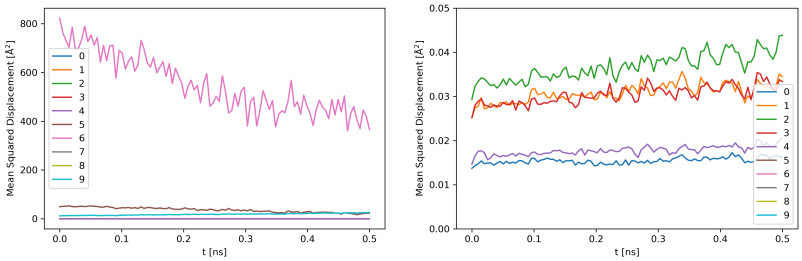

(c) *3 ns*

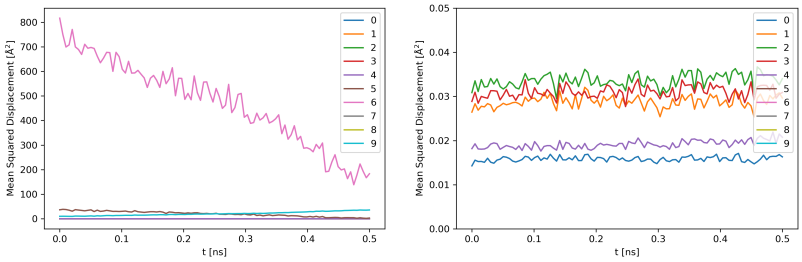

(d) *4 ns*

Figure 6.14: *Mean squared displacement of the water molecules versus the lag-time for each individual region. No water molecules are present in regions 7 and 8 throughout or region 6 for the first 2 ns. A closer look at the other regions are is presented (right) due to scale.*

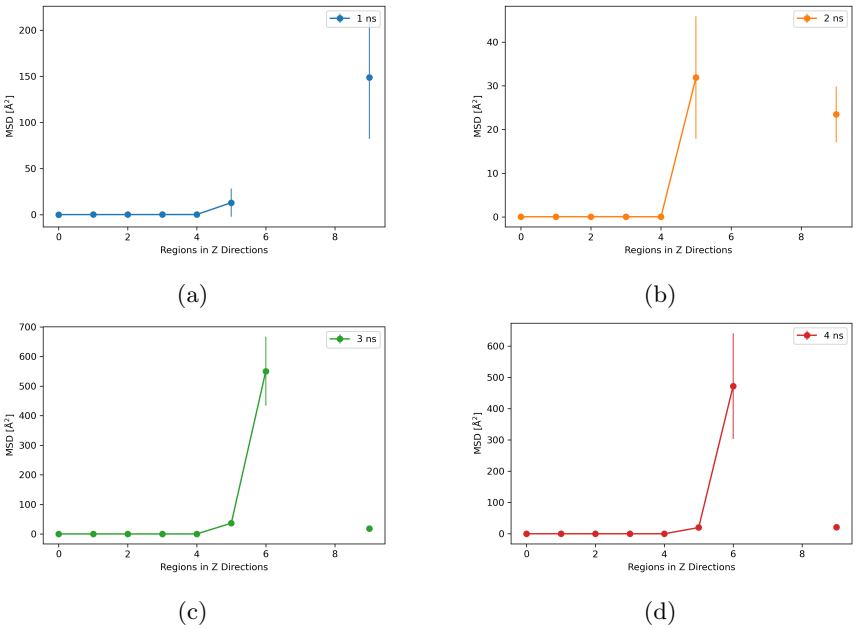

Figure 6.15: *The average MSD for each region across all times intervals. Error bars indicate the standard deviation associated with the values for each region.*

water in region 9. Depending on their location within region 8, the clusters may be close enough to feel the influence of the water movement in the adjacent region. Additionally, no water molecules are found in region 7, where there is a decrease in polymorph-like clusters found compared to the adjacent regions.

Figure 6.16 compares the values of the average number of clusters found and the MSD of the waters in the system. For calcite, the greatest number of polymorph-like clusters are generally found at high values of MSD but there is very little to conclude from the results presented. There is even less correlation found between the aragonite clusters and the water behaviour, however with such low numbers of crystal-like clusters found, the statistics are rather poor.

Although it is not possible to draw a concrete statement on the relationship between polymorph selection and water mobility from our investigation results. There is some suggestion that disruption or changes to the environment around a potential cluster may allow the cluster to order itself into resembling calcite or aragonite. The greatest number of polymorph-like clusters were found within or adjacent to regions where there was large movement of water molecules. Region 7 where there is an abundance of ACC but no water has a lower number of clusters than the adjacent regions where water movement is either found or close enough to feel the influence of water movement from other regions.

Running the simulation for longer or artificially inducing the mixing could provide more answers; firstly increasing the number of clusters formed and secondly allowing a greater change between the starting and finishing configurations if the molecules mix more thoroughly. With more clusters, we can more confidently establish any correlation between where the cluster is found and the dynamics of its surrounding environment. Then with a more thorough mixing,

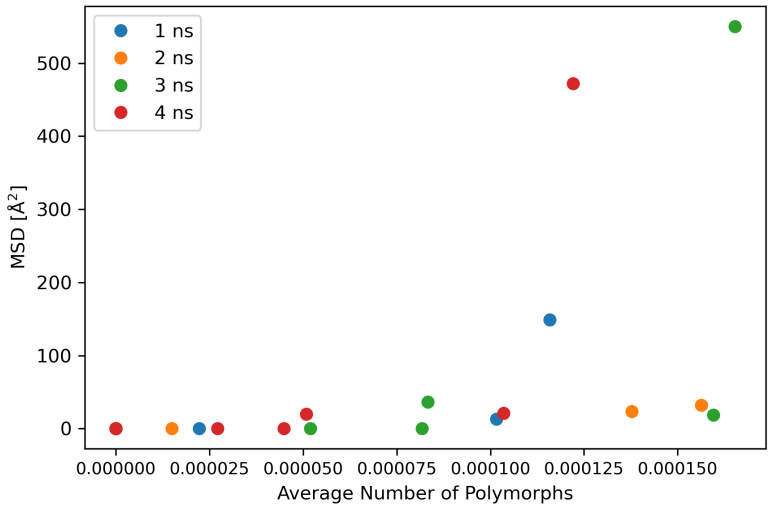

(a) *Calcite*

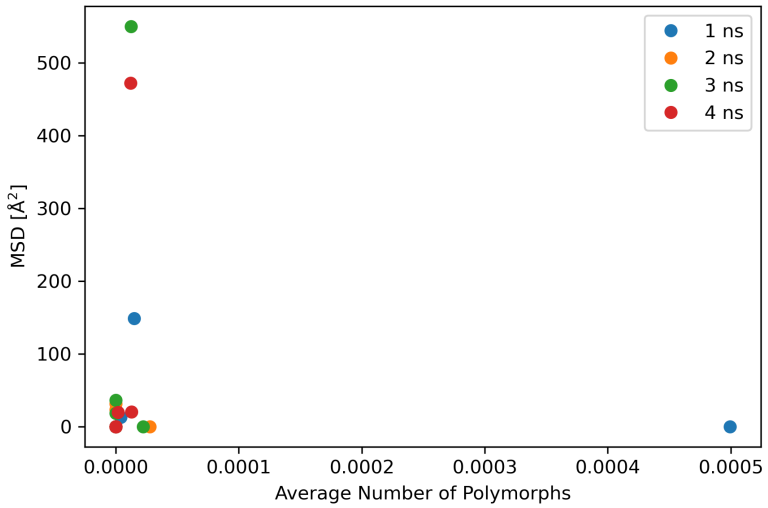

(b) *Aragonite*

Figure 6.16: *Direct comparison of the average number of clusters found within a region and the average mean squared displacement of the water molecules for both calcite and aragonite.*

a greater number of environments are available to test the relationship.

6.3 Conclusions

As with the ion ratio results, very little amounts of either polymorph were found under any conditions. For the ACC and waters systems without a vacuum gap, there was a slight increase in the number of calcite- and aragonite-like clusters found as the amount of water in the system increased but further calculations need to be run for confidence in this conclusion.

A distinct difference in the number of clusters with crystalline-like structure was found between the systems with a vacuum gap and molecule separation and those without. The vacuum gap systems showed a general decrease in the number of polymorph-like clusters identified as water content increased, as opposed to the mixed systems. However the average number of found clusters was generally higher for the vacuum gap systems. The most obvious difference comes from the distribution of similarities. At high water contents, there is a large variation in the average similarity values when the vacuum gap and molecule separation is present. For the thoroughly mixed systems, the similarity shows a constant decrease with water content, suggesting a difference in polymorph selection between the systems with and without a vacuum gap and separation.

From further simulations, it was determined that the vacuum gap was not causing the difference as the average polymorph similarity was the same with and without the vacuum. Additionally it was found that there was no detectable relationship between the location of either polymorph cluster and its local ion environment. The amount of calcium ions, carbonate ions and water molecules around an identified polymorph-like ion varied significantly and had no impact on the polymorph phase found.

By ruling out the other factors, it was thought that the movement of the water and calcium carbonate molecules during the separation process influenced the resultant polymorphs found. Our final simulation allowed the mixing of water and ACC that were initially separated. The number of clusters found was once again very small but did show variation across the regions with differing ion contents. There was also some relationship between the calculated water mobility and the regions in which the polymorph-like clusters were identified; regions with more dynamic ion environments showed more preference for crystal-like cluster formation.

The Manhattan distance method of quantifying similarity allowed us to identify and distinguish ion clusters which resembled calcite and aragonite. However for all systems in which the technique was applied, very few clusters were identified. This is due to the choice of configurations to which we applied the method. All systems were modelling the very early stages of the nucleation of calcite and aragonite from amorphous calcium carbonate and it is possible that the rearrangement to crystalline-like structures occurs much later. This is reinforced by the short lifetimes of the calcite- and aragonite-like clusters found.

To utilise the Manhattan distance method's potential, the technique should be applied to systems further along in the nucleation process or where nucleation has been induced. Fantauzzo has successfully applied the technique to

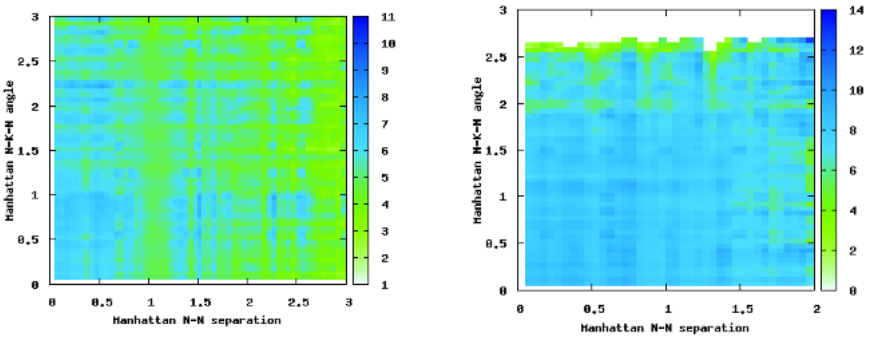

(a) *Calcite*

(b) *Aragonite*

Figure 6.17: *Manhattan distance similarity for distance and angle values for an 8 molal supersaturated solution of potassium nitrate. Images are courtesy of Fantauzzo (currently unpublished).*

identify the different polymorphs of potassium nitrate in supersaturated solutions. As the KNO_3 polymorphs considered resemble the calcite and aragonite structures of calcium carbonate, the reference structures were easily adapted and the method could be applied to the simulation trajectories. These simulations were ran for longer (10 ns) and the ions were confined to induce clustering in the systems for 6, 8, 10 and 12 molal solutions. Results for the 8 molal system are shown in Figure 6.17 as an example. The distribution of distance and angle values for all clusters are shown and a substantially larger number of both polymorphs are identified within the system. Nearly all clusters show close resemblance to the reference structures with $s_{\alpha,\beta}$ values all with 3 standard deviations; aragonite in particular shows very strong resemblance. These results highlight the capability of the Manhattan distance similarity analysis when applied to a system with significantly more crystalline-like structures available to identify.

So far, our investigation into polymorph selection in the calcium carbonate system has focused on kinetic factors (variation in ion ratios, water content and its movement) and identifying polymorphs within the amorphous state. We can also consider thermodynamics and the role that free energy and entropy plays in the selection of calcite and aragonite during the nucleation process.

Chapter 7

Interfacial Free Energies of Calcium Carbonate and Water

The MD simulations looking at the effect of water content and calcium to carbonate ion ratio yielded little evidence that these factors had much effect on polymorph selection, specifically the preference to form aragonite over the more stable calcite. Therefore, our attention turned to the effect of surface stability and its role in polymorph selection.

The final morphology of a crystal is strongly dependent on the interfacial free energy of the solid-liquid interface, in accordance with classical nucleation theory. The phase most likely to nucleate can therefore be predicted using the relative free energies of different forms and their interfaces with solution.

For calcium carbonate, values for the free energies with water have been calculated, however most fail to include the entropic contribution. It has been well established that the water at the calcite-water interface exhibits a structure imposed by the surface[122], therefore the entropic contribution is important to include.

In this work, a novel method utilising Einstein crystals as a thermodynamic reference state has been applied to the calcium carbonate system to calculate the interfacial free energies of hydrated calcite and aragonite surfaces. Unlike previous methods, the associated entropy has been accounted for and has been shown to have a contribution to the interfacial free energies that cannot be ignored.

7.1 Interfacial Free Energy Methods

The interfacial free energy between a solid and liquid phase is the main thermodynamic property of the surface and one of the factors that determines the behaviour of the material during nucleation. It is defined as the reversible work required to form a unit area of the solid/liquid interface. Both the nucleation rate and the final crystal morphology are strongly dependent on this value.

Free energies are difficult to measure experimentally and also challenging

to calculate from simulations. Frequently the surface energy or enthalpy is computed instead and used in determining crystal stability and morphology. At a solid/liquid interface, the solid may impose ordering in the liquid and in such cases, the entropy of the system cannot be ignored. Interfacial free energy values contain both the enthalpic and entropic contributions, providing significantly more information on the system. Despite the difficulty, methods are available to calculate interfacial free energies from atomistic simulations.

Contact Angle Approach

One of the most straightforward solutions to calculating the interfacial free energy involves direct simulation of a liquid droplet on a solid surface [123]. From the geometry of the liquid droplet, the contact angle θ_c with the surface can be computed, which is related to the solid/liquid interfacial energy γ_{SL} via Young's equation,

$$\gamma_{SG} = \gamma_{SL} + \gamma_{LG} \cos \theta_c,$$

along with the solid/vapour and liquid/vapour interfacial energies.

Despite its simplicity, the method has a number of drawbacks. Finite size effects strongly influence the value of θ_c and large simulation cells are therefore required to mitigate these errors. The liquid droplet may require a long time to equilibrate, further increasing computer expense, and the contact angle depends on the choice of contact plane with the droplet, imparting ambiguity into the result. A large vapour pressure is also associated with the finite size of the system. Altering the system so that a curved solid phase is in contact with a liquid film eliminates issues with vapour pressure [124] but it is still plagued by other problems and the difficulty associated with creating a curved solid.

Metadynamics

Metadynamics can be employed to calculate free energies [125]. The free energy surface is constructed during the simulation. The surface maps out a transition from a single phase to where two phase coexist. Excess free energy is given by the minimum difference in Gibbs free energy between the two regions at the solid-liquid equilibrium temperature. The solid/liquid interfacial energy γ_{SL} is equivalent to the excess free energy divided by the surface area of the interface.

Unlike other free energy calculation methods, the metadynamics approach is less affected by hysteresis. However, complex order parameters are required to differentiate between the solid and liquid phases, which can be both resource heavy and bias the results.

Mold Integration

A more recently proposed method relies on introducing a mold to the system to induce the formation of a crystal slab in the liquid phase [126]. The mold is composed of potential energy wells, the positions of which are defined by the lattice sites of the selected crystal plane. The interaction between the wells and the liquid particles reversibly induces the formation of a thin crystal slab, resulting in two solid/liquid interfaces either side of the mold [127].

As the formation of the crystal slab is performed under coexistence conditions, the solid and liquid have the same chemical potential and thus the work

associated with the slab formation is related to the interfacial free energy and twice the area of the interface. The work required for creating the crystal slab in the system can be calculated via thermodynamic integration (see Section 4.2) from the initial state, where potential energy wells are turned off, to the final state, where the wells are fully on. A gradual change in the interaction between the wells and the particles is required for a suitable thermodynamic integration pathway.

Unfortunately the method described can only be performed on systems near the solid/liquid coexistence point and at a flat interface. Application to a heterogeneous system may also prove considerably more complicated than the approach described here.

Cleaving Wall Methods

Arguably the most established approaches are the cleaving wall methods [128]. Both the bulk solid and bulk liquid are cleaved using a "cleaving potential" at coexistence conditions. The cleaving potential should promote the formation of properly oriented layers upon insertion into the liquid phase. The boundary conditions are altered such that the solid and liquid are combined whilst still maintaining the potential. Gradually the potential is removed from the combined system [129,130].

The reversible work performed in cleaving the two phases, combining the solid and liquid parts, and removing the potential, when integrated equates to the excess surface free energy. To convert to interfacial free energy, the excess free energy is divided by the interface area, as with the metadynamics approach. Thermodynamic integration is used on each of the four steps in the process and summed to obtain the total interfacial free energy of the system.

For simple systems, this method is successful, but the assumptions upon which it is based hinder its use in more complicated cases. It assumes that the top and bottom surfaces of the slab will recreate the bulk when they meet, which is not always the case. A well defined and flat interface is also required for successful cleaving of the solid and liquid phases. Finally, any dipolar surfaces cannot be accounted for easily in a fully periodic system like the one required for the cleaving wall method.

A new method [4] is employed in this work, which can be applied to more complex systems due to the flexibility of the approach. The framework accommodates dipolar surfaces and miscible molecules at the interface as well as significantly optimising the method to avoid needless recalculation of values, further details are discussed in Section 7.3.

7.2 Previous Work

Atomistic simulations have been frequently utilised to calculate interfacial free energy values of calcium carbonate. Static simulations have been used to calculate the hydrated surface energies of various calcite and aragonite surfaces by De Leeuw and Parker [131]. The calcite $\{10\bar{1}4\}$ surface was undoubtedly the most stable of all surfaces considered and the hydrated morphology, determined with Wulff construction, exhibited a strong resemblance to the experimental

morphology. For aragonite, more surfaces were considered and a greater range of energies were found. The resultant morphology showed some resemblance to the suggested mineral morphology but a poorer match than for the calcite resemblance. The equilibrium and hydrated morphologies of calcite are almost entirely dominated by a single surface, the same is not true for aragonite and more surfaces are expressed. Importantly, the reported surfaces energies contain only the enthalpic contribution and entropy is ignored.

More recent work by Bano et al has built upon the previous study and implemented updated forcefields and simulation methods to reconsider the calcite and aragonite interfaces with water. The calculated enthalpy values for hydrated calcite and aragonite surfaces are nearly all negative and small in magnitude[132]. This alone would suggest that the bulk crystal is unstable in aqueous environments. The authors highlight that the structured water layers found at the crystal-water interface indicate an entropic contribution should be included. For stable crystallites, all surface energies must be positive, therefore the authors suggest that the entropy contribution is both positive and of greater magnitude than the enthalpy term. By considering the structure of the water layers at the interface as ice-like, the entropy is approximated by the entropy of fusion in the ice-liquid water system, which produces a value able to compensate for the negative enthalpies.

Both works discussed here suggest that the entropy of the system is an important term that cannot be ignored when considering the interfacial free energies of calcium carbonate with water. In this work, the method used to calculate the interfacial free energies of calcite and aragonite surfaces with water includes both the enthalpic and entropic contributions and quantifies their relative contributions.

7.3 Free Energies using Einstein Crystals

Free energies cannot be measured directly, instead the difference in free energy between states is calculated. For comparison, a common reference state is required. The method for calculating free energies adopted here has been recently developed by Yeandel[4] and uses Einstein crystals as the chosen reference state. This method can be applied to much more complex system than the previous methods detailed above and makes extensive reuse of previously calculated values to improve efficiency. In the paper, the method is applied to the hydrated calcium sulphate system and it is able to handle the miscible species present in the different phases. Since we are only looking at anhydrous phases of calcium carbonate, the miscible species correction is not required and the method is simplified further.

Transformation from a system to an Einstein crystal is relatively straightforward for the solid phase. Within the Einstein crystal, each atom is confined to its own harmonic well with a fixed spring constant, which is the same for all atoms. The atoms do not interact with each other. As the energy of the Einstein crystal does not depend on the position of the constituent atoms, for the same temperature and composition, atoms can be rearranged without a change in free energy. The free energy difference between states A and B can therefore be calculated in two stages; the conversion of state A to the Einstein crystal and the conversion of the same Einstein crystal to state B. As the transformation

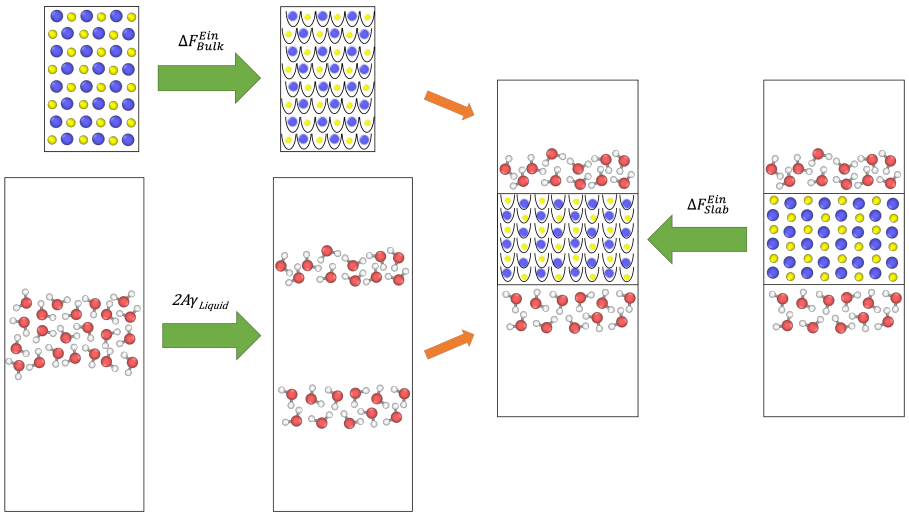

Figure 7.1: *Schematic diagram to show general procedure and setup for interfacial free energy calculations via Einstein crystals. The two calculations on the left need only be computed once for each bulk phase and liquid and reused; the righthand calculation is different for each surface considered.*

is reversible, the free energy difference between the states is given by

$$\Delta F^{B}_{A} = \Delta F^{Ein}_{A} - \Delta F^{Ein}_{B} \tag{7.1}$$

where $\Delta F^{Ein}_{A,B}$ is the free energy difference between the states A or B and the Einstein crystal of the same composition. Thermodynamic integration (TI) is then used to transform between the state of interest to the Einstein crystal.

For use in calculating solid/liquid interfacial free energies, the atomistic simulation is set up such that the solid slab lies between two liquid layers with vacuum gaps either side, as demonstrated in Figure 7.1. The free energy of the interface $\gamma_{Interface}$ is then given by

$$\gamma_{Interface} = \frac{\Delta F^{Liquid+Vacuum}_{Liquid} + \Delta F^{Slab}_{Bulk}}{2A} \tag{7.2}$$

where A is the area of the interface and the factor of 2 arises from solid/liquid interfaces appearing on both sides of the slab. The term $\Delta F^{Liquid+Vacuum}_{Liquid}$ arises from inserting a vacuum gap in the liquid layer large enough to accommodate the solid slab. This value, divided by the area of the two arising interfaces is equivalent to the surface tension of the liquid γ_{Liquid}. The second free energy difference, ΔF^{Slab}_{Bulk} results from inserting the bulk solid into the vacuum gap between two liquid layers to create the slab. It is this transformation that utilises the Einstein crystal reference state,

$$\Delta F^{Slab}_{Bulk} = \Delta F^{Ein}_{Bulk} - \Delta F^{Ein}_{Slab} \tag{7.3}$$

as dictated by Equation 7.1. By substituting the surface tension and Equation 7.3 into Equation 7.2, the following equation

$$\gamma_{Interface} = \gamma_{Liquid} + \frac{\Delta F^{Ein}_{Bulk} - \Delta F^{Ein}_{Slab}}{2A} \tag{7.4}$$

can be used to calculate the solid/liquid interface. Both γ_{Liquid} and ΔF_{Bulk}^{Ein} can be calculated once and reused for various slabs in the system, the bulk to Einstein crystal conversion value must be scaled accordingly to the number of formula units. The surface tension of liquids can be calculated from simulations using the Kirkwood-Buff method which relates the pressure tensor of the liquid system to the surface tension [133].

Converting from either the bulk or the slab to the Einstein crystal requires two thermodynamic integration pathways with control parameters λ. Firstly, the harmonic wells for each atom are activated with TI ($\lambda_{Harm}0 \rightarrow 1$). Second, the atomic interactions, excluding the now activated harmonic wells, are switched off with TI ($\lambda_{Pot}1 \rightarrow 0$). It is important to note that when converting the slab to an Einstein crystal, the solid-solid and solid-liquid interactions are turned off however the liquid-liquid interactions are left on.

Thermodynamic integration is discussed more generally in Section 4.2 but for the pathways described above, there are some possible convergence issues when approaching the end points of 0 and 1. To combat this, a function of λ may instead be used. The author's chosen function,

$$f(\lambda) = \lambda^5(70\lambda^4 - 315\lambda^3 + 540\lambda^2 - 420\lambda + 126) \tag{7.5}$$

is a sigmoid function that smoothly approaches 0 and 1 allowing improved convergence of the thermodynamic integral. The derivative of the Hamiltonian with respect to the function of the control parameter $f(\lambda)$ is calculated numerically using the symmetric difference quotient. Because $f(\lambda)$ is non-linear, the step size, δ, used in the differentiation is also defined as a function of λ such that

$$\delta(\lambda) = 0.01f(\lambda). \tag{7.6}$$

The perturbed Hamiltonians $H(f(\lambda) + \delta(\lambda))$ and $H(f(\lambda) - \delta(\lambda))$ are calculated based on the results of trajectory used for $H(f(\lambda))$ so that further simulations are not required. The average potential energy then can be calculated with the results for $f(\lambda) \pm \delta(\lambda)$, provided the perturbations of $f(\lambda)$ are sufficiently small.

In contrast, the calculation of the enthalpy $\Delta H_{Interface}$ of the interface is much simpler. The enthalpy of the components of the system; the bulk, slab, liquid and liquid/vacuum interface are directly calculated and combined by

$$\Delta H_{Interface} = \frac{\Delta H_{Slab} - \Delta H_{Bulk} - \Delta H_{Liquid} - \Delta H_{Liquid/Vacuum}}{2A} \tag{7.7}$$

to determine the interfacial enthalpy. With both the interfacial free energy and interfacial enthalpy known, the entropy, ΔS of the system can be simply calculated with $\Delta F = \Delta H - T\Delta S$.

The method described has been applied in this work to the calcium carbonate system investigating various calcite and aragonite surfaces in contact with pure water.

7.4 Results

For calcite, it is well known that the $\{10\bar{1}4\}$ surfaces entirely dominates the resultant crystal structure [134,135,136], hence for calcite only the $\{10\bar{1}4\}$ and $\{01\bar{1}2\}$ surfaces have been considered. The $\{01\bar{1}2\}$ is one of the more stables surfaces of

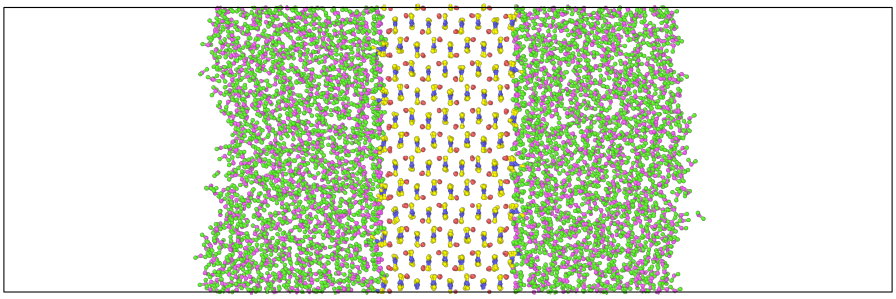

Figure 7.2: *Initial simulation setup for an example system. The water has been introduced to the system during an MD run. The vacuum gap on either side is large enough to ensure no interactions occur across the boundary.*

calcite, however it is still not expressed in the crystal morphology. It provides a comparison for the $\{10\bar{1}4\}$ surface to ensure it is the most stable surface, as expected. Several low index surfaces of aragonite have been investigated consistent with previous literature and the numerous faces expressed in the crystal morphologies.

7.4.1 Simulation Setup

Each surface follows the procedure outlined in Section 7.3. All simulations have been performed using the Large-scale Atomic/Molecular Massively Parallel Simulator (LAMMPS) program [93] and run on HPC Midlands+ Sulis machine. Previously used forcefields of Raiteri [118] for $CaCO_3$ and the SPC/Fw model of water [120] have again been implemented.

The initial configuration includes the respective calcite or aragonite slab in contact with the vacuum in an elongated simulation cell as depicted in Figure 7.2. Water is then inserted during a MD run to create the liquid/solid/liquid setup required for the calculation of interfacial free energies. The number of water molecules inserted was selected to create a roughly equal water layer thickness ($\sim$ 30 Å) across all surfaces. Both the solid slab and the water layers are wide enough to ensure that interactions are not occurring across the slab and the "bulk" water behaviour is present as well as the surface effects.

The simulation cell is then equilibrated by an NPT run with the lattice vector perpendicular to the slab orientation held constant. All simulations were performed at 300 K and 0 bar using the Nosé-Hoover thermostat and barostat with relaxation times of 0.1 ps and 1.0 ps respectively and a 1 fs timestep. Additionally the long-ranged electrostatic interactions were determined using a PPPM algorithm with a relative force accuracy of 1.0×10^{-5}. The cell is equilibrated for 100 ps and the average lattice vectors calculated over the remaining 500 ps run. A short NVT run is then performed to ensure the stability of the cell before the thermodynamic integration is performed.

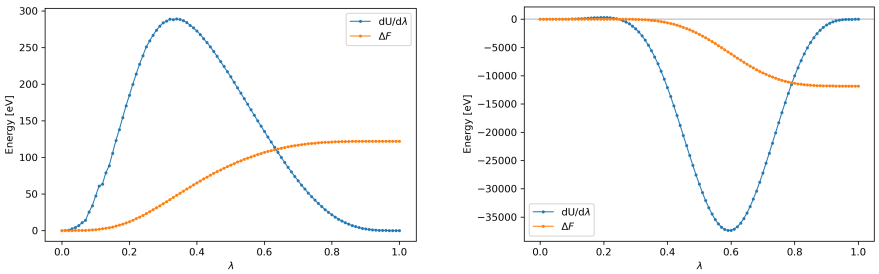

(a) (b)

Figure 7.3: *Example curves produced by the TI scheme for the energy differential* $dU/d\lambda$ *and the free energy calculated via numerical integration* ΔF*.* (a) *shows data associated with turning the harmonic wells of the Einstein crystal on and* (b) *shows the effects of turning the interatomic potentials on going from* $\lambda = 0$ *to* $\lambda = 1$*.*

Two TI calculations are required to convert the solid to an Einstein crystal; one to activate the harmonic wells in the solid and the other to turn off interactions for the solid atoms. For the first TI calculation, λ varies between 0 and 1 as the harmonic wells are gradually switched on while the other atom interactions are still present. For the second calculation, the harmonic wells are fully on and the other potentials are incrementally switched off as λ varies from 1 to 0. Each calculation consists of 100 discrete values of λ to ensure a smooth integration curve (see Figure 7.3) and the MD simulations were performed simultaneously each for 0.5 ns using a Langevin thermostat at the same relaxation time and the potential energy sample every 1 ps. The method's author suggests a change of thermostat as the Nosé-Hoover does not provide full ergodic sampling at the end of the TI pathway when the system is almost purely comprised of harmonic oscillators [137].

A similar procedure is followed for the bulk phases of calcite and aragonite but without the inclusion of water or the vacuum and all lattice vectors are unconstrained in the equilibration run. The separate TI pathways are numerically integrated and the difference between the energies equates to the free energy associated with the conversion of the slab or bulk into an Einstein crystal, $\Delta F^{Ein}_{Slab,Bulk}$ required for computing the interfacial free energy.

The results obtained for ΔF^{Ein}_{Bulk} for calcite and aragonite can be reused for each interfacial free energy calculation of the respective surfaces with Equation 7.4. Additionally the value of γ_{Water} may be reused for all calculations at 300 K. The surface tension of water has been taken from the original paper [4] as 0.0581 J/m^2 since the same water model is being used.

7.4.2 Interfacial Free Energies of $CaCO_3$ and Water

The low index surfaces {001}, {010}, {011}, {100} and {110} of aragonite have been considered. For the {110} surface, both the calcium terminated, {110}Ca, and carbonate terminated, {110}CO_3, configurations have been studied. For calcite, only the two surfaces, $\{10\bar{1}4\}$ and $\{01\bar{1}2\}$, were included.

Results for the interfacial free energies, comprising both enthalpy and en-

(a) *Calcite*

Surface	**Interfacial Free Energy** [J/m^2]
$\{10\bar{1}4\}$	0.205
$\{01\bar{1}2\}$	0.487

(b) *Aragonite*

Surface	**Interfacial Free Energy** [J/m^2]
{001}	0.307
{010}	0.240
{011}	0.295
{100}	0.387
{110}Ca	0.291
{110}CO_3	0.440

Table 7.1: *Interfacial free energy values for aragonite and calcite surfaces with water.*

tropy, of the selected calcite and aragonite surfaces are given in Table 7.1. As with previous studies and experimental findings, the calcite $\{10\bar{1}4\}$ surface is unequivocally the lowest at 0.21 J/m^2 and thus the most stable surface. The $\{01\bar{1}2\}$ surface has the highest energy of all slabs considered. For the $\{01\bar{1}2\}$ surface, the dipole across the slab has been removed in the cutting process by translating calcium ions from the top surface to the bottom. A second configuration with the dipole has been calculated, however the resultant energy was so much larger, 1.10 J/m^2, that it has not been considered in further analysis.

Bruno et al. reported a value of 0.49 J/m^2 for the interfacial free energy of the $\{10\bar{1}4\}$ surface with water using static simulations[138]. More recently values of 0.16 J/m^2 and 0.18 J/m^2 have been calculated by Bano et al.[132], in strong agreement with our results. Importantly, the works reported and our own work have all utilised different calcium carbonate forcefields, inevitably leading to discrepancies in values.

For aragonite, there is much less distinction between surfaces. Although {010} is the lowest, it is still less stable than the calcite $\{10\bar{1}4\}$ surface and suggests that calcite is more likely to form than aragonite in water - in line with current understanding of calcium carbonate nucleation. The {001}, {011} and {110}Ca surfaces all lie within 0.016 J/m^2 of each other and any slight variation in the free energy values could alter their relative stabilities. The carbonate terminated {110}CO_3 has a much higher value than its calcium terminated counterpart and therefore the {110}Ca surface is likely to be favoured in the resultant crystal. After the carbonate terminated surface, the least stable surface of aragonite is the {100} surface. Despite the higher number of surfaces considered, the range of values for aragonite is lower than that between the two calcite surfaces. The close proximity of the aragonite surface stabilities is reflected in the variety of aragonite morphologies and expressed surfaces observed when precipitated experimentally. Although work looking at the interfacial energies of the numerous aragonite surfaces is available[131,139,140], there is very little on the interfacial *free* energies. The most stable calculated surfaces, {010} and {110}, however are the faces more often expressed in naturally formed aragonite[134,135].

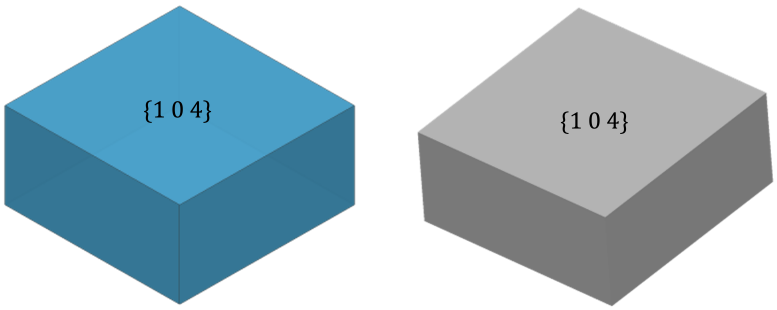

(a) *Calcite*

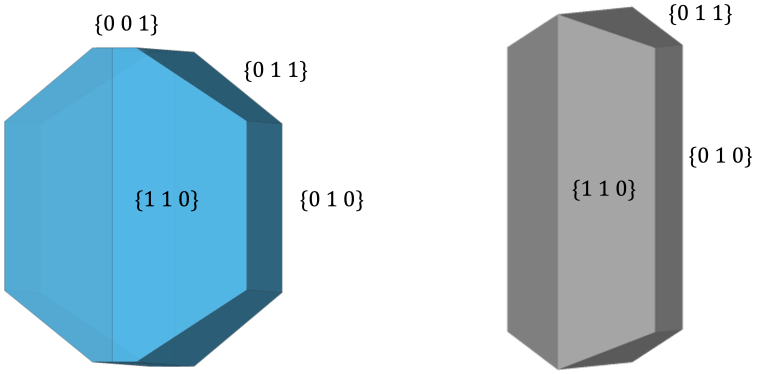

(b) *Aragonite*

Figure 7.4: *Crystal morphologies (left) of calcite* (a) *and aragonite* (b) *in pure water at 300K calculated with the Wulff construction method compared with the respective measured equilibrium morphologies (right)*[134,135].

7.4.3 Crystal Morphology

Using the interfacial free energies in Table 7.1, the Wulff construction can be utilised to determine the equilibrium morphology of calcite and aragonite nanoparticles in pure water. The shape of the nanoparticle is determined by minimising the overall free energy. Our hydrated morphologies for calcite and aragonite are shown in Figure 7.4 alongside the known equilibrium structures[134,135].

The rhombehedral morphology of calcite (Figure 7.4a, left) is in agreement with previous morphology predictions and experimental morphologies. Only the $\{10\bar{1}4\}$ surfaces are expressed[131,136]. The aragonite morphology (Figure 7.4b, left) shows a strong resemblance to the equilibrium morphology, particularly in comparison to previous morphology predictions[131,139]. Despite not appearing in the equilibrium morphology, the {001} has been observed experimentally[141] and is therefore not inconceivable as part of the structure. Generally, scanning electron microscopy images show hexagonal rods or needles of aragonite[136?,142] but there are many factors that could alter our predicted morphologies to those seen; kinetic effects are ignored here as well as the presence of impurities. For

further confidence in the results produced, other calcite and aragonite surfaces should be calculated to determine whether they are stable enough to influence the equilibrium morphology.

7.4.3.1 Relative Nanoparticle Stabilities

From the interfacial free energies and Wulff construction process, quantities are obtained to describe the resultant nanoparticle morphology. Firstly, the shape factor, f_{Nano}, quantifies how much the crystal shape deviates from a sphere of the same volume. If the crystal was perfectly spherical, $f_{Nano} = 1$, all other shapes will have a value higher than this. The average interfacial energy of the crystal γ_{Nano} can also be obtained with a weighted average of the interfacial energies of the expressed surfaces and their corresponding area.

With these quantities and the volume per formula unit of the bulk phases V_{Bulk}, the author [4] calculates the free energy required to convert a nanoparticle of one phase to the other in pure water. The procedure will be repeated here for the conversion of a calcite nanoparticle to an aragonite nanoparticle, as a function of the number of formula units, n.

For conversion of the bulk phase to a nanoparticle of the same phase, the following formula is used

$$\Delta F_{Bulk}^{Nano}(n) = \gamma_{Nano}\, f_{Nano}\, C(nV_{Bulk})^{2/3} \tag{7.8}$$

where $C = 6^{2/3}\pi^{1/3}$, the constant terms in the surface area of a sphere. Additionally, the difference in free energies of the bulk calcite and aragonite phases is required and is given by,

$$\Delta F_{Cal}^{Ara} = \Delta F_{Cal}^{Ein} - \Delta F_{Ara}^{Ein} \tag{7.9}$$

which uses the conversions of bulk calcite and aragonite into Einstein crystals computed during the interfacial energy calculations. The final function for the conversion of calcite to aragonite nanoparticles is then

$$\Delta F_{Nano(Cal)}^{Nano(Ara)}(n) = -\Delta F_{Cal}^{Nano(Cal)}(n) + n\Delta F_{Cal}^{Ara} + \Delta F_{Ara}^{Nano(Ara)}. \tag{7.10}$$

The free energy associated with the conversion of aragonite to calcite, ΔF_{Ara}^{Cal} is measured as -840 ± 20 J/mol [143], a value that is reproduced by Raiteri et al. using a slightly older version of the calcium carbonate forcefield than that implemented in this work [144]. Our value for the energy difference comes out as -612 J/mol, the same sign and magnitude as the reported value.

Values of $f_{Nano} = 1.28$ and $f_{Nano} = 1.14$ were obtained for the shape factors of calcite and aragonite respectively. As only the $\{10\bar{1}4\}$ face is expressed in the calcite morphology, the average interfacial energy is simply the interfacial energy of the surface, $\gamma_{Nano} = 0.20$ J/m^2, whereas for aragonite, the weighted average value is $\gamma_{Nano} = 0.28$ J/m^2. Using these, the relative nanoparticle free energy as a function of the number of formula units is shown in Figure 7.5. As the value is always positive, calcite is always the favoured polymorph regardless of the number of formula units, in line with experimental findings. A negative value would suggest that an aragonite nanoparticle is more favourable to form.

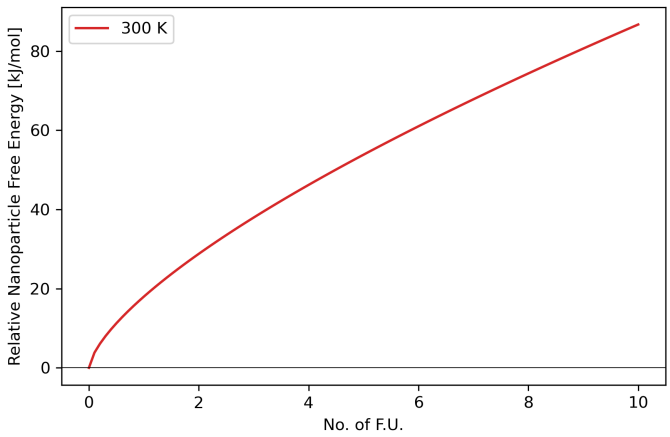

Figure 7.5: *Relative nanoparticle free energy of calcite and aragonite as a fucntion of number of formula units. As the calculated values are always positive, calcite is always the favoured polymorph regardless of size.*

7.4.4 Enthalpy and Entropy

In addition to the interfacial free energy, the interfacial energy, or *enthalpy*, of each slab has been calculated with Equation 7.7. The enthalpy of the slab, ΔH_{Slab}, and the respective bulk, ΔH_{Bulk}, were obtained from MD runs under the same conditions as the TI calculations but with the harmonic wells turned off and the interatomic potentials on. Values for the bulk water enthalpy, ΔH_{Water}, and water/vacuum surface enthalpy, $\Delta H_{Water/Vacuum}$ have been taken as -42.2 kJ/mol per formula unit and 0.115 J/m^2 respectively, as used by Yeandel[4].

The entropic contribution to the interfacial energy , $-T\Delta S$, can be obtained by subtracting the enthalpic contribution from the free energy, the values of which are shown in Table 7.2 and also displayed in Figure 7.6 for further clarity.

One of the first things to note is that the entropic contribution is not uniform across all the surfaces, suggesting that a single entropic correction is not enough when considering stability, particularly in the case of calcium carbonate where there is very little separating the thermodynamic stability of the two phases. Secondly, the fraction of entropic contributions to the free energies of the aragonite surfaces are much greater than those of calcite. For the $\{10\bar{1}4\}$ and $\{01\bar{1}2\}$ surfaces of calcite, 35% and 33% of the interfacial free energy is due to the entropy, which is lower than all the aragonite surfaces. The contributions for the aragonite surfaces vary from 39% to 65%, with the {010} and the {100} surfaces having only minor enthalpic contributions.

Focusing on the {010} aragonite surface, the enthalpy associated with the interface is lower than that of the $\{10\bar{1}4\}$ calcite surface, however the large entropy results in a less stable surface. If the entropy in this system were reduced, say by impurities distrupting the water structuring, the aragonite surface would become the more stable, presenting a possible means of promoting aragonite over calcite nucleation.

In the original work (applied to calcium sulphate) the metastable bassanite phase was found to have generally larger entropic contributions than the more

Surface	Free Energy ΔF	Enthalpy ΔH	Entropy $-T\Delta S$
$\{10\bar{1}4\}$	0.205	0.133	0.071
$\{01\bar{1}2\}$	0.487	0.325	0.162
$\{001\}$	0.307	0.189	0.118
$\{010\}$	0.240	0.084	0.156
$\{011\}$	0.295	0.166	0.129
$\{100\}$	0.387	0.171	0.216
$\{110\}$Ca	0.291	0.152	0.139
$\{110\}CO_3$	0.440	0.255	0.185

Table 7.2: *Interfacial free energy, and the individual enthalpy and entropy components contributing in $[J/m^2]$. ΔF and ΔH are obtained from MD simulations and $-T\Delta S$ from the difference between them. Note that although the entropic contribution is positive, the change in entropy ΔS will be negative.*

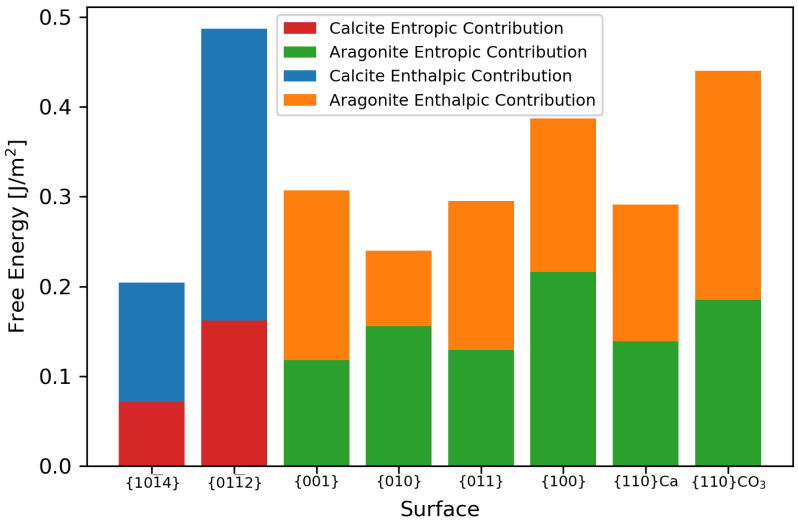

Figure 7.6: *Interfacial free energies ΔF of all surfaces at 300 K. The entropy contribution $-T\Delta S$ is also displayed for each surface and the remaining proportion of the free energy is the enthalpic contribution ΔH.*

thermodynamically stable gypsum phase. This bears a strong similarity to our results with the less stable phase, aragonite, having a greater dependence on entropy than the stable calcite phase. However significantly more systems would need to be investigated before we could generally conclude that metastable phases have a greater entropy contribution to the interfacial energy.

The small change in enthalpy is due to the strong binding of the water with the Ca^{2+} ions at the surface. This accumulation of molecules at the surface imposes water ordering at the interface; which results in an entropy penalty when compared to the disorder of bulk water. Therefore for more information of the role entropy contributes to the interfacial free energies, analysis of the water at the surface is required.

7.4.5 Water Ordering

Ordering of water at the calcite interface has been reported both experimentally and computationally [122,144,145] and structured layers of water molecules are observed at the surface. For aragonite, less is known about the mineral/water interface, however in the previous work of Bano et al. [132], similar ordering to calcite is identified.

The structure of water in our systems has been analysed using a variety of methods to try and provide a detailed account of the ordering.

7.4.5.1 1D density

One of the simplest methods to observe ordering is the density profile in a single dimension. In this work, the distribution of the water oxygen (OW) atoms has been calculated in the direction normal to the plane of the slab. For each OW atom, the distance to the outermost calcium ion for the nearest interface has been calculated. The probability density function of the distances is then estimated using a kernel density estimation (KDE) to provide a smooth, continuous distribution. Figure 7.7 shows the obtained KDE curves for all surfaces up to 12 Å.

The peak positions and relative sizes of the peaks for the $\{10\bar{1}4\}$ surface are in strong agreement with previous density profiles [144]. In all cases, there is very little long-range order, beyond 6 Å the water is generally bulk-like. For the least stable surfaces, $\{01\bar{1}2\}$ and $\{110\}CO_3$, there is negligible ordering, even at the interface. There is some semblance of structured water layers at the interface for all other surfaces. Calcite $\{10\bar{1}4\}$ shows arguably the most distinct layers, but there are numerous, less distinguishable, peaks in the $\{010\}$ and $\{100\}$ profiles. This lack of distinctness however may be an artefact of the chosen bandwidth (smoothing factor) for the KDE. Also interesting to note are the regions of zero density present in some of the curves, suggesting possible areas where water is entirely excluded.

So far we have only considered the distribution of water molecules in one dimension, for a more complete picture we need to analyse all three dimensions.

7.4.5.2 3D density

Along with the distance from the calcium carbonate slab, the other two coordinates of the OW atoms have been included in our density profiles. For each

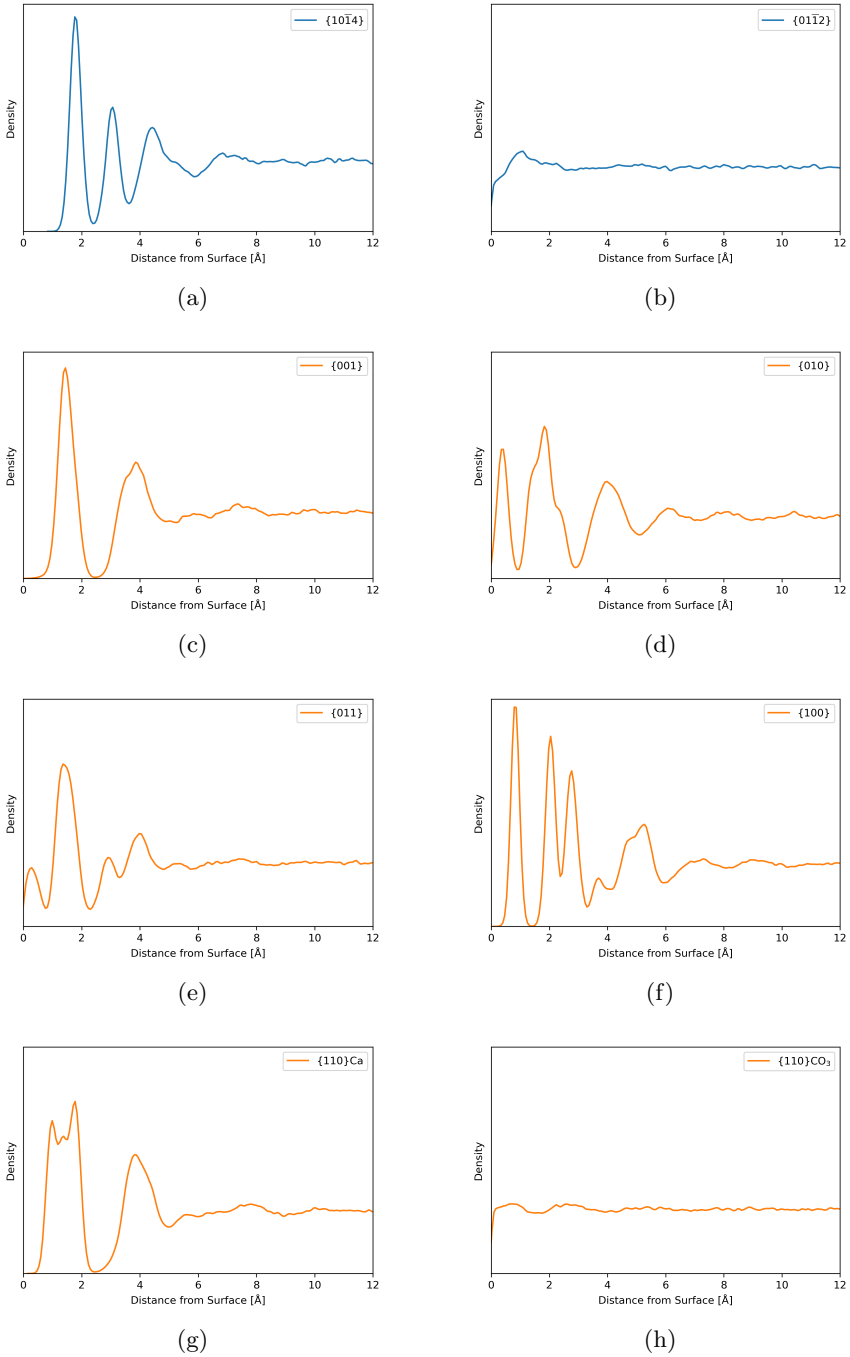

Figure 7.7: *Water oxygen density profiles in the perpendicular direction to the slab calculated via kernel density estimation. Both the calcite (blue) and aragonite (orange) surfaces are shown. Structured water layering is present at the surface of all but two surfaces,* (b) *and* (h)*, with the highest interfacial free energy.*

surface, two density profiles are presented in Figure 7.8, one for each coordinate plane perpendicular to the plane of the slab. The average plane parallel to the slab has not been shown as no ordering was detected. Note that the horizontal borders of the ZX plane for the calcite surfaces appear due to the non-orthogonal simulation cell.

The qualitative information from the 2D density plots expands on the analysis from the 1D density profile. Again, the two most unstable surfaces show very little ordering in either plane. Notably, the edges of these slabs have disorganised the most and thus far less ordering in the liquid layers compared to other surfaces. There is very strong ordering present in the {100} and the {110}Ca surfaces, particularly in the XY plane. The space available around the ions at the surface of the {100} slab allows the water to accumulate and order, as shown in Figure 7.8(f). A similar situation occurs in the {110}Ca and imposes the same pattern of ordering in at least the second water layer.

Apart from the {110}CO_3, all other aragonite surfaces show a degree of ordering in both planes. The denser regions of water and the patterns produced can be seen in both the density plot and the trajectory visualisation. In comparison to the highly structured aragonite surface edges mentioned previously, these aragonite surfaces are arguably rougher and more mobile leading to slightly less water ordering.

For the $\{10\bar{1}4\}$ surface, although there is a relatively strong degree of structuring shown in the ZX plane, there is comparatively little in the ZY plane. From this we can deduce that measuring the degree of order in only one dimension does not provide enough information and ordering in all dimensions should be considered.

So far, only the oxygen atom on the water molecules have been considered and the ordering is based entirely on its position. Applying the same procedure to the hydrogen atoms can provide an initial insight into any possible rotational ordering occurring within the system. The constructed density plots show ordering that aligns with the positional ordering from the oxygen atoms. Most molecules near the interface are constrained and rotational movement may be affected, however further analysis would be required to draw a more concrete conclusion.

Generally the degree of ordering in the density plots correlates to the entropy contribution of the respective system, when interpreting visually. However a method to quantify the order exhibited by the water is required.

7.4.5.3 Hydrogen Bonding

One way of determining the behaviour of the water at the interface is to look at the hydrogen bonding in the water. We can see if the hydrogen bonding at the interface is significantly different to the bulk hydrogen bonding to look at possible ordering.

For this work, a hydrogen bond between two water molecules is classified as such if the distance between the donor and acceptor oxygen atoms is $r < 3.5$ Å and if the angle between the donor, hydrogen and acceptor ions is $\theta < 30°$, as shown in Figure 7.9.

The average number of hydrogen bonds per water molecule in bulk water is calculated and used as a comparative value. At 300 K, the average number of hydrogen bonds is computed as 1.795 per molecule. A slab of water from the

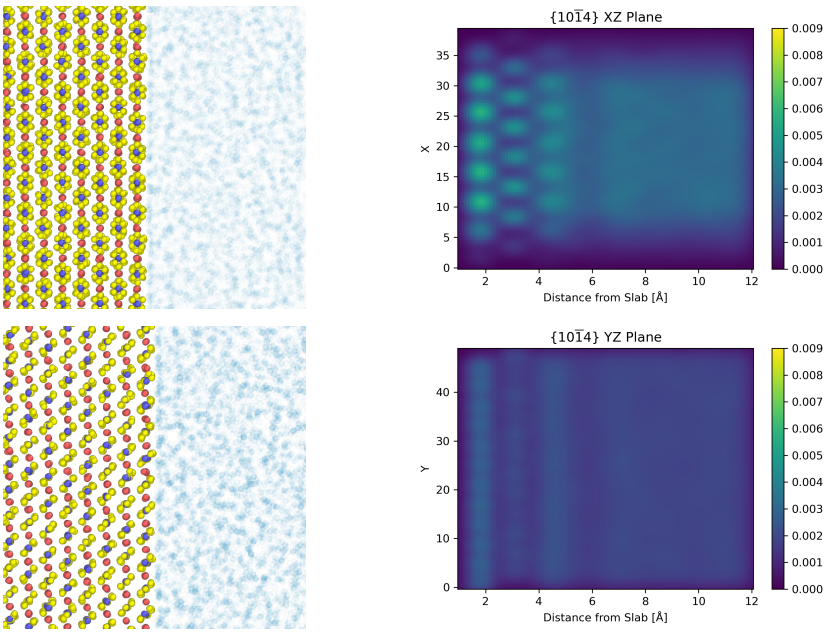
{10$\bar{1}$4} XZ Plane
X
Distance from Slab [Å]
{10$\bar{1}$4} YZ Plane
Y
Distance from Slab [Å]

(a)

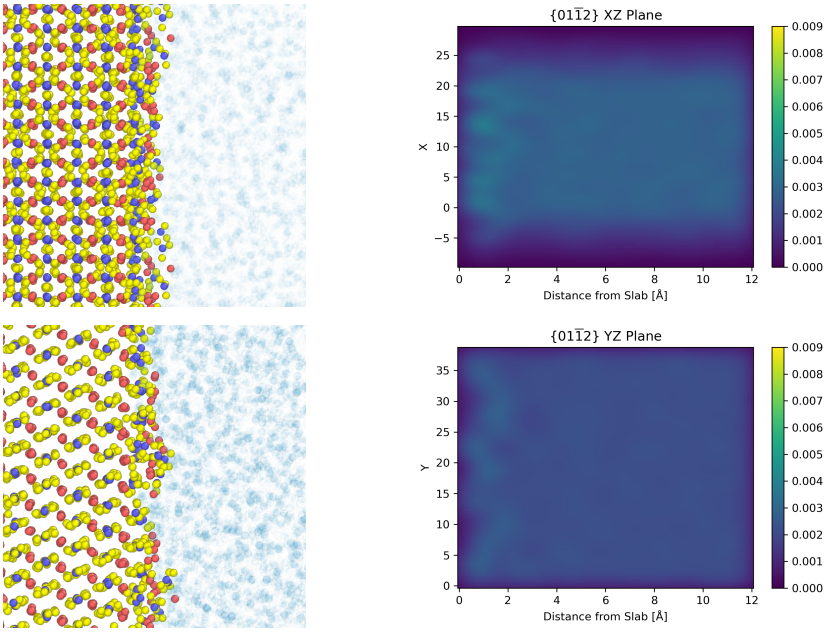
{01$\bar{1}$2} XZ Plane
X
Distance from Slab [Å]
{01$\bar{1}$2} YZ Plane
Y
Distance from Slab [Å]

(b)

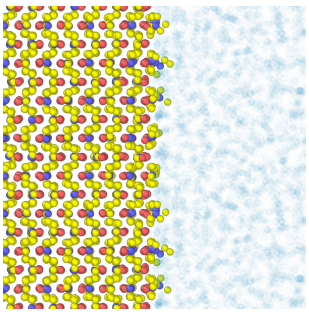

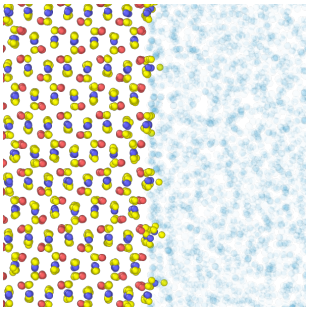

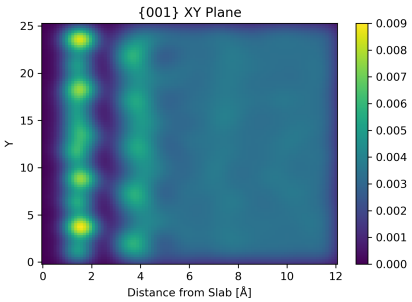
{001} XY Plane
Y
Distance from Slab [Å]

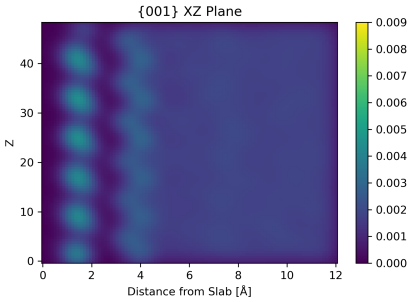
{001} XZ Plane
Z
Distance from Slab [Å]

(c)

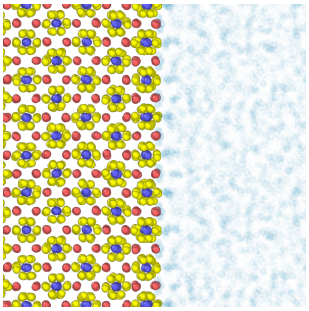

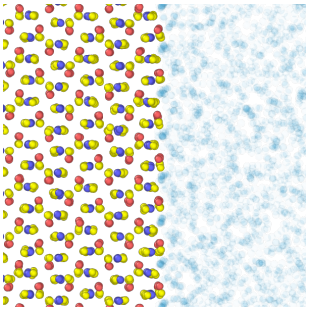

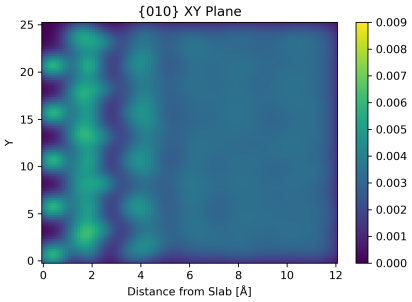
{010} XY Plane
Y
Distance from Slab [Å]

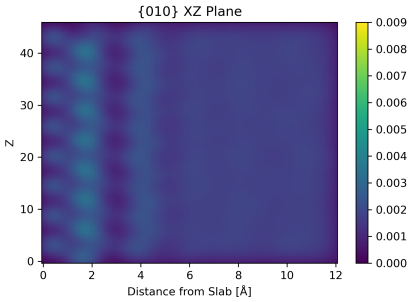
{010} XZ Plane
Z
Distance from Slab [Å]

(d)

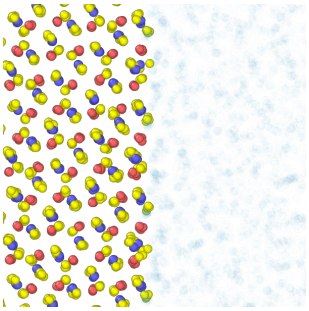

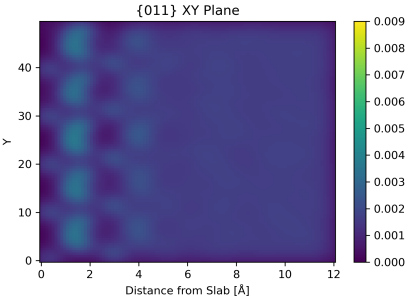
{011} XY Plane
Y
Distance from Slab [Å]

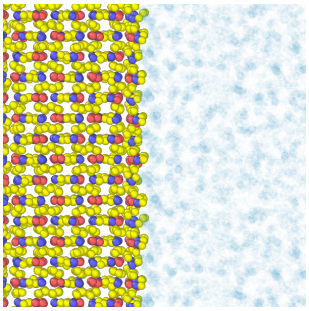

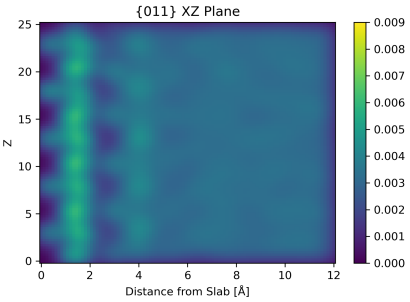
{011} XZ Plane
Z
Distance from Slab [Å]

(e)

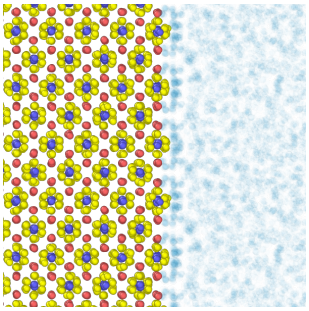

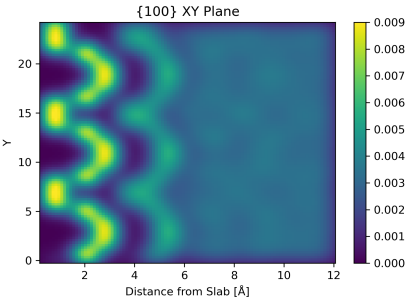
{100} XY Plane
Y
Distance from Slab [Å]

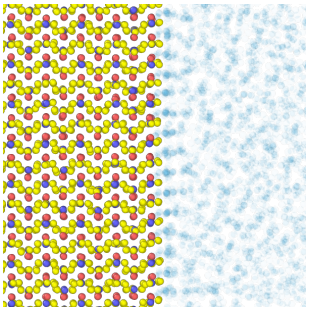

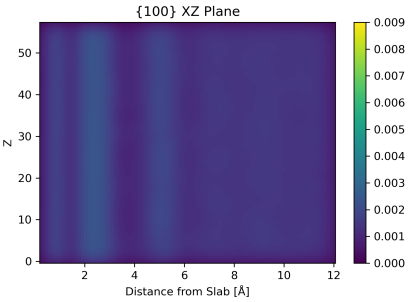
{100} XZ Plane
Z
Distance from Slab [Å]

(f)

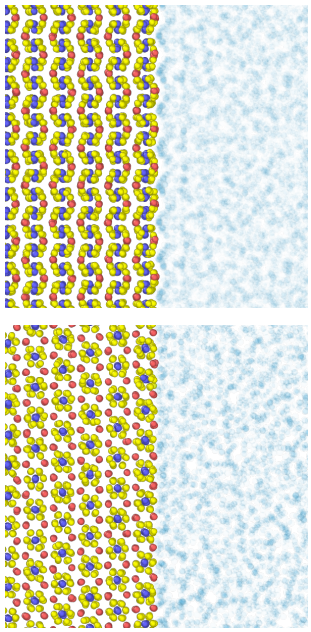

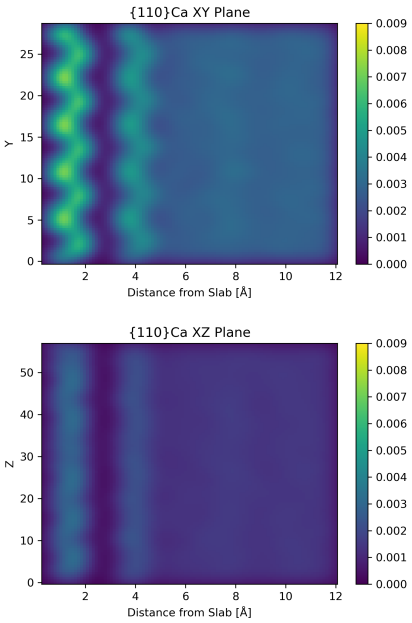

(g)

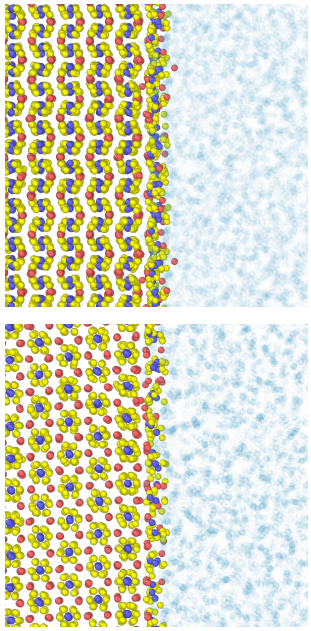

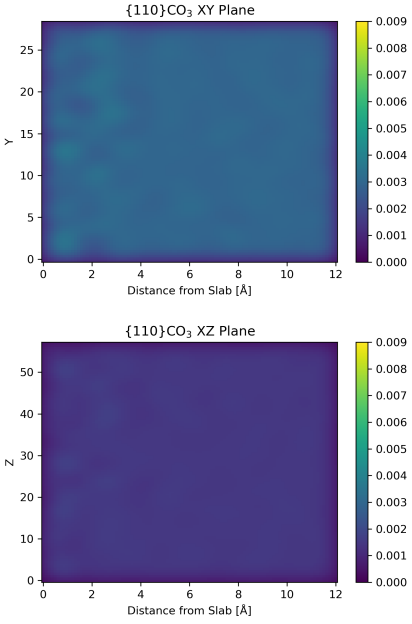

(h)

Figure 7.8: *Density plots for the calcite* (a)-(b) *and aragonite* (c)-(h) *surfaces alongside visualisation of the crystal-water interface. Note that the scale differs between the interface visual and the density plots.*

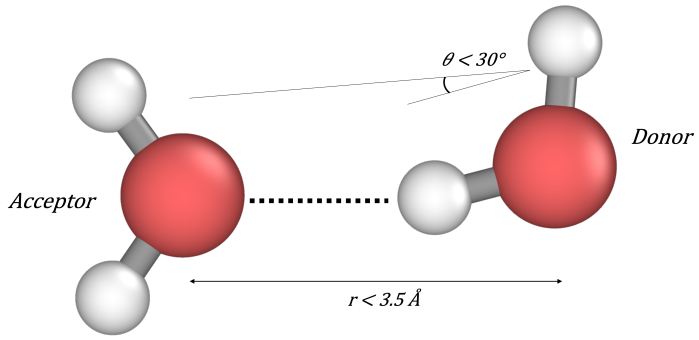

Figure 7.9: *Definition of hydrogen bonding between water molecules utilised in our analysis[146]. The bonding is defined by the distance r between donor and acceptor atoms and the angle θ between the acceptor, donor and hydrogen atoms.*

interface 6 Å wide defines the interfacial waters as this captures most of the ordering exhibited in Figure 7.8.

Variation of the average number of hydrogen bonds with distance from the slab is shown in Figure 7.10. Close to the slab, the number is always lower due to the reduced availability of other waters to bond to. As the distance from the surface increases, the average number of hydrogen bonds roughly tends to that of the bulk, although noise from the data causes discrepancies in some cases. In general, the peaks and troughs in the graph correspond with the high and low water regions as seen in the density plots.

The $\{10\bar{1}4\}$ surface shows relatively high degrees of hydrogen bonding due to the small distances (< 5 Å between centres in the x direction) between high density regions of water and between the layers of water perpendicular to the slab. It is likely that bonds can form in and between these regions. For the $\{001\}$, $\{010\}$ and $\{011\}$ surfaces of aragonite, there are slightly larger gaps between water regions than exhibited in the calcite surface and much more distinct separation between the water layers. Therefore the number of donors and acceptors available is lower, which is reflected in the lower average values in Figure 7.10.

Aragonite $\{100\}$ is the only system where the average number peaks above the bulk value, it then immediately drops to zero. This occurs in the densest regions at the surface suggesting very strong ordering is happening there. Given the apparent ordering exhibited by the waters in the $\{110\}$Ca system, the average number of hydrogen bonds is higher than one might expect in comparison to the other aragonite surfaces. However this particular system shows arguably the most distinct two water layers at the interface with a structure that possible favours hydrogen bonding across it, as the large peak occurs at the same position as the first water layer.

The most surprising results are that of the $\{01\bar{1}2\}$ and $\{110\}CO_3$ slabs. Considering the water densities of the two systems are almost uniform and most "bulk-like", one might expect that the hydrogen bonding would also be

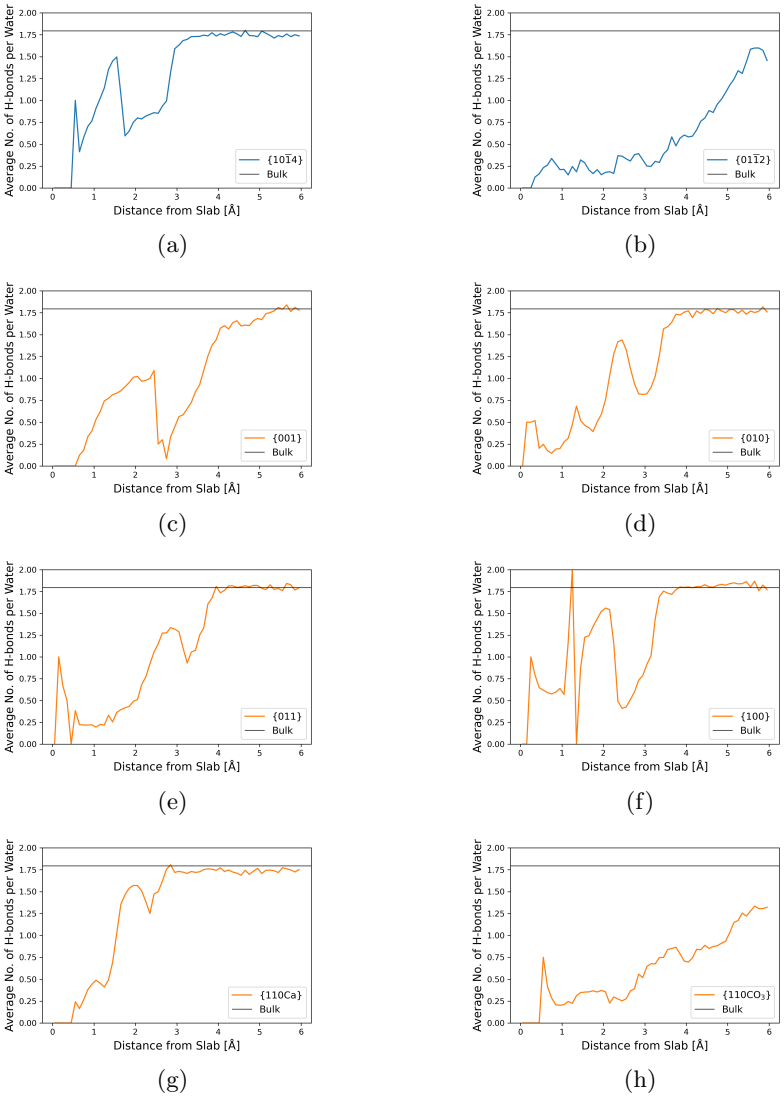

Figure 7.10: *Hydrogen bonding at the surface interface up to 6 Å. The average number of hydrogen bonds per water molecule are calculated for 0.1 Å regions from the surface and the position is determined by the donor atom's coordinate. Each value is compared to that calculated for the bulk water system, which is given by the black line at a value of 1.795 hydrogen bonds per water molecule.*

the similar to the bulk. Both systems show very low amounts of hydrogen bonding and the average value does not converge to that of the bulk until approximately 8 Å whereas the other systems reach the bulk value between 3 Å and 5 Å. Although there is little ordering shown in the density plots, water will still be interacting with the surface. It is possible that the waters are forced into positions with very little ordering but where hydrogen bonding is not possible. The surface edges themselves are significantly rougher than the other interfaces considered and so it is possible that the disorder at the surface causes this behaviour.

7.4.5.4 Quantifying Order

The task of quantifying order is not trivial. For a complete understanding there are many factors to consider; translational movement, rotational movement, molecular orientation and time or distance correlations. As such the aim of our ordering factor is to quantify the structure (or lack thereof) displayed in Figure 7.8 as a single value.

Regions of both high and low densities of water molecules are present in most of the systems. It is important to consider both as a form of ordering and ensure that their effects are not cancelled out in the calculation process. The distribution of water molecules as determined by their oxygen atom position is used to quantify the degree of ordering at the interface. As the bulk water is highly disordered, any deviation from this distribution can be deemed as water ordering.

A 6 Å slab of water at the interface (interfacial waters) is compared to a slab of equal width (bulk water) at 12 Å from the interface, where the water shows bulk behaviour. Due to the density smearing at the edges of the calcite surfaces, the water slabs are also restricted in a second dimension to avoid the artificial influence of the non-orthogonal cell. Orthogonal regions within the systems are instead chosen.

The positions in both slabs are binned in cubic regions to determine the number of waters present. The difference between the distributions of interfacial and bulk waters are calculated. A value around zero suggests that the interfacial water is the same as the bulk. Positive values far from zero suggests there are more waters at the interface than in bulk and similarly for negative values, fewer waters or no waters are present. The statistical deviation from zero is then calculated to produce a single value, deemed the ordering factor, f_{order}. A greater value of f_{order} suggests greater deviation from the bulk and therefore more ordering has occurred.

With the proposed method, there is a significant dependence of the final value on the chosen bin size. To select an appropriate bin size, convergence tests have been run on a separate system of bulk water. The number of frames sampled for the bulk system to be considered homogeneous is calculated. Homogeneity is defined by the standard deviation of the water density across planes of the system and then normalised by bin area; a low standard deviation suggests a more constant density across the system and thus a more homogeneous system. Figure 7.11 shows the results starting from a bin with 1 Å sides, down to 0.20 Å. The number of frames required for homogeneity will continue to decrease with bin volume. However, for a balance with computational expense, a bin size of 0.25 Å has been used for the interfacial systems.

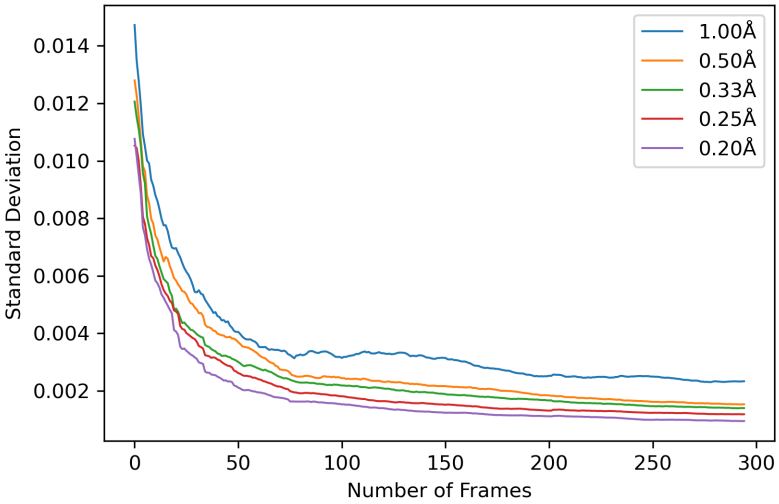

Figure 7.11: *Convergence of the spread of density (defined using the standard deviation) as the number of trajectory frames included in the calculation increases for multiple cubic bin length values. A smaller spread correlates to a more homogeneous system.*

The ordering factor gives a simple but sufficient measure of how the water in the system is structured, values of which are presented in Figure 7.12. From the density plots in Figure 7.8, the {100} surface is the most ordered, which is reflected in the values obtained. Relative ordering in the other aragonite planes is harder to distinguish and the ordering factors lie closely together. The $\{01\bar{1}2\}$ and $\{110\}CO_3$ show the least structured water and thus obtain the lowest values of f_{order}. Somewhat surprising is the low value for the $\{10\bar{1}4\}$ since the ordering is shown in the 1D density and in the XZ plane density profiles. However when considering the lesser ordering in the YZ plane and the smaller difference in region density in comparison to the aragonite surfaces, the resultant low value seems reasonable.

With the water ordering quantified, we can compare the structuring observed to the entropies of the respective system. Figure 7.13 details how the ordering factor varies with both the change in entropy, $-\Delta S$, and the proportion of the free energy that is due to entropy. The Pearson correlation coefficient was calculated for the ordering factor with both these parameters and the values are detailed in the legend of Figure 7.13. Neither variable has a distinctly linear relationship with the order parameter, however the values are large enough to consider correlation between the two. There is a significantly stronger correlation between the entropy fraction than with the entropy change. Additionally the Spearman's Rank correlation coefficients were calculated for the entropy change and entropy fraction as 0.143 and 0.833 respectively, reinforcing the much stronger correlation between the entropy fraction and ordering factor. From this we can determine that ordering in the liquid at the interface will not be the only factor to dictate the absolute change in entropy; the interplay

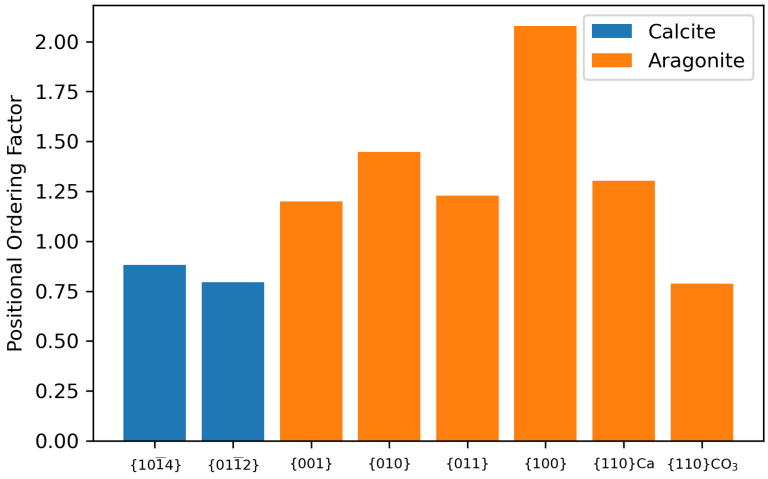

(a)

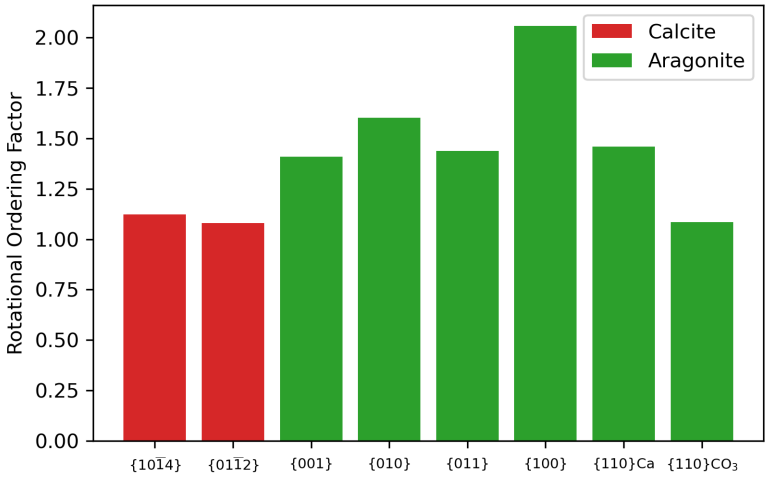

(b)

Figure 7.12: *Positional* (a) *and rotational* (b) *ordering factor for interfacial waters in both the calcite and aragonite systems. The higher the factor the greater the structuring of the waters at the interface. The calculated values generally describe the relative order expressed in* Figure 7.8*, encapsulating the ordering in all 3 dimensions.*

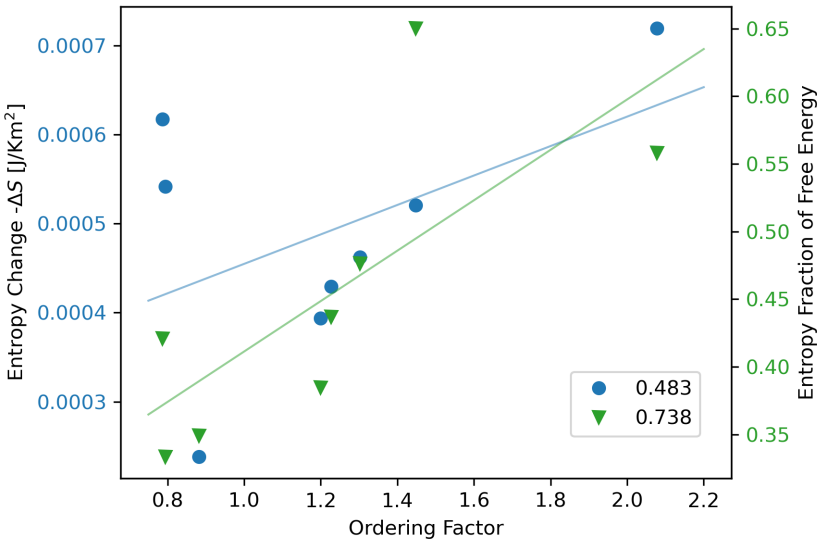

Figure 7.13: *Determining the relationship between our calculated ordering factor and both the entropy change of the system (blue circles) and the entropy fraction of the free energy (green triangles). The legend shows the Pearson correlation coefficient for both variables with the ordering factor. Although the ordering shows some relationship with both, the quantitative value for the entropy fraction is significantly stronger.*

between the entropy and enthalpy contributions has a more prominent effect on the system.

7.5 Conclusions

From our initial investigation, it is clear the entropy plays a prominent role in the interfacial energies of calcium carbonate. The entropic contribution to the free energy, and thus the enthalpic contribution, varies considerably across the surfaces and a uniform entropy correction is not sufficient for crystal/liquid interfacial energy calculations.

Moreover there is a clear distinction between the two polymorphs with the metastable aragonite surfaces having on average a much higher entropic contribution than the calcite surfaces. Distinct water ordering at the interface is clear from the 1D density profiles. Observing the density of water in all 3 dimensions highlights further ordering occurring in the planes of the system. Additionally, the surface characteristics influence the water structuring and thus the entropy lost in the system; for the "rough" surfaces there is very little ordering imposed in the liquid; surfaces with sufficient space available trap water at the interface creating a highly ordered structure. The hydrogen bonding in the system also demonstrates the differing restrictions imposed on the water molecules. Despite bulk-like disorder in some systems, the hydrogen bonding is not the same as the bulk and the waters are restricted such that this bonding is not possible.

There is a strong resemblance between the hydrogen bonding profile and the layered structure of water at the corresponding interface. It is well known that there are structured water layers at the calcite $\{10\bar{1}4\}$ interface, however there is arguably more found at the aragonite interfaces.

Our simple approach to quantifying the water ordering effectively quantifies the density profiles of the 3D liquid. There is also a particularly strong correlation between the ordering factor and the entropy *fraction* of the system, as opposed to the entropy change. This suggests that the relative contributions of enthalpy and entropy within the solid/liquid interface influences the ordering seen. Therefore, given the importance of the enthalpy-entropy balance determined, the logical next step is to determine how this varies with temperature.

Chapter 8

Temperature Effects on Interfacial Free Energies

Utilising the Einstein crystal method to calculate interfacial free energies of both calcite and aragonite surfaces highlights the importance of the entropic contribution and its interplay with the enthalpic contribution. Only calculating surface enthalpies or including a constant entropy correction across all surfaces is not sufficient when investigating nucleation and polymorph selection.

In classical thermodynamics entropy, dS, is related to the temperature, T, of a closed system by $dS = \delta Q/T$, where δQ is the transfer of heat to the system. Given the importance of entropy and its relationship with temperature, we want to investigate how the interfacial free energies, and thus the entropic and enthalpic contributions, of our selected surfaces vary with temperature.

Furthermore, in Section 3.1.1 we discussed the known effects of high temperature on aragonite selection over calcite. However, it is still not established why this occurs. Therefore, by calculating the interfacial energies at temperatures within the known region of aragonite precipitation, we can provide possible insight into temperature effect on polymorph selection in calcium carbonate.

8.1 Free Energies, Enthalpies and Entropies

The previous free energies calculations we performed were all at 300 K. For this work, the procedure detailed in Chapter 7, using the Einstein crystal as a reference state for thermodynamic integration, has been repeated at temperatures ranging from 280 K to 450 K. One of the advantages of the method [4] is the ability to reuse calculated values for the bulk phases and chosen liquid, however these must be recomputed for each temperature.

8.1.1 Bulk Calcite and Aragonite

Free energies and enthalpies of the bulk phases of calcite and aragonite have been computed at a range of temperature values as shown in Figure 8.1 and Table 8.1. For both free energy and enthalpies, calcite is lower at all temperatures and there is no crossover point at which aragonite becomes the more stable form.

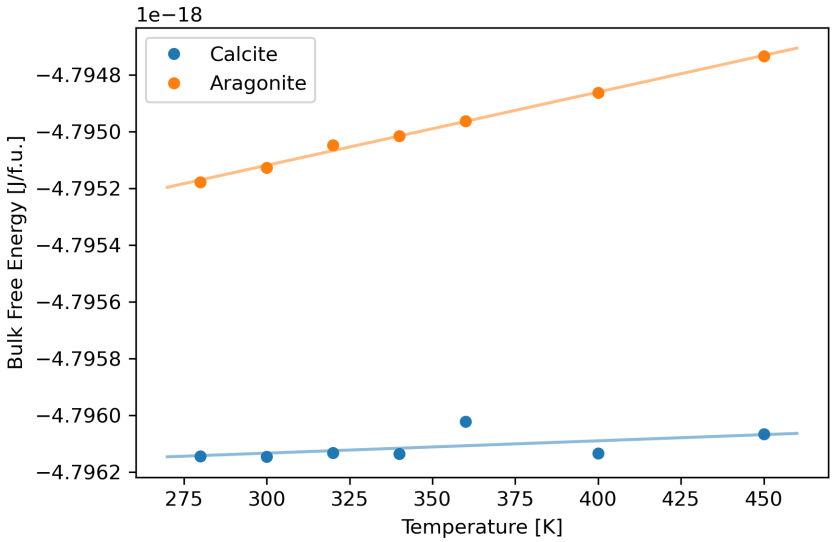

(a)

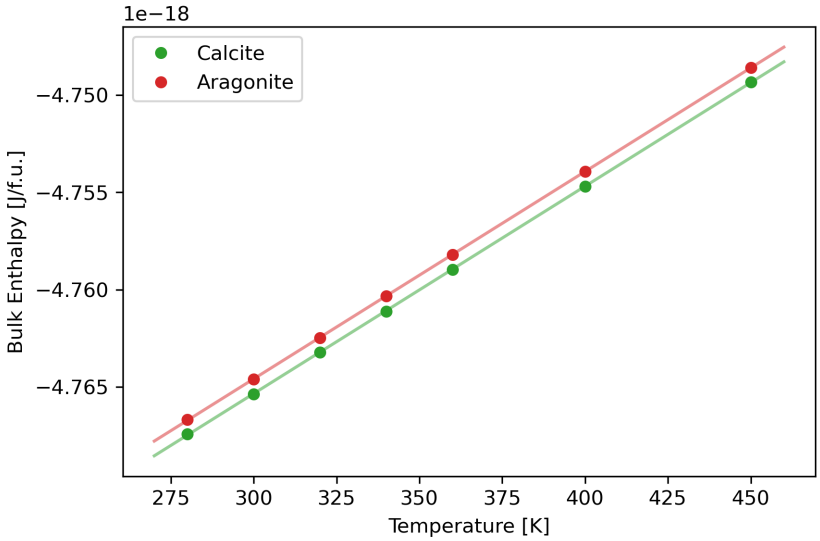

(b)

Figure 8.1: *Free energy* (a) *and enthalpy* (b) *cohesive energy values calculated for bulk calcite and aragonite via the Einstein crystal method for various temperatures.*

	Calcite		Aragonite	
T [K]	ΔF [J/F.U. $\times 10^{-18}$]	ΔH [J $\times 10^{-18}$]	ΔF [J/F.U. $\times 10^{-18}$]	ΔH [J $\times 10^{-18}$]
280	-4.79614	-4.76741	-4.79518	-4.76668
300	-4.79615	-4.76536	-4.79513	-4.7646
320	-4.79613	-4.76321	-4.79505	-4.76247
340	-4.79614	-4.76112	-4.79502	-4.76032
360	-4.79602	-4.75897	-4.79496	-4.7582
400	-4.79613	-4.7547	-4.79486	-4.75393
500	-4.79607	-4.74934	-4.79473	-4.74861

Table 8.1: *Values for the bulk free energy and enthalpy for calcite and aragonite with temperature increase.*

It has been established that the effect of temperature on polymorph selection is not due to thermodynamics and therefore it is expected for bulk aragonite to always have the highest energy. Although aragonite is the least stable, there is very little difference between aragonite and calcite ($\sim 0.02\%$) at all temperatures. The difference does increase as the temperature is raised, since the rate at which the aragonite energy increases is greater than the rate for calcite.

The difference between the calcite and aragonite enthalpies is much smaller and both increase at approximately the same rate. Experimentally, the magnitude of the aragonite enthalpy is greater than the calcite enthalpy [143]. However, the forcefield used in this work is known to get the enthalpy stabilities the wrong way round [144]. Our calculated difference between the two phases is of the same magnitude as the experimental results.

The variation in the resultant free energies and enthalpies of the bulk calcite and aragonite systems is as expected from both experimental and previous computational studies. Therefore we can feel confident in using the Einstein reference state method at temperatures other than 300 K, provided the chosen water forcefield also behaves.

8.1.2 Water Surface Tension and Enthalpy

In addition to the bulk calcium carbonate values, free energies and enthalpies of the water/vacuum interface and the enthalpies of the bulk water at the selected temperatures have been calculated. An important point to note is that the melting and boiling point of the water model SPC/Fw [120], do not align with the known temperatures for water. In fact, the melting and boiling points for our chosen model are not well known. For the rigid water model SPC/E, the melting and boiling temperatures are quoted as 215 K [147] and 396 K [148] respectively. Although we are not interested in the behaviour at the transition points, we are interested in the temperature region at which aragonite becomes favoured over calcite ($\sim$ 330 - 350 K). However, given the transition points are unknown for the water model, this temperature range for aragonite formation is also unknown. The boiling point quoted is only somewhat larger than the known value for water, however other estimates and other models predict substantially higher values. Therefore we have elected to expand our temperature range in hopes of encapsulating the surface behaviour around the point at which aragonite is favoured.

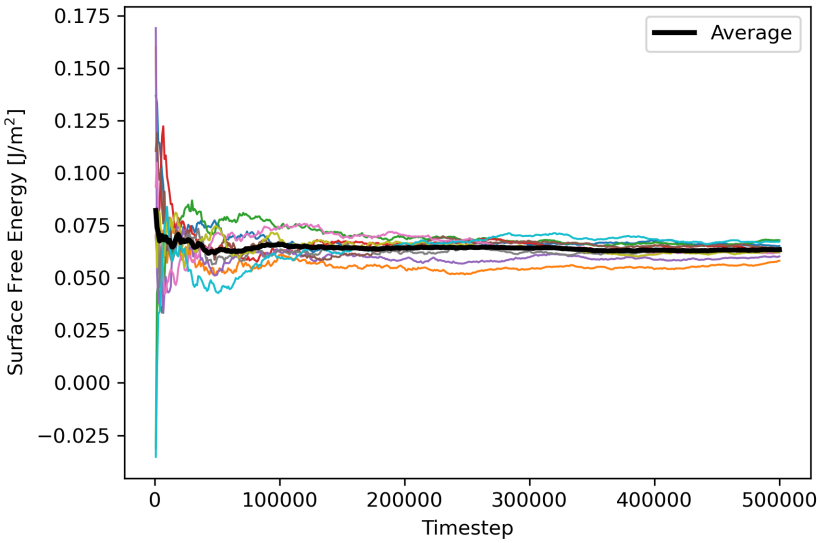

Figure 8.2: *Example of results from the Kirkwood-Buff calculation of water surface tension at 280 K. Ten different MD simulations were run and the average value calculated at each timestep.*

We have used the Kirkwood-Buff method to calculate the surface free energy (surface tension) of the water, in the same manner as the original paper [4]. Similar to the TI setup, a thick layer of liquid is aligned in the xy plane in contact with vacuum either side creating two water/vacuum interfaces. The surface tension γ_{Liquid} is then calculated from a single simulation run from

$$\gamma_{Liquid} = \frac{1}{2}\int_0^{L_z} \left[P_{zz} - 0.5(P_{xx} + P_{yy})\right] dz \tag{8.1}$$

where P_{xx}, P_{yy} and P_{zz} are the diagonal components of the pressure tensor and L_z is the length of the simulation cell in the z direction. The average pressure tensor is calculated across thin slices in the z direction and then integrated numerically. The calculated surface tension as the number of included timesteps increases is shown for 10 different simulation runs in Figure 8.2. An average across all 10 runs is computed and the average value at the end of the simulations is taken as the surface tension of water for that specific temperature.

Calculated surface free energies (surface tension) of water from 280 K to 500 K are shown in Figure 8.3. The values show an approximately linear dependence on temperature, in line with expected findings [149]. Experimentally, the surface tension of water at 300 K is 0.072 J/m^2 (72 mN/m), slightly larger than our value of 0.058 J/m^2. A similar discrepancy is present for all temperatures. However it is known that the chosen water model underestimates the water tension [150] but given the similarity in gradients of the computed and experimental results, are results are sufficient for use in further calculations.

Water enthalpies are much simpler to calculate. The bulk enthalpies are determined by the average enthalpy across a bulk water simulation run, normalised for the number of waters molecules present. The values show a strong

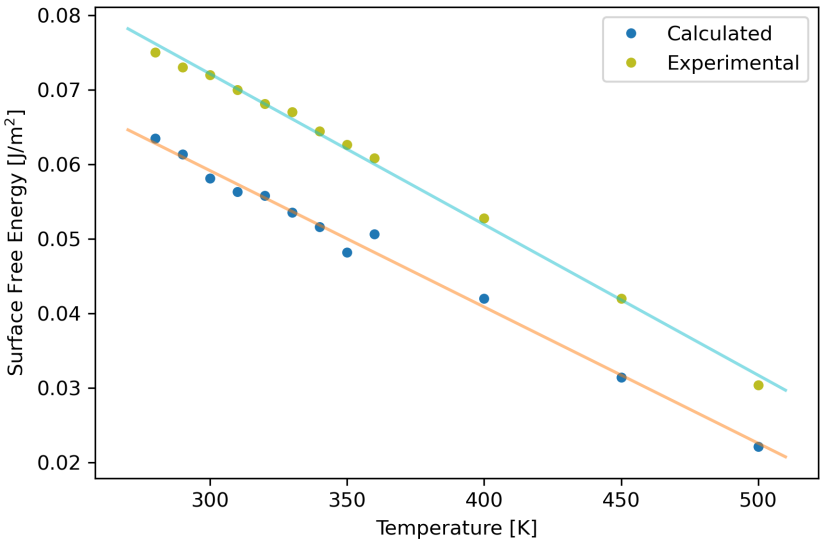

Figure 8.3: *Comparison of calculated surface free energies of water and experimental values from*[151]*. Solid lines shown to indicate the approximate linear relationship.*

linear trend in Figure 8.4a, the bulk enthalpy increases as the temperature rises. For the surface enthalpies, the procedure is slightly more complicated. It can be calculated from the simulation runs used previously for the Kirkwood-Buff method. The average enthalpy over the simulation run is again averaged across the 10 MD runs. Surface enthalpy $\Delta H_{Liquid/Vacuum}$ of the water/vacuum interface is given by

$$\Delta H_{Liquid/Vacuum} = \frac{\Delta H_{Average} - N\Delta H_{Liquid}}{2A} \tag{8.2}$$

where $\Delta H_{Average}$ is the average across multiple simulation runs and ΔH_{Liquid} is the bulk surface enthalpy calculated earlier. The number of water molecules in the system is given by N, and A is the surface area of the water/vacuum interface.

Figure 8.4 shows how the surface enthalpy alters with temperature. Unlike for the bulk, the surface enthalpies do not vary linearly as the temperature increases. There is an apparent decrease in the rate of enthalpy increase around 360 K and then the enthalpy plateaus between 400 K and 450 K.

The calculated values can be reused in all calculations performed at the same temperature.

8.1.3 Calcite and Aragonite Surfaces

As with the calculations at 300 K, the interfacial free energies of each surface at all temperatures are computed via TI. Enthalpies are then calculated from a single simulation and the entropy of the system is determined as the difference in free energy and enthalpy, $-T\Delta S = \Delta F - \Delta H$. The values are shown

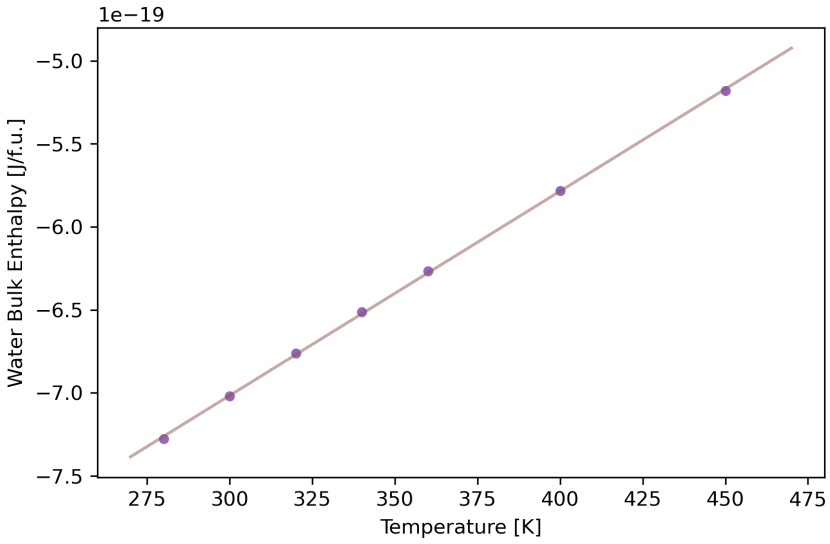

(a)

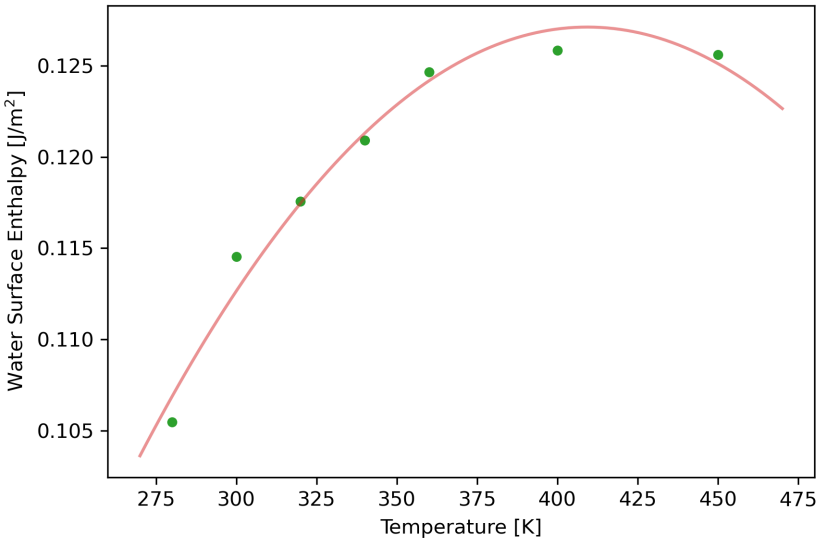

(b)

Figure 8.4: *Calculated bulk water enthalpies* (a) *and water surface enthalpies* (b) *from 280 to 450 K.*

in Figure 8.5 across all temperatures. In general, the free energies increase as the temperature increases. The relative energies and stabilities of the surfaces change very little across the temperature range; only some surfaces with close energy values alter stability, such as the {100} and {110}CO_3 surfaces of aragonite. At all temperatures, the $\{10\bar{1}4\}$ surface has the lowest free energy and thus calcite is the most stable polymorph. As with the bulk free energies, the gap between the lowest calcite surface, $\{10\bar{1}4\}$, and the lowest aragonite surface, {010}, increases with temperature.

Furthermore, the fraction of free energy due to entropy is not constant across temperature changes. Figure 8.6 details how the entropy fraction varies for each individual surface. In general, the entropy fraction initially increases, reaches a maximum between 350-450 K, before decreasing at higher temperatures. The most stable aragonite surface, {010}, also has the highest entropy contribution with a maximum greater than 76% of the free energy resulting from entropy at 380 K. Surfaces with lower entropy contributions, $\{10\bar{1}4\}$ calcite and {001} aragonite, exhibit a maximum entropy contribution at a lower temperature than surfaces with lower entropy contributions and high free energies, $\{01\bar{1}2\}$ and {110}CO_3. These surfaces exhibit a maximum at a higher temperature. Figure 8.7 compares the temperature at which the maximum entropy fraction occurs with the average free energy for the surface. There is good agreement with the relationship between these two variables. It is possible that for the more unstable surfaces, the water is more tightly bound to the surface, as evidenced by the high enthalpy contribution and therefore a higher temperature is required for the entropy contribution to dominate. The only anomaly appears to be the {011} surface (purple triangles), the free energy and entropy fraction at 450 K are higher than expected in comparison with the other surfaces and therefore the trend line has been omitted and the temperature of the maximum has not been calculated.

A more thorough look at how the free energies and its contributions vary for each individual surface are presented in Figure 8.8. As discussed previously, the free energy increases with temperature for most surfaces. The enthalpy of the system initially decreases with temperature but at the higher temperatures considered, the enthalpy begins to increase. Since the entropy is calculated from the difference in free energy and enthalpy, it mirrors the trend of the enthalpy values; initially increasing and then decreasing with raised temperature.

Our results suggest that free energy and temperatures follow a cubic relationship for both calcite and aragonite surfaces. The Gibbs free energy, free energy under constant pressure and temperature as we have calculated, is given by

$$\Delta F = \Delta H - T\Delta S \tag{8.3}$$

and differentiating with respect to T, results in the expression,

$$\frac{\partial \Delta F}{\partial T} = -\Delta S \tag{8.4}$$

therefore the differential of the change in free energy with temperature should be equivalent to the negative of the change in entropy. According to this, our entropy values should follow a quadratic curve as the free energy follows a cubic curve. The left-hand curves in Figure 8.8 nearly all exhibit a quadratic-like curve, consistent with Equation 8.4.

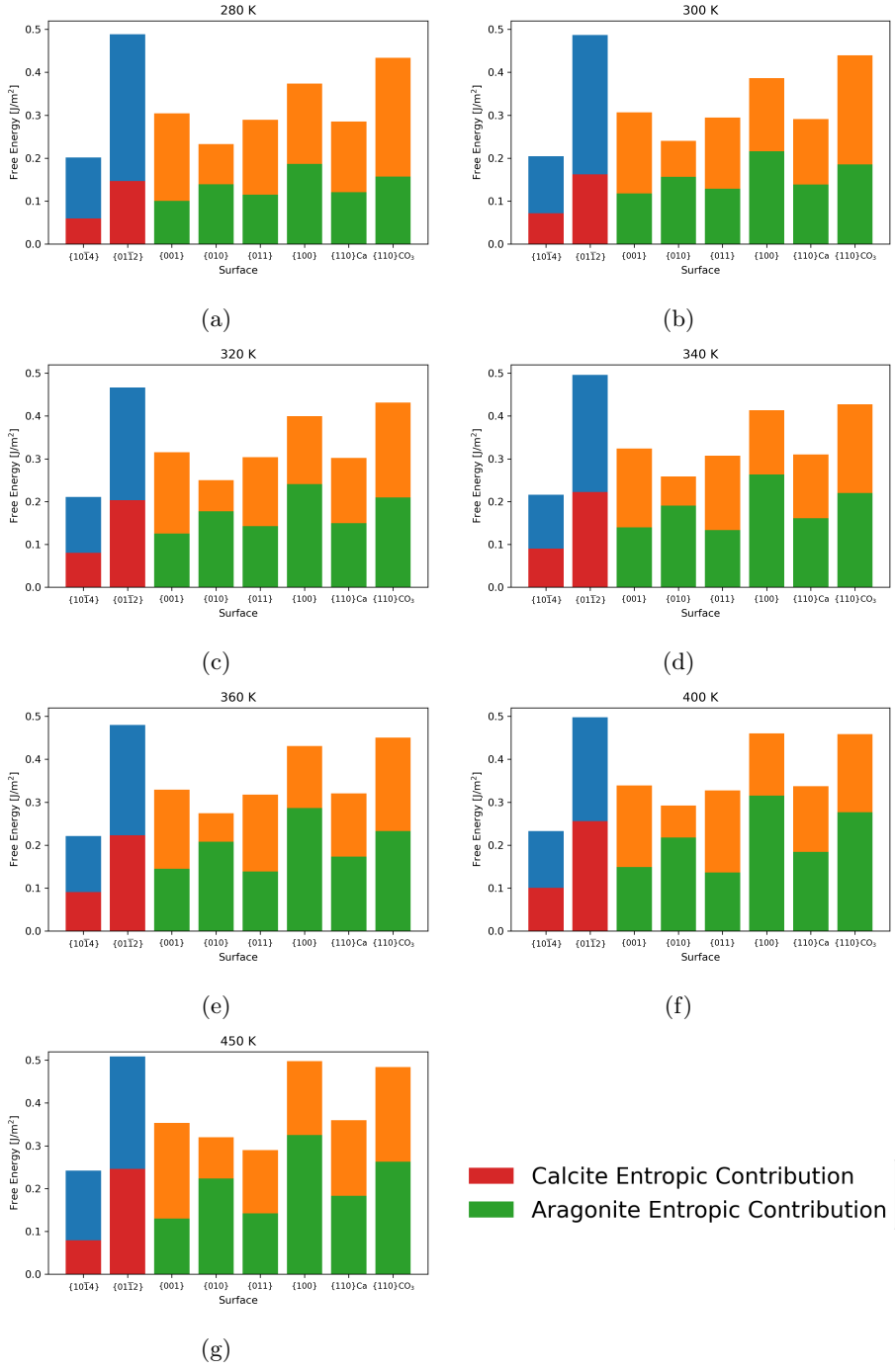

Figure 8.5: *Interfacial free energies for all surfaces across various temperatures. The entropy contribution is highlighted for calcite (red) and aragonite (green) with the enthalpy contribution given by the remaining free energy for calcite (blue) and aragonite (orange).*

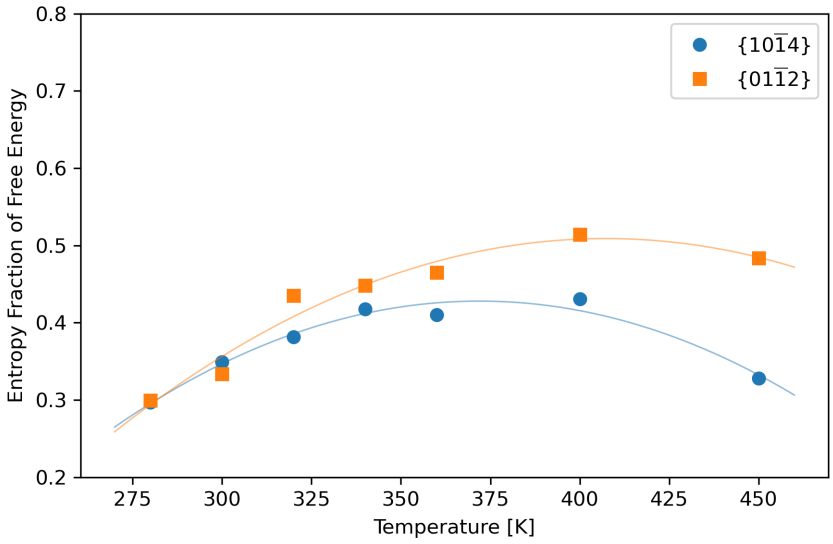

(a)

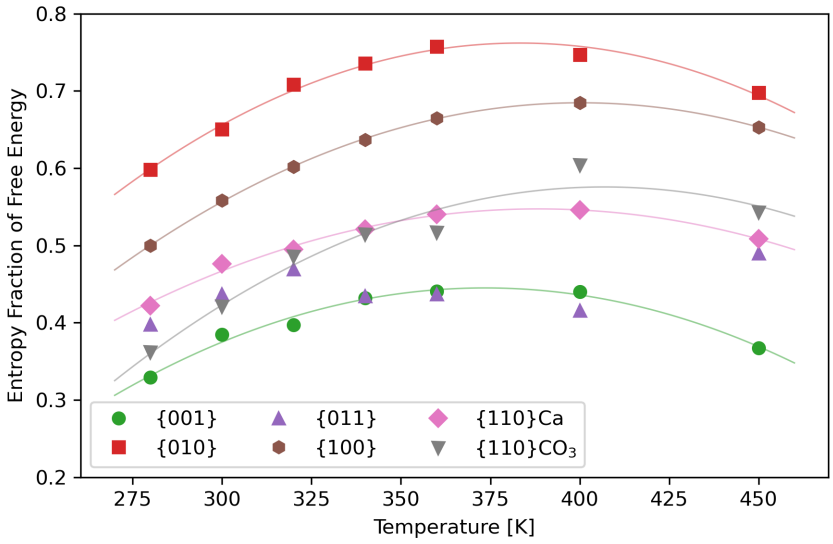

(b)

Figure 8.6: *The entropy fraction of the free energy variation with temperature of individual surfaces for both calcite* (a) *and aragonite* (b).

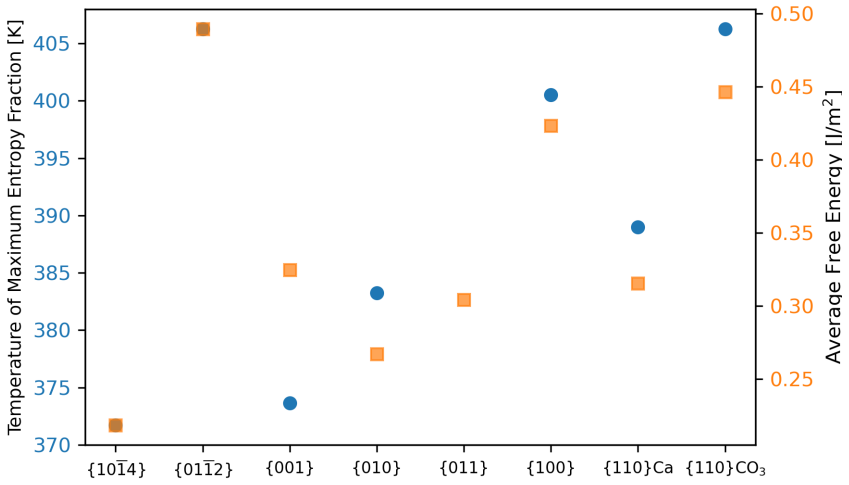

Figure 8.7: *Temperature at which the maximum entropy contribution occurs (blue) for each surface compared with the average free energy across all temperatures (orange).*

The equation also provides an alternative method of calculating the entropy; by differentiating the fitted free energy curve $\Delta F = aT^3 + bT^2 + cT + d$ to find the entropy $\Delta S = -3aT^2 - 2bT - c$, where the constants a, b, c and d have been calculated for each surface. Values computed from the difference in free energy and enthalpy are compared to the values from the differential in the right-hand plots in Figure 8.8. In all instances, the derivative calculated values of the entropy are larger than our values from the TI simulations; all of our computed values are negative, however some predicted values come out positive. Despite the change in sign and offset, the shape of the curve generally fits the calculated entropy values.

As previously noted the {011} aragonite surface stands out with its free energy decreasing considerably at 450 K. When visualising the trajectory of the {011} surface at this temperature, it is apparent that the aragonite slab is melting (see Figure 8.9) and thus the comparison to the bulk crystal and Einstein reference state are not applicable. Neither the bulk aragonite state nor the other aragonite surfaces melt at 450 K. Therefore the calculation should be run again using a greater slab width in hope of preventing the melting of the slab.

8.2 Crystal Morphologies

With the interfacial free energy values calculated at different temperatures, the expected equilibrium crystal morphology can again be deduced using Wulff construction. For calcite, the {10$\bar{1}$4} surfaces is always the most stable with free energy values considerably lower than the {01$\bar{1}$2} surface. Therefore the calcite

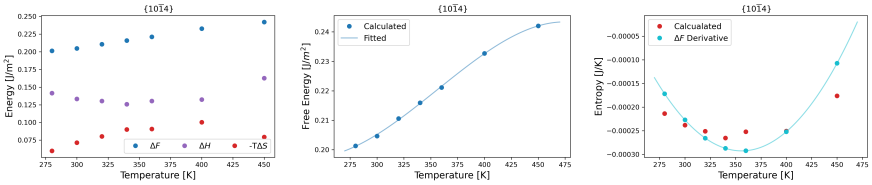
{10$\bar{1}$4}
Energy [J/m^2]
Temperature [K]
ΔF
ΔH
-TΔS
Free Energy [J/m^2]
Calculated
Fitted
Entropy [J/K]
ΔF Derivative

(a)

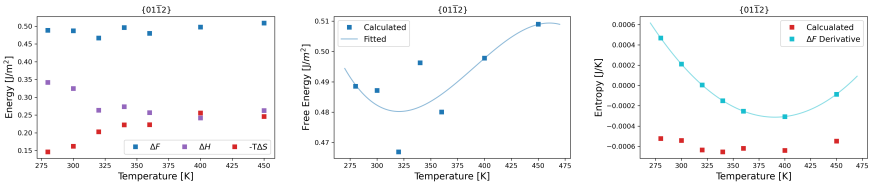
{01$\bar{1}$2}
Energy [J/m^2]
Temperature [K]
ΔF
ΔH
-TΔS
Free Energy [J/m^2]
Calculated
Fitted
Entropy [J/K]
ΔF Derivative

(b)

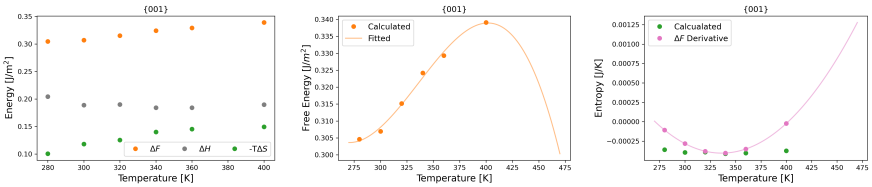
{001}
Energy [J/m^2]
Temperature [K]
ΔF
ΔH
-TΔS
Free Energy [J/m^2]
Calculated
Fitted
Entropy [J/K]
ΔF Derivative

(c)

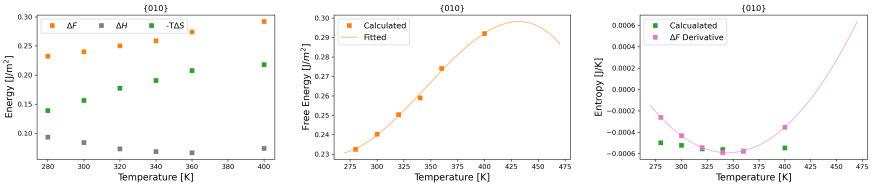
{010}
Energy [J/m^2]
Temperature [K]
ΔF
ΔH
-TΔS
Free Energy [J/m^2]
Calculated
Fitted
Entropy [J/K]
ΔF Derivative

(d)

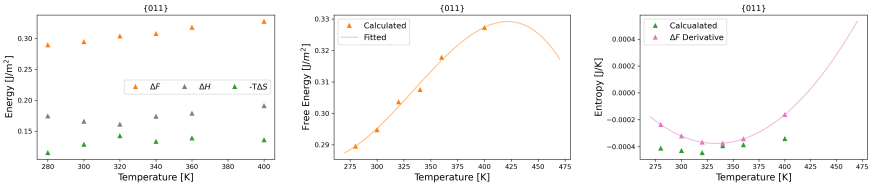
{011}
Energy [J/m^2]
Temperature [K]
ΔF
ΔH
-TΔS
Free Energy [J/m^2]
Calculated
Fitted
Entropy [J/K]
ΔF Derivative

(e)

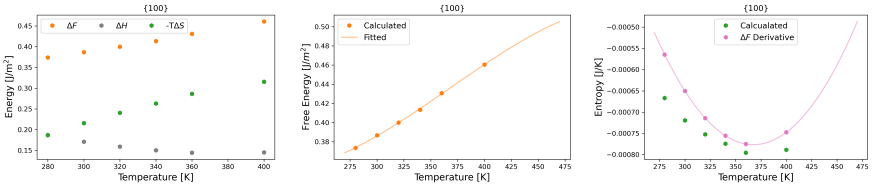
{100}
Energy [J/m^2]
Temperature [K]
ΔF
ΔH
-TΔS
Free Energy [J/m^2]
Calculated
Fitted
Entropy [J/K]
ΔF Derivative

(f)

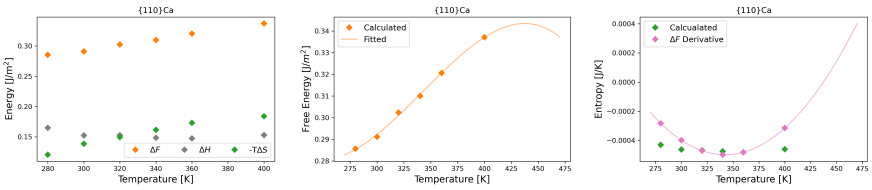

(g)

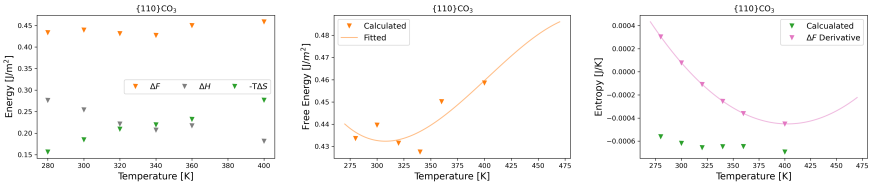

(h)

Figure 8.8: *Free energy ΔF, enthalpy ΔH and entropy $-T\Delta S$ variation with temperature (left). Cubic polynomial fit for free energy with temperature (centre). Entropy values calculated from the derivation of the free energy fit compared with the computed entropy values from the TI calculations (right).*

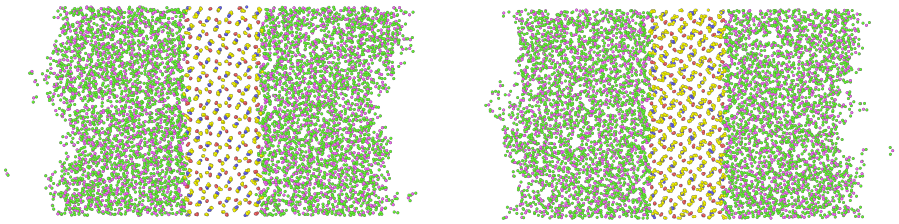

(a) 400 K (b) 450 K

Figure 8.9: *Comparison of the $\{011\}$ aragonite slab at 400 K* (a) *and at 450 K* (b) *when the solid slab has begun melting.*

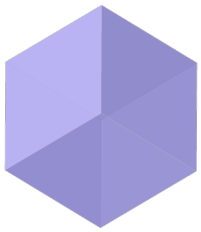

(a)

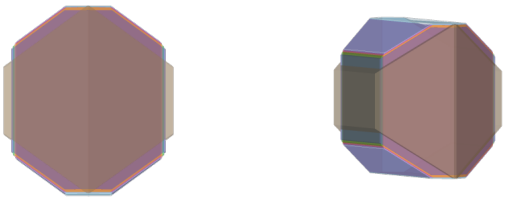

(b)

Figure 8.10: *Computed crystal morphology with the Wulff construction for calcite* (a) *and aragonite* (b). *Each colour represents a different temperature. There is no change for the calcite morphology and very little change for aragonite, expect at 450 K (brown morphology).*

morphology does not change with temperature. The morphology in Figure 8.10a is the same as the morphology shown in Chapter 7 at 300 K. The average interfacial energy of the crystal, γ_{Nano}, will increase with temperature but the shape factor, f_{Nano}, does not change.

There is a small change in morphology with temperature for aragonite. Excluding the morphology produced at 450 K, the expressed surfaces remain the same with some slight changes in the relative sizes of the {001}, {010}, {011} and {110} surfaces. The brown morphology in Figure 8.10b shows the expected equilibrium morphology at 450 K from our calculated values. It is the only case to show a different morphology due to the decrease in the free energy of the {011} surface from 400 K to 450 K. The {011} surface is far more pronounced than for calculations at lower temperatures and the {001} surface is omitted. Given the anomalous nature of the energy result at 450 K, the resultant morphology is not conclusive and the calculation should be repeated for greater confidence.

As with the initial results from 300 K, the free energy of converting a calcite nanoparticle to an aragonite nanoparticle as a function of the number of formula units, n, is computed and plotted in Figure 8.11. For all temperature values considered, calcite is the dominant polymorph regardless of the number of formula units.

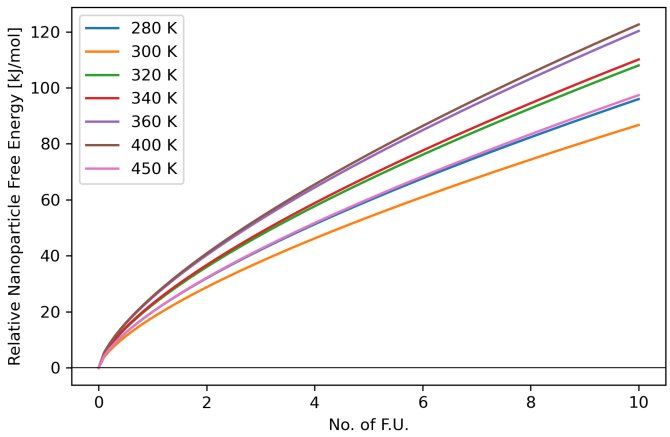

Figure 8.11: *Free energy required to convert a calcite nanoparticle to an aragonite nanoparticle at each temperature value.*

8.3 Water Ordering

Following the procedure from the previous investigation at 300 K, we want to establish how the water ordering in the system relates to the entropy and thus the temperature changes. Looking at the water density in the system, there is very little change in the distributions as the temperature varies. Figure 8.12 shows examples of the water densities calculated for the $\{10\bar{1}4\}$ surface of calcite and the $\{010\}$ surface of aragonite across a range of temperatures. There is some alteration in the distributions and the patterns present become less defined with temperature; as would be expected with greater movement of atoms. This is the case for all of the surfaces.

Although there is little visible difference with temperature, the previous method of calculating order can again be implemented to quantify the structuring in the liquid and if it changes across our systems. Since the interfacial waters are compared with a slab of bulk water further out in the system, how bulk water varies with temperature is also considered. Details of how the ordering factor varies for each surface are shown in Figure 8.13. There is a general decrease in the ordering with temperature, as one might expect. The relative ordering between surfaces is also consistent as temperature is varied.

It is important to note that although our ordering value reflects the atomic structuring of water seen in the density plots (such as Figure 8.12), we are only considering the positional density of the oxygen atoms. The positions of the hydrogen atoms were also calculated and displayed the same patterns and ordering, suggesting that there is not a significant amount of rotational ordering occurring. However this has not been explicitly calculated. Dynamical features of the water structuring are also not included in our factor. Despite its difficulty, the development of a more thorough ordering factor would be an important follow up of the work presented here

Water ordering in the system has greater correlation with the entropy fraction, not the absolute value, and thus is highly dependent on the interplay between the enthalpy and entropy contributions making up the free energy.

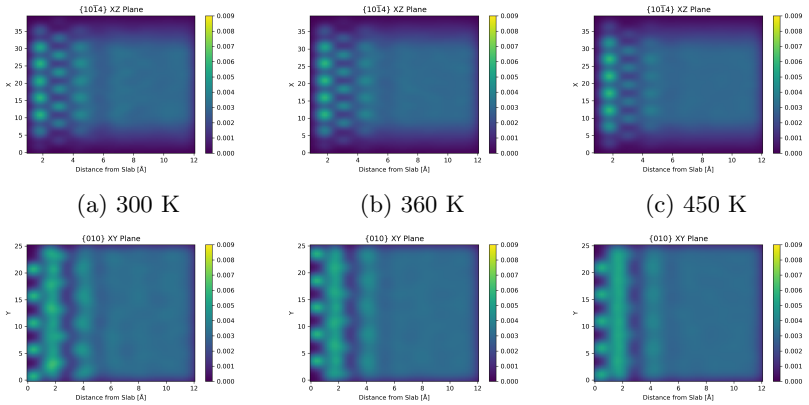

(a) 300 K (b) 360 K (c) 450 K

(d) 300 K (e) 360 K (f) 450 K

Figure 8.12: *Examples of water density plots for calcite* $\{10\bar{1}4\}$ *surface* (a) - (c) *and aragonite* $\{010\}$ *surface* (d) - (f) *at a sample of temperatures.*

The relationship between the ordering factor and the entropy contribution is displayed in Figure 8.14 for individual temperature values. The Pearson correlation coefficient is displayed on each plot and there is a clear decrease in the correlation coefficient as the temperature increases. However even at the highest temperature, the coefficient is still large enough for the ordering factor and entropy fraction to be considered correlated. The correlation here reinforces the importance of the balance between enthalpy and entropy in the systems and how that will affect the stabilities of the surfaces and ultimately the crystal polymorphs.

8.4 Conclusions

Although the free energy of the surfaces increases with temperature, the relative stability of the surfaces broadly remains the same. Calcite, specifically the $\{10\bar{1}4\}$ surface, is always the lowest in energy and thus the most stable. However the entropy contribution is of significant importance. The maximum entropy contribution for a surface is around 76%, from an aragonite surface, and the lowest contribution is around 30% which is for a calcite surface. It is clear that the entropy contribution cannot be ignored in interfacial free energy calculations and a constant correction across all surfaces is not sufficient to capture the vital role the enthalpy and entropy components contribute to the surface stabilities. For all surfaces, the maximum entropy contributions to the free energy occurs between 370 - 410 K. When considering the discrepancy between the melting and boiling points of our chosen water model and the known values for water, it is possible that this temperature range coincides with the temperature range at which aragonite formation is primarily seen.

Entropy of the system is predominantly due to water ordering at the interface whereas enthalpy comes from the water binding to the surface. Therefore we have looked at the behaviour and structuring of water in the systems. Our ordering factor quantifies the structuring seen from the water densities across

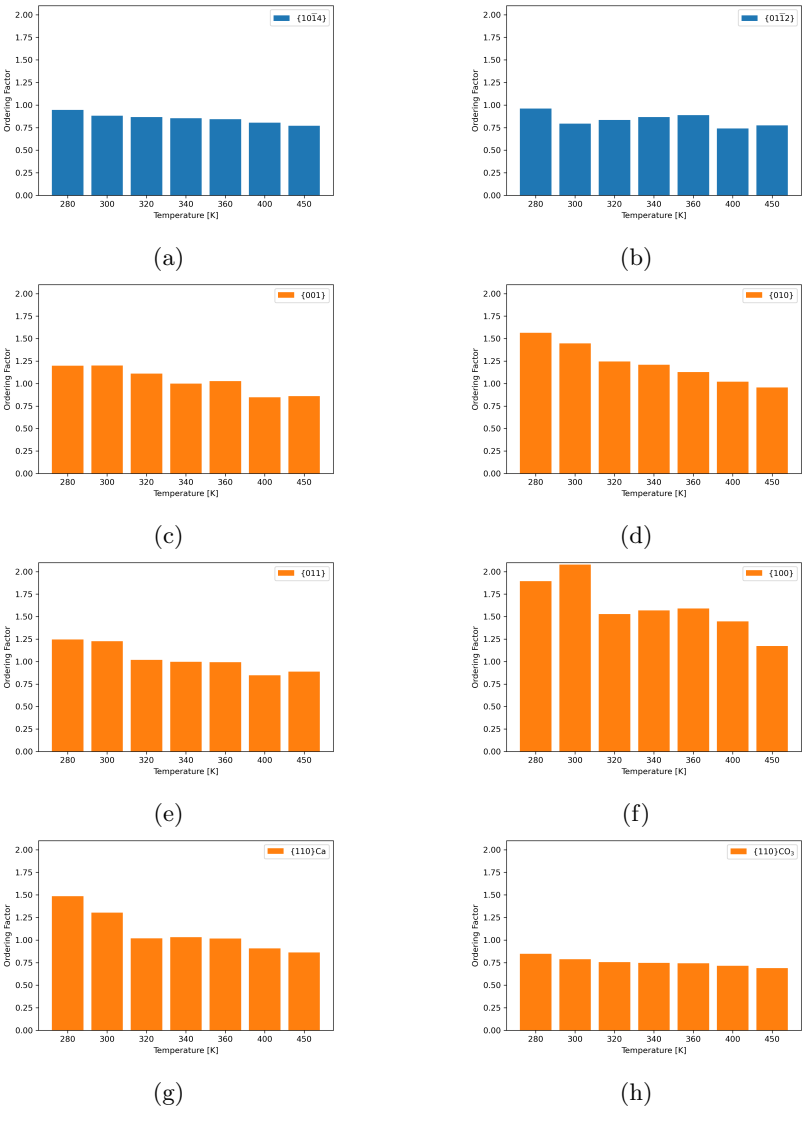

(a) (b) (c) (d) (e) (f) (g) (h)

Figure 8.13: *Variation of the ordering factor with temperature for calcite (blue) and aragonite (orange) surfaces.*

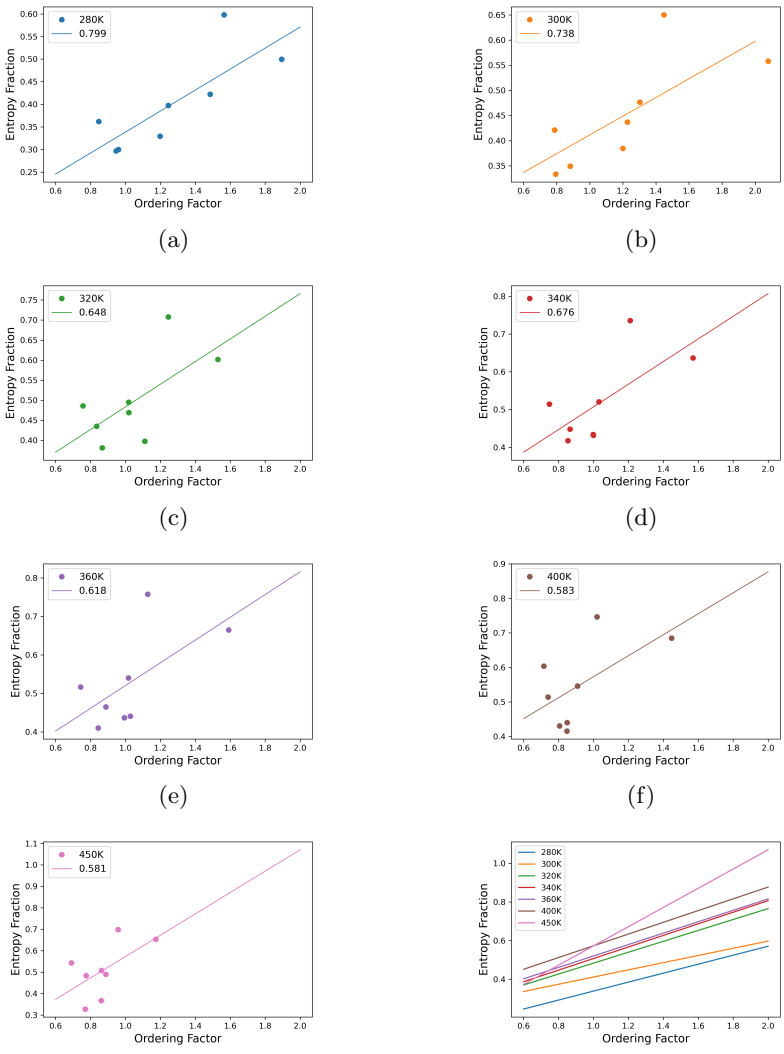

Figure 8.14: *Correlation between ordering factor and entropy fraction at all considered temperatures. The Pearson correlation coefficient for each temperature is presented in thel legend of the respective plot. Given the different scales on the plots, all trend lines are presented together in Figure* (h).

the MD simulation but does not take into account other dynamical features. In spite of its simplicity, there is a clear correlation between this ordering factor and the entropy fraction. With an increase in the entropic contribution comes a decrease in the enthalpic contribution. The lower enthalpies suggest strong binding between the water and the interface. Therefore there is particularly strong binding of the water to the aragonite surfaces in the range 340 - 400 K. Although there is change for the calcite surface, generally the binding is much weaker and enthalpy plays a more dominant role than entropy. By disrupting the water ordering at the surface/liquid interface, the entropy will decrease. Given that entropy makes up the majority of the aragonite surfaces' free energies, there is a large proportion that can be altered by disrupting the water structure in the system. If the entropy of the aragonite surfaces are reduced such that the total energy is lower than that of calcite, aragonite would become the more stable polymorph. Since the maximum entropy proportions occur at the aragonite precipitation temperature range, it is possible this is one reason for the temperature effects on calcite/aragonite stability. However, we have only considered pure water in our systems. In reality, there will be a substantial amount of ions in the system; individual $CaCO_3$ ions and NaCl ions from the initial solutions. It is possible these additional ions will have further effects on the interfacial free energies and stabilities of the surfaces not revealed here. The enthalpy and entropy contributions are not consistent across all surfaces and there is a clear distinction between the contributions to calcite and aragonite surfaces. It possibly influences polymorph selection and it is imperative that the entropy is included in interfacial free energy calculations.

Chapter 9

Conclusions and Outlook

Molecular dynamics simulations have been used to investigate polymorph selection in the calcium carbonate system with a focus on the nucleation of calcite or aragonite from amorphous calcium carbonate in solution.

In the first section of this work, we focused on identifying calcite- or aragonite-like clusters of ions within simulations of ACC. To do so, a method of cluster identification based on the Manhattan distance metric has been implemented. The technique was able to successfully identify clusters of ions within the system that resembled the geometric structure of either calcite or aragonite. As our systems of choice focused on the very early stages of nucleation, very few cluster were identified resembling either polymorph. This is unsurprising given that the systems were only run for, at most, 4 ns and the nucleation process would require significantly longer. In addition, the systems we investigated were not known to promote nucleation of either polymorph and the process was not artificially induced in any way. However, it was notable that in nearly all configurations we studied, calcite was the more dominant polymorph and was identified on average two orders of magnitude more than aragonite clusters; in line with experimental results of calcite precipitating much more readily than aragonite Additionally, we were able to quantify the resemblance of a cluster to the reference polymorphs and establish how the distribution of all ions varied within a single system and in comparison with many systems. The Manhattan distance analysis to quantify similarity to known reference structures has since been successfully applied to the similar KNO_3 system yielding large amounts of crystalline-like structures. It is a successful and simple method that can identify and quantify a cluster's similarity to known crystalline structures when applied to appropriate systems.

Experimental findings suggested that systems containing high amounts of CO_3^{2-}, and sufficient amount of Ca^{2+} will promote aragonite nucleation and sufficiently high ratios, $[1Ca^{2+}/200CO_3^{2-}]$, produce purely aragonite crystals. Our corresponding simulations contain substantially lower ratios as the simulation size required to replicate the lab conditions would be far too computationally expensive. Across the systems, very low numbers of either polymorph were found but calcite was always the dominant polymorph. There was a notable decrease in the number found when the amount of either Ca^{2+} or CO_3^{2-} was increased. We also found that the system containing the most polymorph-like

clusters was also the system with the lowest atom density and thus more readily available space for the ions to rearrange themselves. This could also explain the decrease in clusters found at higher ratios of either type if the space to rearrange themselves was not available.

It was also determined that the oxygen coordination varied from that of calcite, 6, in the higher Ca^{2+} systems and increased to that of aragonite, 9, as the Ca^{2+} content decreased and the CO_3^{2-} content increased. It is possible that in the experimental findings, aragonite was preferred due to the increased availability of O atoms. The distribution of polymorph similarities suggested that a particular cluster could resemble one polymorph or the other - it would not equally resemble both. This makes sense due to the distinct geometries of calcite and aragonite and due to the Manhattan distance analysis statistically distinguishing the two forms. The implication is that to form one polymorph, the other must be inhibited, as in seen in the case of Mg^{2+} ions inhibiting calcite to favour aragonite nucleation. It is possible that this is also the case for high carbonate ratios and that calcite is being inhibited as opposed to aragonite being promoted. However, the number of clusters found in our systems was very small, with no clusters at all being identified at high ratios and so our results are inconclusive.

The ion ratio systems were all anhydrous, but our considered experimental results look at precipitation from *solution* and therefore the influence of water on polymorph selection cannot be ignored. Our simulations found a very small increase in the number of polymorph-like clusters as the water content was increased in the thoroughly mixed systems. Again, the amount identified was very small and it is not possible to state the relationship, if any, between water content and polymorph seleciton.

On the other hand, within our simulations, there was an apparent difference in the similarity and number of polymorphs found between the mixed systems and the systems in which the molecules had separated along with the appearance of a vacuum gap. By process of elimination, it was determined that the movement of the water had altered the results and it was not due to the presence of the vacuum interface or the demixing of molecules. When investigating the water movement alone, there was some correlation between the movement of water molecules and the location of identified polymorph clusters. Both calcite and aragonite clusters were more likely to be found in regions near increased water movement. Further study of the mixing system is required to support this statement.

Although our investigations into the kinetics of calcium carbonate nucleation produced some interesting results, they yielded little insight into: why calcite is seen significantly more often than aragonite despite little difference in thermodynamic stability; how aragonite nucleation can be promoted; and why aragonite is promoted under certain conditions (ion ratio, temperature, etc.). Therefore the next body of work took a different approach and instead focused on the thermodynamics of calcium carbonate polymorph selection.

Using a novel method with Einstein crystal reference states, interfacial free energies of calcite and aragonite surfaces in water were calculated. Importantly with this method, both the enthalpic and entropic contributions to the free en-

ergy were considered, whereas previous calculations contained only the enthalpic contribution, or a uniform entropy correction was applied across all surfaces. In agreement with both experimental and previous computational findings, the $\{10\bar{1}4\}$ surface of calcite had the lowest free energy under ambient conditions and is thus the most stable. It was significantly lower than the other computed calcite surface. For aragonite, the free energies of the selected surfaces were much closer in value which again is in line with the variety of aragonite morphologies found experimentally and naturally. Both of the computed crystal morphologies were in good agreement with known equilibrium morphologies.

Upon closer inspection of the relative contributions of enthalpy and entropy to the free energy, the entropy values and proportion of the free energy varied substantially across the surfaces. The calcite surfaces were dominated by enthalpy and thus the waters were weakly bound at the interface. For the aragonite surfaces, there was a much higher entropy contribution found. This was supported by the highly structured water ordering found at the interface. Water ordering is well established at the calcite $\{10\bar{1}4\}$ surface both computationally and experimentally but there is little recorded about the ordering at the aragonite interfaces. Our simple method of quantifying order, suggest that there is in fact more water ordering occurring in the most stable aragonite surfaces than in the most stable calcite surface and is thus imposing a larger entropy penalty associated with the interface.

With increasing temperature, calcite is always the most stable polymorph. As there is no change in thermodynamic stability between calcite and aragonite, this is not unexpected - the bulk free energy curves do not cross over with increased temperature. The relative stabilities of the calcite and aragonite surfaces remain approximately the same across all temperatures, however there is variation in the relative enthalpy and entropy contributions. Between 370 K and 410 K, the entropy contributions are particularly large, reaching highs of 76% for the most stable aragonite surface. Although we have not included all dynamical features of the water, we found a strong correlation between the water ordering in the system and the entropy *fraction* of the free energy. If the structured water were to be disturbed in some way, the entropy contribution would decrease as would the free energy. Lowering the entropy contribution may be the method by which aragonite is promoted over calcite, especially as the largest entropy contribution occurs in the temperature region known to encourage aragonite nucleation.

We have investigated both the kinetic and thermodynamic factors influencing polymorph selection in calcium carbonate at the atomistic level using molecular dynamics. The Manhattan distance analysis was able to identify ion cluster resembling calcite or aragonite in ACC systems with various ion ratios and systems with various water contents. Although the technique proved successful, very limited amounts were identified in the systems. In all cases, running the simulations for longer would hopefully allow more chances for clusters to form and overall provide better statistics. For the ion ratio configurations, counterions in the system, Na^+ and Cl^- have been neglected as well as the solution itself. By including these, the simulation size would rapidly increase but would provide a more accurate representation of the experimental setup. It could also determine if the counterions are affecting polymorph selection as there quantities

would vary significantly with ion ratio.

Calculating the interfacial free energies of calcium carbonate surfaces with water has highlighted the importance of entropy in these systems. Previous calculations of free energies neglected entropy entirely or included a single value correction term for it. Going forward, it is essential for entropy to be included in free energy calculations to provide a more accurate description of the systems. For both the calcium carbonate and calcium sulphate systems, the metastable phase has the higher entropy contributions to its surfaces. Further systems should be investigated to determine if this is a common property of polymorphic systems and would provide substantial insight into the complex issue of polymorph selection.

We have also shown that entropy may be an important factor in the promotion of aragonite nucleation, particularly with temperature. There are many other aragonite and calcite surfaces that have not been considered and could serve as the basis of future work. Additionally, only pure water has been examined when $CaCO_3$ ions in solution at the interface would likely influence findings, in particular the water ordering and should also been included in further study.

Considerable work has looked at calcite-water interface however the aragonite-water interfaces are often overlooked. Moreover, despite the influence of temperature on the system being well known, there is little recent work focusing on temperature and polymorph selection. This work has shown the possible importance of entropy in the selection of aragonite over calcite but experimental work focusing on the effect of temperature and the aragonite-water interface is required for a greater understanding of polymorph selection in the calcium carbonate system.

Bibliography

[1] S. Karthika, T. K. Radhakrishnan and P. Kalaichelvi. A review of classical and nonclassical nucleation theories. *Crystal Growth & Design*, 16:6663–6681, 2016.

[2] L. Addadi, S. Raz and S. Weiner. Taking advantage of diorder: Amorphous calcium carbonate and its roles in biomineralization. *Advanced Materials*, 15:959–970, 2003.

[3] W. Sun, S. Jayaraman, W. Chen, K. A. Persson and G. Ceder. Nucleation of metastable aragonite in caco$_3$ in seawater. *PNAS*, 112:3199–3204, 2015.

[4] S. Yeandel, C. L. Freeman and J. H. Harding. A general method for calculating solid/liquid interfacial free energies from atomistic simulations: Application to $CaSO_4.H_2O$. *Journal of Chemical Physics*, 157:084117, 2022.

[5] C. Breitkreuz. Spherulites and lithophysae - 200 years of investigation on high-temperature crystallization domains in silica-rich volcanic rocks. *Bulletin of Volcanology*, 75:705, 2013.

[6] S. Mann. *Biomineralization*. Oxford University Press, 2001.

[7] B. J. Murray, D. O'Sullivan, J. D. Atkinson and M. E. Webb. Ice nucleation by particles immersed in supercooled cloud droplets. *Chemical Society Reviews*, 41:6519–6554, 2012.

[8] T. Tyrrell. Calcium carbonate cycling in future oceans and its influence on future climates. *Journal of Plankton Research*, 30:141–156, 2008.

[9] J. C. Orr et. al. Anthropogenic ocean acidification over the twenty-first century and its impact on calcifying organisms. *Nature*, 437:681–686, 2005.

[10] K. S. Lackner. A guide to CO_2 sequestion. *Science*, 300:1677–1678, 2003.

[11] W. Beckmann, editor. *Crystallization: Basic Concepts and Industrial Applications*. John Wiley & Sons, Incorporated, 2013.

[12] M. Senra , E. Panacharoensawad, K. Kraiwattanawong , P Singh and H. S. Fogler. Role of n-alkane polydispersity on the crystallization of n-alkanes from solution. *Energy Fuels*, 22:545–555, 2008.

[13] J. W. Mullin. *Crystallization (4th Edition)*. Elsevier Science & Technology, 2001.

[14] A. Llinás and J. M. Goodman. Polymorph control: past present and future. *Drug Discovery Today*, 13:198–210, 2009.

[15] P. G. Vekilov. The two-step mechanism of nucleation of crystals in solution. *Nanoscale*, 2:2346–2357, 2010.

[16] D. Kashchiev. *Nucleation*. Elsevier Science & Technology, 2000.

[17] K. F. Kelton and A. L Greer. *Nucleation in Condensed Matter: Application in Materials and Biology*. Elsevier Science & Technology, 2010.

[18] K. Sangwal. *Nucleation and Crystal Growth: Metastability of Solutions and Melts*. John Wiley & Sons, Incorporated, 2018.

[19] I. V. Markov. *Crystal Growth For Beginners: Fundamentals of Nucleation, Crystal Growth and Epitaxy (2nd Edition)*. World Scientific Publishing Company, 2003.

[20] J. J. De Yoreo. A holistic view of nucleation and self-assembly. *MRS Bulletin*, 42:525–531, 2017.

[21] H. Cölfen. Nonclassical nucleation and crystallization. *Crystals*, 10:61, 2020.

[22] D. Gebauer, M. Kellermeier, J. D. Gale, L. Bergstrom and H. Colfen. Pre-nucleation clusters as solute precursors in crystallisation. *Chemical Society Reviews*, 43:2348–2371, 2014.

[23] G. C. Sosso, J. Chen, S. J. Cox, M. Fitzner, P. Pedevilla, A. Zen, and A. Michaelides. Crystal nucleation in liquids: Open questions and future challenges in molecular dynamics simulations. *Chemical Reviews*, 116:7078–7116, 2016.

[24] D. Gebauer and H. Cölfen. Prenucleation clusters and non-classical nucleation. *Nanotoday*, 6:564–584, 2011.

[25] G. I. Tóth , T. Pusztai, G. Tóth and L. Gránásy. Amorhpous nulceation precursor in highly nonequilibrium fluids. *Physical Review Letters*, 107:175702, 2011.

[26] W. J. E. M. Habraken et. al. Ion-association complexes unite classical and non-classical theories for the biomimetic nucleation of calcium phosphate. *Nature Communications*, 4:1507, 2013.

[27] F. Zhang. Nonclassical nulceation pathways in protein crystallization. *Journal of Physics: Condensed Matter*, 29:443002, 2017.

[28] O. Galkin, K. Chen , R. L. Nagel and P. G. Vekilov. Liquid-lquid separation in solutions of normal and sickle cell hemoglobin. *PNAS*, 99:8479–8483, 2002.

[29] C. Rodriguez-Navarro, A. B urgos Cara , K. Elert, C. V. Putnis and E. Ruiz-Agudo. Direct nanoscale imaging reveals the growth of calcite crystals via amorphous nanoparticles. *Crystal Growht & Design*, 16:1850–1860, 2016.

[30] J. J. De Yoreo et. al. Crystallization by particle attachment in synthetic, biogenic and geological environmenta. *Science*, 349:498–510, 2015.

[31] G. A. Tribello , F. Bruneval , C. Liew and M. Parrinello. A molecular dynamics study of the early stages of calcium carbonate growth. *Journal of Physical Chemistry B*, 113:11680–11687, 2009.

[32] D. Gebauer , P. Raiteri, J. D. Gale, and H.Cölfen. On classical and non-classical views on nucleation. *American Journal of Science*, 318:969–988, 2018.

[33] B. Wang , Y. Xiao and Z. Xu. Variation in propeties of pre-nucleation calcium carbonate clusters induced by aggregation: a molecular dynamics study. *Crystals*, 11:102, 2021.

[34] A. J. Giuffre , A. C. Gagnon , J. J. De Yoreo and P. M. Dove. Isotopic tracer evidence for the amorphous calcium carbonate to calcite transformation by dissolutin-reprecipitation. *Geochimica et Cosmochimica Acta*, 165:407–417, 2015.

[35] B. Jin, Z. Liu and R. Tang. Recent experimental exxplorations of non-classical nucleation. *Crystal Engineering Communications*, 22:4057–4073, 2020.

[36] F. Zhang, J. A. Gavira, G. W. Lee and D. Zhan. Nonclassical nucleation - role of metastable intermediate phase in crystal nucleation: An editorial prefix. *Crystals*, 11:174, 2021.

[37] M. H. Nielsen, S. Aloni and J. J. De Yoreo. In situ TEM imaging of $caco_3$ nucleation reveals coexistence of direct and indirect pathways. *Science*, 345:1158–1162, 2014.

[38] J. R. Espinosa, E. Sanz, C. Valeriani and C. Vega. Homogeneous ice nucleation evaluated for several water models. *Journal of Chemical Physics*, 141:18C529, 2014.

[39] D. Quigley and P. M. Rodger. Metadynamics simulations of ice nucleation and growth. *The Jounral of Chemical Physics*, 128:154518, 2008.

[40] H. Niu, Y. I. Yang and M. Parrinello. Temperature dependence of homogeneous nucleation in ice. *Physical Review Letters*, 122:245501, 2019.

[41] N. E. R. Zimmermann, B. Vorselaars, D. Quigley and B. Peters. Nucleation of NaCl from aqueous solution: Critical sizes, ion-attachment kinetics and rates. *Journal of the American Chemical Society*, 137:13352–13361, 2015.

[42] H. Jiang, A. Haji-Akbari, P. G. Debenedetti and A. Z. Panagiotopoulos. Forward flux sampling calculation of homogeneous nulceation rates from NaCl solutions. *The Jounral of Chemical Physics*, 148:044505, 2018.

[43] A. R. Finney and M. Salvalaglio. Multiple pathways in nacl homogeneous crystal nucleation. *Faraday Discussions*, 235:56, 2022.

[44] F. C. Meldrum and H. Cölfen. Controlling mineral morphologies and structures in biological and synthetic systems. *Chemical Reviews*, 108:4332–4432, 2008.

[45] F. C. Meldrum. Calcium carbonate in biomineralisation and biomimetic chemistry. *International Materials Reviews*, 48:187–224, 2003.

[46] J. Rohleder and E. Kroker. *Calcium carbonate: From the cretaceous period into the* 21^{st} *century.* Springer Science & Business Media, 2001.

[47] H. Saulat et. al. Preparation and applications of calcium carbonate whisker with a special focus on construction materials. *Construction and Building Materials*, 236:117613, 2020.

[48] R. M. Santos , P. Ceulemans and T. Van Gerven. Synthesis of pure aragonite by sonochemical mineral carbonation. *Chemical Engineering Research and Design*, 90:715–725, 2012.

[49] S. Maleki , M. Boarzegar-Jalali , M. H. Zarrintan , K. Adibkia and F. Lotfipour. Calcium carbonate nanoparticles; potential applications in bone and tooth disorders. *Pharmaceutical Sciences*, 20:175–182, 2015.

[50] J. T. Avaro, C. Ruiz-Agudo, E. Landwehr, K. Hauser and D. Gebauer. Impurity-free amorphous calcium carbonate, a preferential material for pharmaceutical and medical applications. *Europen Journal of Mineralogy*, 31:231–236, 2019.

[51] K. Hua, H. Wang, R. Chung and J. Hsu. Calcium carbonate nanoparticles improve crop nutrition and increase insect resistance. *Journal of Pesticide Science*, 40:208–213, 2015.

[52] K. W. T. Goulding. Soil acidification and the importance of liming agricultural soils with particular reference to the united kingdom. *Soil Use and Managment*, 32:390–399, 2016.

[53] O. Nahi, A. N. Kulak, S. Zhang, X. He, Z. Aslam, M. A. Ilett, I. J. Ford , R. Darkins and F. C. Meldrum. Polyamines promote aragonite nucleation and generate biomimetic structures. *Advanced Science*, 10:2203759, 2023.

[54] A. M. Belcher , X. H. Wu, R. J. Christensen, P. K. Hansama , G. D. Stucky and D. E. Morse. Control of crystal phase switching and orientation by soluble mollusc-shell proteins. *Nature*, 381:56–58, 1996.

[55] G. Falini, S. Albeck , S. Weiner and L. Addadi. Control of aragonite or calcite polymorphihsm by mollusk shell macromolecules. *Science*, 271:67–69, 1996.

[56] J. C. Jamieson. Phase equilbrium in the system calcite-aragonite. *Journal of Chemical Physics*, 21:1385–1390, 1953.

[57] G. Falini, S. Fernani, M. Reggi, B. N. Džakula and D. Kralj. Evidence of structural variablility among synthetic and biogenic vatertite. *ChemComm*, 50:15370, 2014.

[58] F. Liendo , M. Arduino, F. A. Deorsola and S. Bensaid. Factors controlling and influencing polymorphism, morphology and size of calcium carbonate synthesized through the carbonation route: A review. *Powder Technology*, 398:117050, 2022.

[59]

[60] S. Kim, J. Jeon and M. Kim. Vaterite production and particle size and shape control using seawater as an indirect carbonation solvent. *Journal of Environmental Chemical Engineering*, 10:107296, 2022.

[61] M. Seifan and A. Berenjian. Application of microbially induced calcium carbonate precipitation in designing bio self-healing concrete. *World Journal of Microbiology and Biotechnology*, 34:168, 2018.

[62] D. B. Trushina, T. V. Bukreeva , M. V. Kovalchuk and M. N. Antipina. $Caco_3$ vaterite microparticles for biomedical and personal care applications. *Materials Science and Engineering C*, 45:644–658, 2014.

[63] M. S. Clark et. al. Deciphering mollusc shell production: the roles of genetic mechanisms through to ecology, aquaculture and biomimetics. *Biological Reviews*, 95:1812–1837, 2020.

[64] J. Seto et. al. Structure-property relationships of a biological mesocrystal in the adult sea urchin spine. *PNAS*, 109:3699–3704, 2012.

[65] I. Brown. What factors determine cation coordination numbers. *Acta Crystallagraphica Section B*, 44:545–553, 1988.

[66] U. Balthasar and M. Cusack. Aragonite-calcite seas - quantifying the gray areas. *Geology*, 43:99–102, 2015.

[67] J. W. Morse , R. S. Arvidson and A. Lüttge. Calcium carbonate formation and dissolution. *Chemical Reviews*, 107:342–381, 2007.

[68] A. A. Finch and N. Allison. Coordination of Sr and Mg in calcite and aragonite. *Mineralogical Magazine*, 71:539–552, 2007.

[69] D. Aquilano, M. Bruno and L. Pastero. Impurity effects on habit change and polymorphic transitions in the system: Aragonite–calcite–vaterite. *Crystal Growth & Design*, 20:2497–2507, 2020.

[70] W. Park et. al. Effects of magnesium chloride and organic additives on the synthesis of aragonite precipitated calcium carbonate. *Journal of Crystal Growth*, 310:2593–2601, 2008.

[71] Y. Kitano, K. Park and D. W. Hood. Pure aragonite synthesis. *Journal of Geophysical Research*, 67:4525–4957, 1962.

[72] J. W. Morse, Q. Wang and M. Y. Tsio. Incluences of temperature and Mg:Ca ratio on $caco_3$ precipitates from seawater. *Geology*, 25:85–87, 1997.

[73] G. Wolf and C. Günther. Thermophysical investigations of the polymorphous phases of calcium carbonate. *Journal of Thermal Analysis and Calorimetry*, 65:687–698, 2001.

[74] K.K. Sand, D.J. Tobler, S. Dobberschütz, K.K. Larsen, E. Makovicky, M.P. Andersson, M. Wolthers and S.L.S. Stipp. Calcite growth kinetics: Dependence on saturation index, Ca^{2+}:CO_3^{2-} activity ratio, and surface atomic structure. *Crystal Growth & Design*, 16:3602–3612, 2016.

[75] S. Y. M. H. Seepma, S. E. Ruiz-Hernandez, G. Nehrke, K. Soetaert, A. P. Philipse, B. W. M. Kuipers and M. Wolthers. Controlling $CaCO_3$ particle size with { Ca^{2+} } : { CO_3^{2-} } ratios in aqueous environments. *Crystal Growth & Design*, 21:1576–1592, 2021.

[76] C. R. Blue, A. Giuffre, S. Mergelsberg, N. Han , J. J. De Yoreo and P.M Dove. Chemical and physical controls on the transformation of amorphous calcium carbonate into crystalline $CaCO_3$ polymorphs. *Geochimica et Cosmochimica Acta*, 196:179–196, 2017.

[77] A. Sugawara, T. Nishimura, Y. Yamamoto, H. Inoue, H. Nagasawa and T. Kato. Self-organization of oriented calcium carbonate/polymer composites: Effects of a matrixpeptide isolated from the exoskeleton of a crayfish. *Angewandte Chemie*, 118:2881–3049, 2006.

[78] J. Aizenberg, S. Weiner and L. Addadi. Coexistence of amorphous and crystalline calcium carbonate in skeletal tissues. *Connective Tissue Research*, 44:20–25, 2003.

[79] A. V. Radha, T. Z. Forbes , C. E. Killian, P. U. P. A. Gilbert and A. Navrotsky. Transformation and crystallization energetics of synthetic and biogenic amorphous calcium carbonate. *PNAS*, 107:16438–16443, 2010.

[80] S. Weiner, Y. Levi-Kalisman, S. Raz and L. Addadi. Biologically formed amorphous calcium carbonate. *Connective Tissue Research*, 44:214–218, 2001.

[81] Y. Levi-Kalisman, S. Raz, S. Weiner, L. Addadi and I. Sagi. Structural differences between biogenic amorphous calcium carbonate phases using x-ray absorption spectroscopy. *Advanced Functional Materials*, 12:43–48, 2002.

[82] H. Du and E. Amstad. Water: How does it influence the $CaCO_3$ formation. *Angewandtle Chemie International Edition*, 59:1798–1816, 2020.

[83] H. Tomono et. al. Effects of magnesium ions and water molecules on the structure of amorphous calcium carbonate: a molecular dynamics study. *Journal of Physical Chemistry B*, 117:14849–14856, 2013.

[84] R. Demichelis, P. Raiter, J. D. Gale, D. Quigley and D. Gebauer. Stable prenucleation mineral clusters are liquid-like ionic polymers. *Nature Communications*, 2:590, 2011.

[85] P. Raiteri and J. D. Gale. Water is the key to nonclassical nucleation of amorphous calcium carbonate. *Journal of the American Chemical Society*, 132:17623–17634, 2010.

[86] C. Günther, A. Becker , G. Wolf and M. Epple. In vitro synthesis and structural characterization of amorphous calcium carbonate. *Zeitschrift für anorganische und allgemeine Chemie*, 631:2533–2946, 2005.

[87] B. Cantaert et. al. Use of amorphous calcium carbonate for the design of new materials. *ChemPlusChem*, 82:107–120, 2017.

[88] J. Gómez-Morales, J. Torrent-Burgués and R. Rodríguez-Clemente. Nucleation of calcium carbonate at different initial ph conditions. *Journal of Crystal Growth*, 169:331–338, 1996.

[89] M. Zheng et. al. Confinement generates single-crystal aragonite rods at room temperature. *PNAS*, 115:7670–7675, 2011.

[90] M.P. Allen and D. J. Tildesley. *Computer Simulation of Liquids*. Oxford University Press, 1991.

[91] A. Malthe-Sorenssen. *Elementary Thermal Physics Using Python*. Springer, 2016.

[92] S. Toxvaerd and J.C. Dyre. Communication: Shifted forces in molecular dynamics. *Journal of Chemical Physics*, 134:081102, 2011.

[93] A. P. Thompson, H. M. Aktulga , R. Berger , D. S. Bolintineanu , W. M. Brown , P. S. Crozier , P. J. in 't Veld , A. Kohlmeyer , S. G. Moore , T. D. Nguyen , R. Shan , M. J. Stevens , J. Tranchida , C. Trott and S. J. Plimpton. LAMMPS - a flexible simulation tool for particle-based materials modeling at the atomic, meso, and continuum scales. *Computer Physics Communications*, 271:108171, 2022.

[94] P. Young. Leapfrog method and other "symplectic" algorithms for integrating Newton's laws of motion. pages 1–5, 2013.

[95] I. T. Todorov, W. Smith, K. Trachenko and M. T. Dove. *Journal of Materials Chemistry*, 16:1911–1918, 2006.

[96] A. R. Leach. *Molecular Modelling: Principles and Applications*. Pearson Education, 2001.

[97] M. Tuckerman. *Statistical Mechanics: Theory and Molecular Simulation*. Oxford University Press, 2010.

[98] H. J. C. Berendsen, J. P. M. Postma, W. F. van Gunsteren, A. Di Nola and J. R. Haak. Molecular dynamics with coupling to an external bath. *Journal of Chemical Physics*, 81:3684–3690, 1984.

[99] W. G. Hoover. Canonical dynamics: Equilibrium phase-space distributions. *Physical Review A*, 31:1695–1697, 1985.

[100] S. Melchionna , G. Ciccotti and B. L. Holian. Hoover NPT dynamics for systems varying in shape and size. *Molecular Physics*, 78:533–544, 1993.

[101] A. Hinchcliffe. *Molecular modelling for beginners*. Wiley-Blackwell, 2008.

[102] A. Martini. Short course on molecular dynamics simulation: Boundary conditions. pages 1–12, 2009.

[103] D. C. Rapaport. *The Art of Molecular Dynamics Simulation*. Cambridge University Press, 2004.

[104] N. Attig. *Computational Soft Matter: from Synthetic Polymers to Proteins: Lecture notes*. NIC, 2004.

[105] B. A. Luty and W. F. van Gunsteren. Calculating electrostatic interactions using the particle-particle particle-mesh method with nonperiodic long-range interactions. *Journal of Physical Chemistry*, 100:2581–2587, 1996.

[106] D. Frenkel and B. Smit. *Understanding Molecular Simulation: From Algorithms to Applications*. Elsevier: Science & Technology, 2001.

[107] G. Falini, S. Albeck, S. Weiner and L. Addadi. Control of aragonite or calcite polymorphism by mollusk shell macromolecules. *Science*, 271:67–69, 1996.

[108] J. C. Jamieson. Phase equilibrium in the system calcite-aragonite. *The Journal of Chemical Physics*, 21:1385–1390, 1953.

[109] S. Y. M. H. Seepma, S. E. Ruiz-Hernadez, G. Nehrke, K. Soetaert, A. P. Philipse, B. W. M. Kuipers and M. Wolthers. Controlling $CaCO_3$ particle size with Ca^{2+}:CO_3^{2-} ratios in aqueous environments. *Crystal Growth & Design*, 21:1576–1590, 2021.

[110] C. R. Blue, A. Giuffre, S. Mergelsberg, N. Han, J. J. De Yoreo and P. M. Dove. Chemical and physical controls on the transformation of amorphous calcium carbonate into crystalline $CaCO_3$ polymorphs. *Geochimica et Cosmochimica Acta*, 196:179–196, 2017.

[111] G. A. Tribello, F. Bruneval, C. Liew and M. Parrinello. A molecular dynamics study of the early stages of calcium carbonate growth. *The Journal of Physical Chemistry B*, 113:11680–11687, 2009.

[112] H. Tomono, H. Nada, F. Zhu, T. Sakamoto, T. Nishimura and T. Kaato. Effects of magensium ions and water molecules on the structure of amorphous calcium carbonate: A moelcular dynamics study. *The Journal of Physical Chemistry B*, 117:14849–14856, 2013.

[113] R. S. DeFever, C. Targonski, S. W. Hall , M. C. Smith and S. Sarupria. A generalized deep learning approach for local structure identification in molecular simulations. *Chemical Science*, 10:7503–7515, 2019.

[114] H. Nada. A new methodology for evaluating the structural similarity between different phases using a dimensionality reduction technique. *ACS Omega*, 3:5789–5798, 2018.

[115] P. J. Steinhardt , D. R. Nelson and M. Ronchetti. Bond-orientational order in liquids and glasses. *Physical Review B*, 28:784, 1983.

[116] D. Quigley, C. L. Freeman, J. H. Harding and P. M. Roger. Sampling the structure of calcium carbonate nanoparticles with metadynamics. *Journal of Chemical Physics*, 134:044703, 2011.

[117] K. Fuchs. A quantum mechanical investigation of the cohesive forces of metallic copper. *Proc. R. Soc. Lond. A*, 151:585–602, 1935.

[118] P. Raiteri, R. Demichelis and J. D. Gale. Thermodynamically consistent force field for molecular dyanmics simulations of alkaline-earth carbonates and their aqueous speciation. *The Journal of Physical Chemistry C*, 119:24447–24458, 2015.

[119] A. Kaufman Katz, J. P. Glusker, S. A. Beebe and C. W. Bock. Calcium ion coordination: A comparison with that of beryllium, magnesium and zinc. *Journal of the American Chemical Society*, 118:5752–5763, 1996.

[120] Y. Wu, H. L. Tepper and G. A. Voth. Flexible simple point-charge water model with improved liquid-state properties. *Journal of Chemical Physics*, 124:024503, 2006.

[121] J. Ihli et. al. Dehydration and crystallization of amorphous calcium carbonate in solution and in air. *Nature Communications*, 5:3169, 2014.

[122] P. Fenter, S. Kerisit , P. Raiteri and J. D. Gale. Is the calcite-water interface understood? direct comparisons of molecular dynamics simulations with specular x-ray reflectivity data. *Journal of Physical Chemistry C*, 117:5028–5042, 2013.

[123] H. Jing and A. J. Patel. Recent advances in estimating contact angles using molecular simulations and enhanced sampling methods. *Current Opinion in Chemical Engineering*, 23:130–137, 2019.

[124] A. Malani, A. Raghavanpillai, E. B. Wysong and G. C. Rutledge. Can dynamic contact angle be measured using molecular modelling? *Physical Review Letters*, 109:184501(5), 2012.

[125] S. Angioletti-Uberti , M. Ceriotti, P. D. Lee and M. W. Finnis. Solid-liquid interface free energy through metadynamics simulations. *Physical Review B*, 81:125416(11), 2010.

[126] J. R. Espinosa, C. Vega and E. Sanz. The mold integration method for the calculation of the crystal-fluid interfacial free energy from simulations. *Journal of Physical Chemistry*, 141:134709, 2014.

[127] J. R. Espinosa, C. Vega, C. Valeriani and E. Sanz. The crystal-fluid interfacial free energy and nucleation rate of NaCl from different simulation methods. *Journal of Chemical Physics*, 142:194709, 2015.

[128] J. Q. Broughton and G. H. Gilmer. Molecular dynamics investigation of the crystal-fluid interface. VI. excess surface free energies of crystal-liquid systems. *Journal of Chemical Physics*, 84:5759–5768, 1986.

[129] R. L. Davidchack. Hard spheres revisited: Accurate calculation of the solid-liquid interfacial free energy. *Journal of Chemical Physics*, 133:234701, 2010.

[130] R. Benjamin and J. Horbach. Crystal-liquid interfacial free energy of hard spheres via a thermodynamic integration scheme. *Physical Review E*, 91:032410, 2015.

[131] N. H. de Leeuw and S. C. Parker. Surface structure and morphology of calcium carbonate polymorphs calcite, aragonite and vaterite: an atomistic approach. *Journal of Chemical Physics B*, 102:2914–2922, 1998.

[132] M. A. Bano, M. P. Roger and D. Quigley. New insight into the stability of $CaCO_3$ surfaces and nanoparticles via molecular simulation. *Langmuir*, 30:7513–7521, 2014.

[133] J. G. Kirkwood and F. P. Buff. The statistical mechanical theory of surface tension. *Journal of Physical Chemistry*, 17:338–343, 1949.

[134] E. S. Dana. *A textbook of mineralogy.* John Wiley & Sons, 1885.

[135] W. A. Deer, R. A. Howie and J. Zussman. *Rock-forming minerals. Vol. 5, Non-silicates.* Longman, 1962.

[136] S. B. Mukkamala, C. E. Anson and A. K. Powell. Modelling calcium carbonate biomineralization processes. *Journal of Inorganic Biochemistry*, 100:1128–1138, 2006.

[137] F. Legoll, M. Luskin and R. Moeckel. Non-ergodicity of the Nosé-Hoover thermostatted harmonic oscillator. *Archive for Rational Mechanics and Analysis*, 184:449–463, 2007.

[138] M. Bruno , F. R. Massaro, L. Pasterp , E. Costa , M. Rubbo, M. Prencipe and D. Aquilano. New estimates of the free energy of calcite/water interfaces for evaluating the equilibrium shape and nucleation mechanisms. *Crystal Growth & Design*, 13:1170–1179, 2013.

[139] W. Sekkai and A. Zaoui. Nanoscale analysis of the morphology and surface stability of calcium carbonate polymorphs. *Scientific Reports*, 3:1587, 2013.

[140] F. R. Massaro , M. Bruno and M. Rubbo. Surface structure, morphology and (110) twin of aragonite. *CrystEngComm*, 16:627–635, 2014.

[141] B. R. Heywood and S. Mann. Molecular construction of oriented inorganic materials: Controlled nucleation of calcite and aragonite under compressed langmuir monolayers. *Chemistry of Materials*, 6:311–318, 1994.

[142] Z. Hu, M. Shao, H. Li, Q. Cai, C. Zhong, Z. Xianming and Y. Deng. Synthesis of needle-like aragonite crystals in the presence of magnesium chloride and their application in papermaking. *Advanced Composite Materials*, 18:315–326, 2009.

[143] G. Wolf, J. Lerchner, H. Schmidt, H. Gamsjäger , E. Königsberger and P. Schmidt. Thermodynamics of $CaCO_3$ phase transitions. *Journal of Thermal Analysis*, 46:353–359, 1996.

[144] P. Raiteri, J. D. Gale, D. Quigley and P. M. Rodger. Derivation of an accurate force-field for simulating the growth of calcium carbonate from aqueous solution: A new model for the calcite-water interface. *Journal of Physical Chemistry C*, 114:5997–6010, 2010.

[145] F. Heberling, T. P. Trainor, J. Lützenkirchen, P. Eng, M. A. Denecke and D. Bosbach. Structure and reactivity of the calcite-water interface. *Journal of Colloid and Interface Science*, 354:843–857, 2011.

[146] S. Varghese, S. K. Kannam, J. S. Hansen and S. P. Sathian. Effect of hydrogen bonds on the dielectric properties of interfacial water. *Langmuir*, 35:8159–8166, 2019.

[147] C. Vega, E. Sanz and J. L. F. Abascal. The melting temperature of the most common models of water. *Journal of Chemical Physics*, 122:114507, 2005.

[148] M. Fugel and V. C. Weiss. A corresponding-states analysis of the liquid-vapor equilibrium properties of common water models. *Journal of Chemical Physics*, 145:064505, 2017.

[149] M. A. Floriano and C. A. Angell. Surface tension and molar surface free energy and entropy of water to -27.2 deg c. *Journal of Chemical Physics*, 94:4199–4202, 1990.

[150] S. P. K. Pathirannahalage, N. Meftahi, A. Elbourne, A. C. G. Weiss, C. F. McConville, A. Padua, D. A. Winkler, M. C. Gomes, T. L. Greaves, T. C. Le, Q. A. Besford and A. J. Christofferson. Systematic comparison of the structural and dynamic properties of commonly used water models for molecular dynamics simulations. *Journal of Chemical Information and Modeling*, 61:4521–4536, 2021.

[151] Dortmund Data Bank. DDB surface tension of water. `http://www.ddbst.com/en/EED/PCP/SFT_C174.php`. [Online; accessed 20-April-2023].